NOVEL MOSFET-BASED FLUIDIC SENSORS AND SIMULATIONS OF THERMAL BUBBLE NUCLEATION IN NANOCHANNELS

By

Manoj Sridhar

Dissertation

Submitted to the Faculty of the

Graduate School of Vanderbilt University

in partial fulfillment of the requirements

for the degree of

DOCTOR OF PHILOSOPHY

in

Physics

August, 2008
Nashville, Tennessee

Approved:

Anthony B. Hmelo

Leonard C. Feldman

Deyu Li

Dongqing Li

Franz J. Baudenbacher

ACKNOWLEDGMENTS

Over the past 5 years, I have had the good fortune of meeting and working with numerous people who have helped in many different ways to reach my goal of attaining a Ph.D. degree. Firstly, I'd like to acknowledge my Ph.D. committee members - Dr. Len Feldman, Dr. Tony Hmelo, Dr. Deyu Li, Dr. Dongqing Li and Dr. Franz Baudenbacher - for guiding my research work with invaluable feedback. I've had the unique opportunity to count on three of them, Dr. Feldman, Dr. Hmelo and Dr. Deyu Li, as my primary advisers and I thank them for their patience, sincerity and motivation. I would also like to acknowledge financial support courtesy of National Institute of Health (NIH) Grant #5R01HG002647.

In addition, numerous people have helped me significantly during my Ph.D. career. First, I would like to thank the Vanderbilt Institute for Nanoscale Science and Engineering (VINSE) and Vanderbilt Institute for Integrative Biosystem Research and Education (VIIBRE) for providing my access to micro/nanofabrication tools, without which this thesis could not be completed. I am also indebted to Dr. Shane Hutson and Dr. Xiaoyan Ma for their graciousness and assistance in allowing me to use their inverted fluorescence microscope which proved crucial for the nanofluidics work.

I would also like to specially thank Dr. Dongyan Xu with whom I had the pleasure of collaborating extensively in both experimental and computational work. The following post-docs and students that I have collaborated with who have contributed in

various ways to my Ph.D. thesis - Dr. Bo Choi, Yuejun Kang, Jiashu Sun, Saumitra Vajandar, Ronald Reiserer. You have all been instrumental in teaching me various aspects of microfabrication and I have had valuable discussions with all of you.

I would also like to acknowledge the effort and support of all the professors at Vanderbilt University who have helped me out with the classes I needed to take to complete the course requirements for this degree. Also, I would like to thank my lab and office colleagues, Eugene Donev, Drs. John Rozen, Sriram Dixit and Sarit Dhar for helping me with daily issues in the lab, and for general discussions which have invariably been fruitful.

Away from the work setting, I would also like to acknowledge my terrific group of friends who have been a tremendous support group for me outside the university. Thanks to all the Galaxy and Soccettes soccer team players for the regular recreational outlet of playing soccer and the balance you provided to my life in general. You have been my family for the last 5 years and I could not have done this without all of you! A special thanks to Hugo Valle who commiserated with me for the last 5 years as a friend, colleague and roommate.

Lastly and most importantly, I want to thank my family for their unfailing support and encouragement in me over the better part of this decade as I embarked on my overseas educational adventure. I am forever indebted to them and I dedicate this Ph.D. thesis to them.

TABLE OF CONTENTS

PART ONE: EXPERIMENTAL WORK

PART TWO: COMPUTATIONAL WORK

APPENDICES

LIST OF TABLES

LIST OF FIGURES

ORGANIZATION OF THIS THESIS

This thesis is divided into two parts. *Part One* deals with the experimental development of novel micro/nanofluidic sensors. Chapter I gives an introduction to micro/nanofluidic sensors by providing relevant background about the fundamentals of electrokinetics, the historical development of resistive pulse sensors and the fundamentals of MOSFET operation. Chapter II discusses the experimental development and characterization of a novel MOSFET-based microfluidic resistive pulse sensor, and Chapter III presents experimental efforts to extend the sensing capability of this new MOSFET-based sensing scheme to the nanoscale.

Part Two deals with molecular dynamics simulations of thermal bubble formation in nanochannels. The motivation for performing these simulations is discussed first in Chapter IV, followed by an overview of the molecular dynamics technique. Next, a review of the literature published in this field is presented. We then discuss our simulation models, and our verification of the code and then, report and discuss our simulation results.

CHAPTER I

INTRODUCTION TO MICRO/NANOFLUIDIC SENSORS

The era of micro/nanofabrication has created a technical revolution in electronics and led to entirely new technologies based on sophisticated materials processing. One area that has seen an explosion of interest is the control of fluid flow on the nanoscale. Applications are abundant, ranging from fluidic transistors analogous to their electronic counterparts to drug delivery and extraordinary molecular sensors. In this Chapter, we first present the motivation behind the development of micro/nanofluidic sensors. Then, we introduce the basic concepts of electrokinetics, which is the most common mechanism used to drive fluid through micro/nanofluidic devices. A historical overview of the resistive-pulse sensing technique, most commonly used in micro/nanofluidic sensors is then presented. Finally, we briefly discuss our novel sensing scheme which integrates a metal-oxide-semiconductor field-effect transistor (MOSFET) with the traditional resistive-pulse sensing scheme.

1.1 Motivation

What is micro/nanofluidics, and why should we be interested? These are the fundamental questions addressed in this section. Micro/nanofluidics can be defined as the study of fluid flow within micro/nanoscale structures. Interest in this field has grown tremendously since the 1990s due to the rapid growth in technology that enables researchers to fabricate and study devices with micro/nanoscale structures.

In particular, the development of advanced lithographic techniques such as electron beam lithography have enabled the fabrication of solid-state structures down to just a few nanometers in dimension. This ability to fabricate structures anywhere from several hundreds of microns (conventional photolithography) down to a few nanometers (electron beam lithography) allows us to precisely manipulate and interrogate individual biomolecules and nanoparticles. The grand vision for micro/nanofluidics is to develop fully-integrated micro/nanoscale devices with the ability to conduct traditional, laboratory-style experiments, such as separations and chemical reactions, on individual molecules on microchips. Such devices are called Lab-on-a-Chip (LOC) devices or Micro-Total Analysis Systems (μ-TAS). The main advantages of such fully-integrated devices include:

- Portability of devices
- High throughput analysis
- Low volume of reagents required
- Automation

Prototype μ-TAS devices have already been demonstrated in the laboratory, and a comprehensive review can be found elsewhere (van den Berg & Lammerink, 1998; Reyes et al., 2002; Auroux et al., 2002; Knight, 2002; Erickson & Li, 2004). In recent years, much attention has been devoted to the development of nanofluidic devices with very specific capabilities that may eventually be integrated into a LOC device. For instance, nanofluidic transistors and diodes which have the ability to control the flow of fluid analogous to the way its electronic counterparts controls the flow of electrons and holes have been developed recently (Daiguji et al., 2004; Karnik et al., 2005; Karnik et al., 2006; Vlassiouk & Siwy, 2007). Also, nanofluidic sensors which are able to sense and discriminate individual biomolecules such as DNA and other proteins have also been reported (Kasianowicz et al., 1996; Bayley & Martin, 2000; Bayley & Cremer, 2001; Meller & Branton, 2002; Peterman et al., 2002; Saleh & Sohn, 2003; Nakane et al., 2003; Li et al., 2003; Chang et al., 2004; Chen et al., 2004a; Heng et al., 2004; Henriquez et al., 2004; Fan et al., 2005; Fologea et al., 2005; Storm et al., 2005; Smeets et al., 2006a). Given that the field of micro/nanofluidics is still in its infancy, we can expect rapid advances in technology and applications in the near future.

In this thesis, we will focus on micro/nanofluidic sensors. The common theme among all the micro/nanofluidic sensing works in general is the use of an applied electric field to drive fluid flow through the micro/nanofluidic channel network. The fluid flow resulting from the application of an applied electric field is known as electrokinetics. An overview of the fundamentals of electrokinetics is presented in the following section.

1.2 Fundamentals of Electrokinetics

As mentioned in the previous section, most modern micro/nanofluidic sensors use an external electric field to drive the electrolyte and analytes through the micro/nanofluidic circuits. In our experimental work reported in Chapters II and III, we also utilize electrokinetics as the primary means of transport in our micro/nanofluidic devices, and so a brief overview of electrokinetic phenomena is presented to provide a basis for the fluid transport mechanism in our devices.

Any fundamental discussion of electrokinetics must begin with a discussion of the electric double layer (Li, 2004; Masliyah & Bhattacharjee, 2006). Solid surfaces often acquire a surface charge when they are brought in contact with a liquid medium. There are several mechanisms by which these surfaces acquire charge such as, for example, ionization of surface groups and specific ion adsorption. The details of these mechanisms are not central to our discussion and are discussed elsewhere (Hunter, 1981; Lyklema, 1995; Masliyah & Bhattacharjee, 2006). As a result of this acquired surface charge, when electrolytes are present in the liquid medium, the ion distribution close to the solid surface is affected. Ions with the opposite charge as that of the surface, known as counterions, are attracted to the surface, while ions with the same charge as that of the surface, known as coions, are repelled from the surface. Such a redistribution of the ions in the electrolyte solution results in the formation of an electric double layer (EDL) as shown in Fig. 1.1. The layer of counterions right next to the solid surface is known as the Stern layer, which is typically 1 - 2 atomic radii thick. These ions are essentially immobile due to their strong electrostatic attraction with the surface charge at the solid surface. We will neglect the Stern layer in our discussion of electrokinetic phenomena for the sake of simplicity because it plays a minor role in electrokinetic phenomena compared to the diffuse layer. The net charge density decreases gradually to zero from the edge of the Stern layer to the bulk of the electrolyte where the liquid is electrically neutral. This region is known as the diffuse layer. The thickness of this layer is often characterized by a parameter known as the

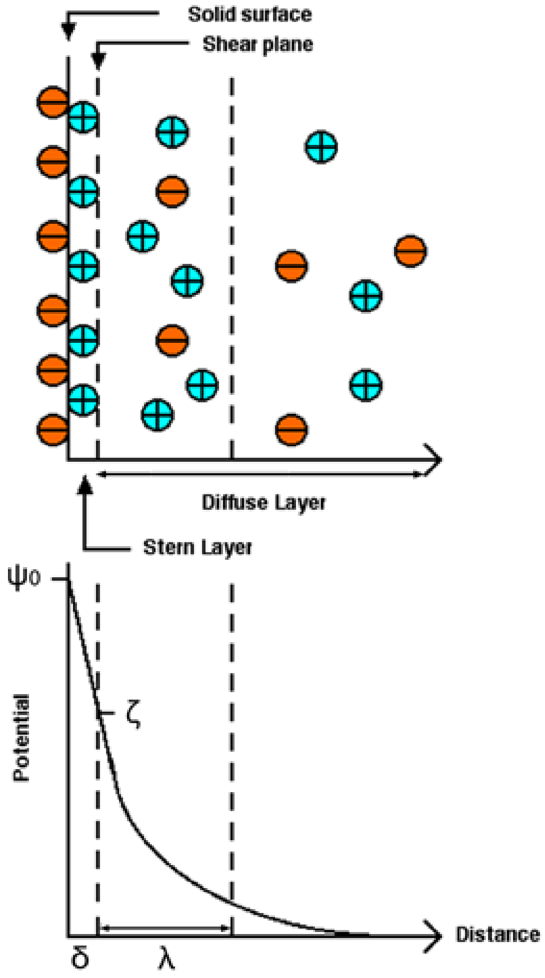

Figure 1.1: Schematic of an electric double layer (EDL) formed adjacent to a negatively charged solid surface like glass. δ is the Stern layer thickness, λ is the characteristic EDL thickness, ψ_0 is the electric potential at the solid surface, and ζ is the potential at the shear plane and is also known as the zeta potential.

EDL thickness, λ, which is a function of the electrolyte concentration in the liquid and the electrical properties of the liquid. In reality, the diffuse layer may be as much as 3 - 5 times thicker than the EDL thickness. The potential close to the interface of the Stern layer and the diffuse layer is known as the zeta potential, ζ. Theoretically, it is defined as the potential at the shear plane, where the no-slip fluid flow boundary condition is assumed to apply (i.e. where fluid velocity, $u = 0$). However, in practice, the zeta potential, ζ, is often used as an approximation to the surface potential, ψ_0, because it is the quantity that can be measured experimentally.

We will now use the Gouy-Chapman model (Li, 2004; Masliyah & Bhattacharjee, 2006) of the electric double layer to derive an expression for the characteristic EDL thickness, λ. It must be noted that the Gouy-Chapman model makes two key assumptions: (a) ions in the electrolyte are treated as point charges, and (b) the existence of the Stern layer is neglected. As such, the validity of this theory is questionable when the characteristic EDL thickness is comparable to the nanochannel size. However, in our experiments, we are far from this regime and so this simple model is valid. Consider a symmetrical electrolyte, such as KCl, where both the cation and anion have equal valence, z_i, in a nanochannel. We can write the spatial distribution of the anions and cations using the Boltzmann distribution as

$$n_+(z) = n_-(z) = n_0 \exp\left(\frac{-z_i q \psi(z)}{kT}\right) \tag{1.1}$$

where $n_+(z)$ and $n_-(z)$ are the number density of cations and anions at a distance, z, away from the solid surface respectively, n_0 is the number density of ions in the bulk of the electrolyte (i.e. far away from the solid surface), $\psi(z)$ refers to the potential at a distance, z, away from the solid surface, q is the electronic charge, k is Boltzmann's constant and T refers to the temperature of the system. Thus, we can write the total charge density of the electrolyte, ρ, as

$$\rho(z) = z_i q(n_+ - n_-) = -2 z_i q n_0 \sinh\left(\frac{z_i q \psi(z)}{kT}\right) \tag{1.2}$$

From Poisson's equation, we have $\nabla^2 \psi = -\rho q/\epsilon$ where ϵ is the dielectric constant of the fluid. So in 1-dimension, we can write

$$\frac{d^2\psi}{dz^2} = \frac{2 z_i q n_0}{\epsilon} \sinh\left(\frac{z_i q \psi(z)}{kT}\right) \tag{1.3}$$

Eq. 1.3 can be linearized if we assume that $z_i q\psi/kT << 1$ such that $\sinh(z_i q\psi/kT) \sim z_i q\psi/kT$ (Debye-Hückel approximation). Thus, Eq. 1.3 becomes

$$\frac{d^2\psi}{dz^2} = \frac{1}{\lambda^2} \cdot \psi(z) \tag{1.4}$$

where we can define the characteristic EDL thickness, λ as

$$\lambda = \left(\frac{\epsilon kT}{2 z_i^2 q^2 n_0}\right)^{1/2} \tag{1.5}$$

As can be seen from Eq. 1.5, the characteristic EDL thickness is purely a function of the concentration of the electrolyte solution and is independent of the properties of the solid surface. The variation of the EDL thickness as a function of electrolyte

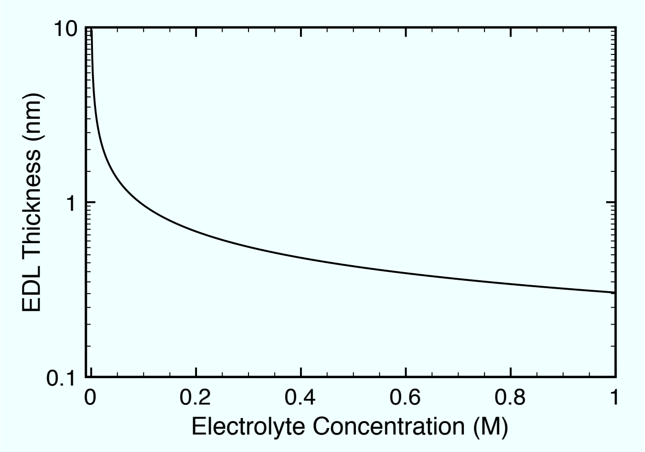

Figure 1.2: Plot of EDL thickness, λ, as a function of bulk electrolyte concentration for a symmetric electrolyte such as KCl ($z_i = 1$).

concentration for a symmetric monovalent electrolyte such as KCl is shown in Fig. 1.2. Typically the EDL thickness is $\sim$ 10 nm when $n_0 = 1$ mM and $\sim$ 1 nm when $n_0 = 100$ mM.

In general, there are four common types of electrokinetic phenomena: electro-osmosis, electrophoresis, streaming potential and sedimentation potential (Li, 2004; Masliyah & Bhattacharjee, 2006). Only electro-osmosis and electrophoresis will be discussed since they are the most relevant phenomena for this thesis. Electro-osmosis is defined as the movement of fluid, due to an applied electric field with respect to a stationary charged surface while electrophoresis is defined as the movement of a charged particle relative to a stationary liquid when an external electric field is applied. Consider a simple nanochannel system where an external electric field is applied as shown in Fig. 1.3. The mobile counterions in the EDL move in the direction of the electric field. As they move from the anode to the cathode, they

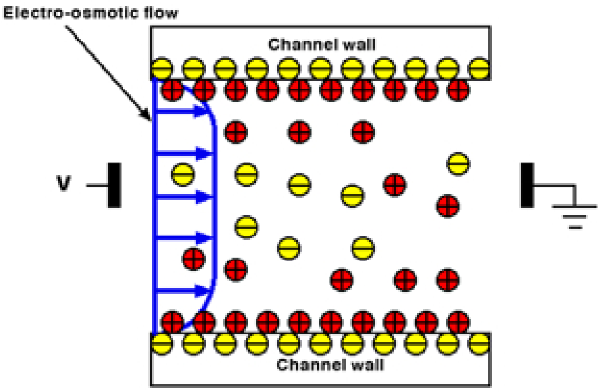

Figure 1.3: Schematic of electro-osmotic flow (EOF) in a nanochannel with negatively charged channel walls. The arrows indicate the direction of EOF.

drag the rest of the fluid along with them, and this flow is called electro-osmotic flow (EOF). Electrophoretic flow (EPF) refers to the flow of particles in an applied electric field due to their inherent surface charge. The direction of EPF will depend on the sign of the net charge on the particle. The derivation of the fluid flow equations for electro-osmotic flow and electrophoretic flow are presented in Appendix A, and only the final results are presented here. When the EDL thickness is much smaller than the dimensions of the channel through which the fluid is flowing, the average EOF velocity under an tangential applied electric field, E, is independent of the channel dimensions and is given by

$$u_{EOF} = -\frac{\epsilon \zeta_w E}{\eta} \tag{1.6}$$

where ζ_w represents the zeta potential of the channel walls and η represents the viscosity of the fluid. The overall sign of u_{EOF} indicates the direction of EOF with respect to the applied electric field. The EOF will be in the same direction as the applied electric field when the zeta potential of the channel walls is negative (as shown in Fig. 1.3, and conversely, the EOF will be in the opposite direction to the applied electric field when the zeta potential of the channel walls is positive.

The electrophoretic flow (EPF) velocity, u_{EPF}, is given by

$$u_{EPF} = \frac{\epsilon \zeta_p E}{\eta} \tag{1.7}$$

where ζ_p is the zeta potential of the charged particle, which is basically determined by the amount of surface charge on the particle and the size of the particle. Consider a negatively charged biomolecule such as DNA flowing through a channel in an external electric field as shown in Fig. 1.4. The EOF velocity will drive the biomolecule from

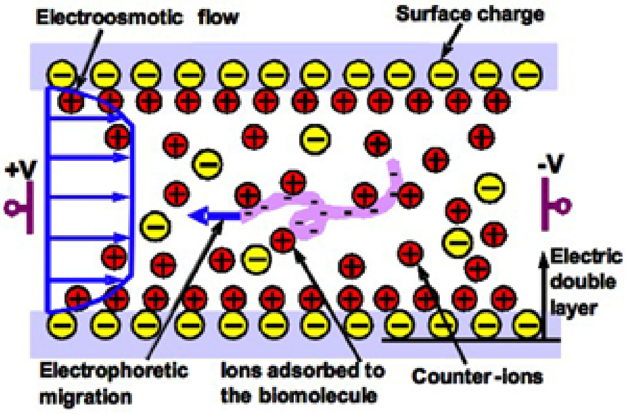

Figure 1.4: Schematic of EOF and EPF for a nanochannel system with negatively charged channel walls. A negatively charged biomolecule is present in the nanochannel, and the EPF and EOF are in opposite directions as indicated. (Figure courtesy of D. Xu).

the anode to the cathode due to the flow of the mobile counterions, whereas the EPF velocity, due to the inherent negative surface charge of the biomolecule, will drive the particle in the opposite direction from the cathode to the anode. Thus, under certain conditions, when $\zeta_w = \zeta_p$, it is possible that $u_{EOF} = u_{EPF}$. In such cases, the biomolecule will move with negligible speed through the channel, assuming there are no other forces present in the system. Such a scenario is detrimental for nanofluidic sensor applications since we want the biomolecules to flow through the fluidic channels with significant speed so that they can be detected. This issue will be discussed further in Chapter III where we report our experimental work on nanofluidic sensors.

1.3 Introduction to Resistive-Pulse Sensing

1.3.1 Basic Principle of Resistive-Pulse Sensing

As mentioned in Sect. 1.1, one of the important trends of micro/nanofluidics research is the development biomolecular and nanoparticle sensors. One commonly used technique for sensing biomolecules such as DNA is known as resistive-pulse sensing. This technique was invented and patented by W. H. Coulter (1953) and consequently, a sensing device based on this technique is often referred to as a Coulter counter. The sensing scheme, which is illustrated in Fig. 1.5, is based on the principle that the electrical resistance of a small, electrolyte-filled channel increases as particles flow through the channel.

When a non-conducting particle flows through a small channel, it displaces a

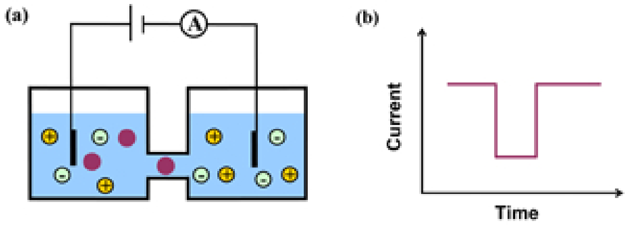

Figure 1.5: (a) Schematic of a Coulter counter-type device, where particles are sensed as they flow through a narrow sensing channel under an applied electric field. (b) Schematic of the ionic current measured as a particle passes through the narrow sensing channel (Xu, 2008).

volume of electrolyte equivalent to its own volume, and hence increases the ohmic resistance of the channel. This resistance modulation will lead to a corresponding decrease of ionic current or an increase of the voltage drop across the sensing channel, which can be measured experimentally and used to detect particles in the channel. The magnitude of the current drop measured depends on the fraction of the volume of the sensing channel that is occluded by the particle being sensed.

DeBlois and Bean (1970) derived an expression for the change in the resistance of a cylindrical sensing channel when a spherical, insulating particle is present in the sensing channel as shown in Fig. 1.6. By solving Laplace's equation with spherical boundary conditions, they showed that the increase in resistance of the sensing channel, ΔR, due to the presence of the spherical particle can be written as

$$\Delta R \approx \frac{4\rho_{fluid} d^3}{\pi D^4} \tag{1.8}$$

where ρ_{fluid} represents the resistivity of the conducting electrolyte. Eq. 1.8 is valid

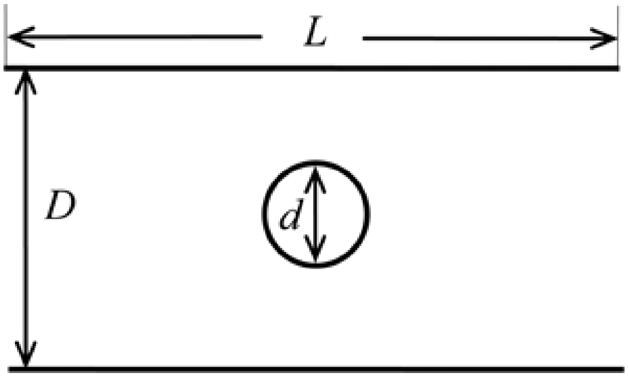

Figure 1.6: Schematic of a cylindrical sensing channel of diameter D and length L that is filled with electrolyte and contains a non-conducting sphere of diameter d (Xu, 2008).

when the ratio $d/D << 1$ and $D/L < 1$. For a cylindrical sensing channel as shown in Fig. 1.6, the resistance of the sensing channel itself (without the spherical particle) is $R = 4\rho_{fluid}L/\pi D^2$. So, the relative resistance modulation is given by

$$\frac{\Delta R}{R} = \frac{d^3}{D^2 L} = \frac{3}{2} \cdot \frac{V_p}{V_c} \tag{1.9}$$

where V_p and V_c are the volumes of the spherical particle and sensing channel respectively. We can see that the relative resistance modulation is roughly equal to the volume ratio of the particle to the sensing channel. When a constant voltage is applied across the sensing channel, from Ohm's law, the relative ionic current modulation can be written as

$$\frac{\Delta I}{I} = \frac{\frac{V}{R} - \frac{V}{R+\Delta R}}{\frac{V}{R}} = \frac{\Delta R}{R} \cdot \left(1 + \frac{\Delta R}{R}\right)^{-1} \tag{1.10}$$

When $\Delta R/R << 1$ (i.e. particle is much smaller than channel), Eq. 1.10 may be simplified to

$$\frac{\Delta I}{I} \approx \frac{\Delta R}{R} \tag{1.11}$$

So, the relative ionic current modulation, $\Delta I/I$, will also be roughly equal to the volume ratio of the particle with respect to the channel, V_p/V_c, when the particle diameter is much smaller than the channel diameter. When the particle size becomes comparable to that of the channel, higher order correction terms will become important and the relationship between the volume ratio of the particle to the channel and the relative resistance modulation will take on a more complex form. However, since we are concerned with trying to sense the smallest possible particles through a channel of a particular size, we will only focus on the scenario presented where the particle diameter is much smaller than the channel diameter.

1.3.2 Development of Resistive-Pulse Sensing

Coulter (1956) first demonstrated that a device based on resistive-pulse sensing could be used to count micron-scale particles like red blood cells at a high count rate of $\sim$ 6000 particles/s. DeBlois and Bean (1970) showed that they were able to detect a minimum volume ratio of 0.06% using a tapered pore with end diameters of 490 nm and 450 nm as polystyrene beads of 91 nm in diameter flowed through the pore. DeBlois and Wesley (1977) then showed that the resistive-pulse sensing could be used to detect the size and concentration of viruses using sub-micron pores. As further optimization of the Coulter counter device continued, Sikdar and Webster (1980) showed that they were able to count particles at a high rate and measure the mean and variation of particle size distribution accurately. Berge and co-workers (Berge et al., 1989) developed a technique to reverse the flow of particles through the sensing channel to study the dissolution of air bubbles and radial migration of particles as a function of time.

The development of Coulter counters since the 1990s has focused on using nanoscale pores for single molecule/nanoparticle sensing and making on-chip Coulter counters (Henriquez et al., 2004). Bezrukov and colleagues (Bezrukov et al., 1994) demonstrated the counting of polymer molecules as they passed through a single alamethicin pore $\sim$ 5 nm long and $\sim$ 2 nm in diameter. Kasianowicz and co-workers (Kasianowicz et al., 1996) showed that they were able to sense individual strands of DNA and RNA as they translocated through a protein nanopore, α-hemolysin. These promising results sparked many studies of DNA translocation and dynamics in biological nanopores (Bayley & Martin, 2000; Bayley & Cremer, 2001; Meller & Branton, 2002; Peterman et al., 2002; Nakane et al., 2003). However, the biological nanopores are not very robust or size-tunable. Therefore, efforts have been made to fabricate artificial, solid-state nanopores to overcome the above-mentioned limitations.

Kobayashi and Martin (1997) fabricated gold nanotubules of diameter < 2 nm and used them to measure the concentration of divalent cations, $\mathrm{Ru(bpy)}_3^{2+}$ and methylviologen(MV^{2+}). Sun and Crooks (2000) used a multi-wall carbon nanotube (150 nm in diameter)-based device to sense 60-100 nm in diameter polystyrene particles. This method was then improved by members of the same group to detect size and surface charge of polystyrene particles simultaneously (Ito et al., 2003; 2004). In 2005, Fan and co-workers (Fan et al., 2005) reported an on-chip device based on silicon dioxide nanotubes and the detection of DNA translocation through the nanotube.

Li and co-workers (Li et al., 2001; 2003) were the first to fabricate solid-state nanopores using ion and electron beam technologies and used these devices to study DNA translocation and dynamics. Similar devices based on SiN_x or SiO_2 nanopores were then developed by them and other groups (Chang et al., 2004; Chen et al., 2004a; 2004b; Heng et al., 2004; Fologea et al. 2005; Storm et al., 2005; Smeets et al., 2006a) to detect DNA translocation. Chang and colleagues (Chang et al., 2004) studied DNA translocation through SiO_2 nanopores 50-60 nm long, 4-5 nm in diameter and demonstrated that the ionic current in the nanopore could increase due to the mobile counter ions adsorbed on the DNA itself. Chen and co-workers (Chen et al., 2004a; 2004b) fabricated $\sim$ 15 nm in diameter SiN_x nanopores, and showed that coating the nanopore surface with alumina could reduce the electrical noise. Heng and colleagues (Heng et al., 2004) made $\sim$ 1 nm in diameter SiN_x nanopores and reported that they were able to distinguish single-stranded DNA from double-stranded DNA and resolve the length of the molecule. Fologea and co-workers (Fologea et al., 2005) reported the possibility of slowing down DNA translocation by a factor of ten by fine-tuning the experimental conditions. Storm and colleagues (Storm et al., 2005) observed the translocation time and the length of the DNA segments and found a power-law relation between them. Smeets et al. (2006a) studied DNA translocation through $\sim$ 10 nm in diameter SiO_2 nanopores for various concentrations of electrolyte. Both this group and Fan et al. (2005) found that the ionic current could either decrease or increase, depending on the concentration of the electrolyte used. The decrease in ionic current is expected from the Coulter principle. The increase in ionic current observed at low salt concentrations was attributed to the contribution to channel conductance from the mobile counter ions adsorbed on the DNA molecule.

Another salient trend of the Coulter counter development since the 1990s is the development of on-chip devices. Larsen and colleagues (Larsen et al., 1997), and Koch and co-workers (Koch et al., 1999) were the first to report the design and fabrication of microchannel-based Coulter counters using silicon micromachining techniques. Saleh and Sohn (2001) fabricated a microchip Coulter counter on a quartz substrate and showed that they were able to sense individual nanoparticles of 87 nm in diameter with a sensing channel of 8.3 μm long and a cross-sectional area of 0.16 μm^2. Later, they developed a poly-dimethyl-siloxane (PDMS)-based device with a sensing channel of 200 nm in diameter and 3 μm long and showed that they were able to detect 16 μm long λ-DNA segments (Saleh & Sohn, 2003). Carbonaro and Sohn (2005) then fabricated a PDMS-based device to detect the size change of 490 nm-diameter latex colloids upon antigen-antibody binding on the antibody-coated colloid surface. More recently, novel designs (Zhang et al., 2005; Jagtiani et al., 2006a; 2006b; Rodriguez-Trujillo et al., 2007; Zhe et al., 2007) of on-chip Coulter counters were also developed by other researchers to realize high throughput counting and sizing, hydrodynamic focusing, etc.

1.3.3 MOSFET-based Resistive-Pulse Sensing

Despite all the success in the fabrication of nanoscale features leading to a dramatic reduction in the volume of the sensing channel, the lowest detectable volume ratio using the resistive-pulse sensing technique, has been 0.06%, as reported by DeBlois and Bean (1970), which is approximately the same as the relative modulation of the ionic current. Improving this lowest detectable volume ratio will enable us to sense smaller particles with larger sensing channels, thereby reducing the pressure on the fabrication process to create structures of dimensions comparable to those of the analyte particle. The fundamental limitation that has prevented the improvement of this minimum detectable volume ratio is noise in the current/voltage measurements. Noise in solid-state nanopore-based resistive-pulse sensors has only been studied and characterized recently (Siwy & Fulinski, 2002; Tabard-Cossa et al., 2007; Smeets et al., 2008; Uram et al., 2008). The main sources of noise have been identified to be the thermal and shot noise generated by the current preamplifier, and the nanopore device itself, dielectric noise due to the substrate material, and flicker noise, the origins of which are still not well understood. Consequently, we can expect researchers to improve experimental methods to reduce the noise observed in traditional resistive-pulse sensors, and thereby improve the minimum detectable volume ratio in the near future.

However, we have chosen to improve device sensitivity by amplifying the signal observed when a particle translocates through the sensing channel. We have recently reported a design of fluidic sensors based on the resistive-pulse sensing principle, which integrates the fluidic circuit with a metal-oxide-semiconductor field effect transistor (MOSFET) and detects the MOSFET drain current to sense the resistance modulation of the fluidic sensing channel as particles flow through it (Xu et al., 2007; M. Sridhar et al., 2008b). Due to the non-linear dependence of the MOSFET drain current on the MOSFET gate voltage, we are able to achieve amplification of the resistance modulation of the fluidic-sensing channel. As such, a good understanding of the performance of a MOSFET as a function of the MOSFET gate voltage is necessary to understand the amplification obtained by our sensing scheme.

1.4 MOSFET Fundamentals

MOSFETs have been studied extensively for several years and a comprehensive review of MOSFET fundamentals maybe found elsewhere (Sze, 1981; Casey, 1999; Kang & Leblebici, 1999). In this section, we present a basic overview of the structure of a n-channel MOSFET and the variation of the MOSFET drain current as a function of the MOSFET gate voltage.

Fig. 1.7 shows a schematic of a typical n-channel MOSFET. The substrate is p-type and the source and drain regions are n^+-doped. When there is no bias applied to the gate, the source-drain electrodes correspond to two back-to-back p-n junctions, and there is only a very small, reverse leakage current which we will ignore for simplicity. When a small positive gate voltage is applied, there is weak inversion at the semiconductor surface as holes are repelled away from the surface into the substrate and electrons are attracted to the surface due to the positive gate voltage applied. As a result, in the presence of a positive drain-source bias, a small current will flow from source to drain. Such a current is known as sub-threshold current, $I_{D,sub}$, which can be written as follows

$$I_{D,sub} = k_{sub} \left(\frac{q\psi_S}{kT}\right)^{1/2} \left[1 - \exp\left(\frac{qV_{DS}}{kT}\right)\right] \exp\left(\frac{q\psi_S}{kT}\right) \tag{1.12}$$

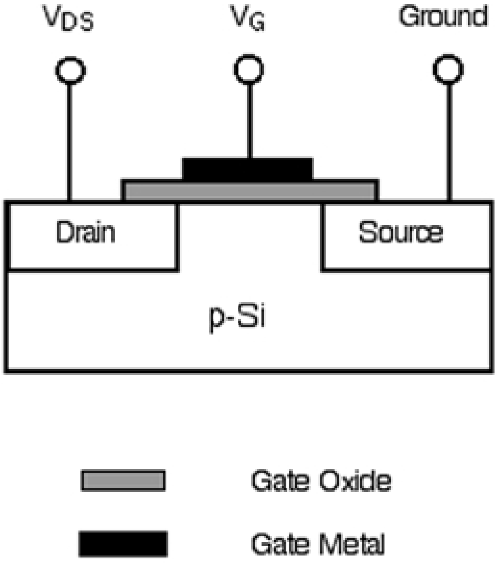

Figure 1.7: Schematic of a typical n-channel MOSFET. The substrate is p-type and the source and drain regions are n^+-doped.

where k_{sub} is a constant and k and T are Boltzmann's constant and temperature, respectively. ψ_S is the surface potential of the MOSFET electronic channel and is given by

$$\psi_S = V_G - V_{FB} - \frac{a^2 kT}{2q}\left\{\left[1 + \frac{4}{a^2}\left(\frac{qV_G}{kT} - \frac{qV_{FB}}{kT} - 1\right)\right]^{1/2} - 1\right\} \tag{1.13}$$

where $a = 2(\epsilon_s/\epsilon_{ox})(d_{ox}/L_D)$. ϵ_s and ϵ_{ox} are the permittivity of the semiconductor and the oxide, respectively. d_{ox} is the thickness of the MOSFET gate oxide, L_D is the extrinsic Debye length, and V_{FB} is the flat-band voltage. The drain current in the sub-threshold region varies exponentially with gate voltage, V_G as can be inferred from Eqs. 1.12 and 1.13.

When a sufficiently large positive voltage is applied to the gate, the density of mobile electrons at the surface becomes equal to the density of holes in the bulk of the p-type substrate. A surface inversion layer or channel is said to have formed between the source and the drain. The minimum gate voltage required for channel formation is known as the threshold voltage, V_T, and is given by

$$V_T = V_{FB} + 2\psi_B + \frac{\sqrt{2\epsilon_s q N_A(2\psi_B + V_{SB})}}{C_i} \tag{1.14}$$

where ψ_B is the potential difference between the Fermi level and the intrinsic Fermi level, N_A is the substrate doping, V_{SB} is the substrate bias, and C_i is the capacitance per unit area of the oxide layer. In practice, the threshold voltage of a MOSFET is determined experimentally from x-intercept of the $I_D^{1/2} - V_G$ curve of the MOSFET, as shown schematically in Fig. 1.8.

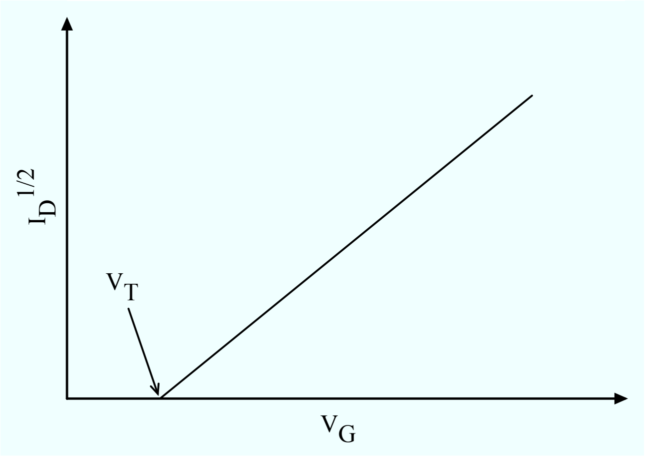

Figure 1.8: Schematic of a typical $I_D^{1/2} - V_G$ curve for a MOSFET. The threshold voltage, V_T is determined by the x-intercept of the curve as shown.

For $V_G > V_T$, when a small drain-source bias, V_{DS} is applied, current flows through the channel from source to drain and the MOSFET is said to be in the ON state. The channel acts simply as a resistor and the drain current is proportional to V_{DS}. This regime of operation is known as the linear region and the drain current in this region is given by

$$I_{D,lin} = k_{lin}(V_G - V_T)V_{DS} \tag{1.15}$$

As the drain-source bias is increased further, the channel depth at the drain end of the channel decreases to zero and eventually the channel is said to have "pinched off". The pinch-off occurs at the drain end of the channel when $V_{DS} = V_G - V_T$. Substituting this relation into Eq. 1.15 gives

$$I_{D,sat} = k_{sat}(V_G - V_T)^2 \tag{1.16}$$

Increasing the drain-source bias further (holding the gate voltage constant) does not affect the drain current anymore, and hence this region of operation is known as the saturation region. In the saturation region, the MOSFET drain current is solely dependent on the gate voltage applied. The variation of the MOSFET drain current as a function of V_{DS} when $V_G > V_T$, is shown in Fig. 1.9. The linear and saturation regions are marked, and the different behavior of the MOSFET in these two regions can be clearly observed.

As can be seen from Eqs. 1.12, 1.15 and 1.16, the drain current of the MOSFET varies differently with gate voltage, V_G, depending on the region in which the

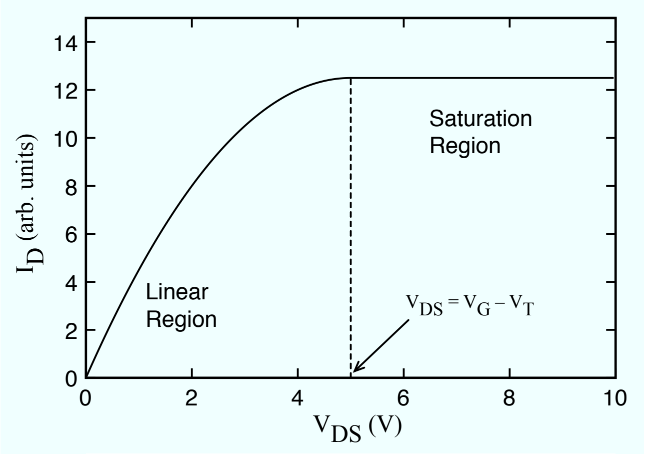

Figure 1.9: Schematic of a typical $I_D - V_{DS}$ curve for a MOSFET. The dotted line indicates where the channel is pinched off i.e. $V_{DS} = V_G - V_T = 5$ V.

MOSFET is operating. We can use a parameter called the transconductance of a MOSFET, which is essentially the rate of change of MOSFET drain current with respect to gate voltage, to characterize the sensitivity of the drain current on gate voltage in the three different regions of operation. The transconductance, g, is usually defined as

$$g = \left.\frac{\partial I_D}{\partial V_G}\right|_{V_{DS}=const} \tag{1.17}$$

Using Eqs. 1.12, 1.15 and 1.16, we can derive expressions for the transconductance of a MOSFET in the three different regions of operation. For clarity, the dependence of the MOSFET transconductance on the gate voltage, which is important for determining the sensitivity of the MOSFET drain current to the gate voltage, is tabulated in Table 1.1.

From Table 1.1, we observe that the transconductance varies exponentially with gate voltage in the sub-threshold region, while it is linearly dependent on gate voltage

Table 1.1: MOSFET transconductance, g, in the sub-threshold, linear and saturation regions.

Operation Region	Expression for transconductance
Sub-threshold	$g_{sub} \propto \exp(qV_G/kT)$
Linear	$g_{lin} = k_{lin}V_{DS}$
Saturation	$g_{sat} = 2k_{sat}(V_G - V_T)$

in the saturation region, and independent of gate voltage in the linear region. Thus, the MOSFET drain current is most sensitive to the gate voltage, V_G, in the sub-threshold region followed by the saturation region, and least sensitive in the linear region. We will take advantage of the high sensitivity of the MOSFET drain current to the gate voltage in the saturation and sub-threshold regions in our novel sensing scheme. The details of this sensing scheme are discussed in Chapter II.

1.5 Summary

In conclusion, we have given a brief overview of micro/nanofluidics and motivated the interest in developing micro/nanofluidic sensors, especially for biomolecular sensing applications. Since the invention of resistive-pulse sensing in 1953, there have been numerous devices built using this sensing scheme to detect nanoparticles. The smallest volume ratio detected was reported by DeBlois and Bean in 1970 (0.06%). Since that time, there has been no significant improvement in this critical parameter.

We present a sensing scheme which integrates the fluidic circuit with a MOSFET, in order to enhance the sensitivity of traditional resistive-pulse sensors. This novel sensing scheme enables us to detect smaller particles flowing through a larger sensing channel, thereby reducing the pressure on the fabrication process to create structures of comparable dimensions as the particles being sensed. In the next chapter, we present this microfluidic MOSFET-based resistive-pulse sensor that was able to detect a minimum volume ratio of 0.006%, 10 times smaller than the smallest volume ratio reported previously. In Chapter III, we present the development of a nanofluidic resistive-pulse sensor prototype and show that the MOSFET-based resistive-pulse sensing scheme can be successfully extended to the nanoscale.

CHAPTER II

ULTRA-SENSITIVE MOSFET-BASED MICROFLUIDIC RESISTIVE-PULSE SENSOR

2.1 Introduction

In this Chapter, we report the detailed characterization of an ultra-sensitive MOSFET-based microfluidic resistive-pulse sensor used to detect the translocation of small particles through a sensing microchannel. The device connects a fluidic circuit to the gate of a MOSFET and detects particles by monitoring the MOSFET drain current modulation, instead of the modulation of the ionic current through the sensing channel. The minimum volume ratio of the particle to the sensing channel detected is 0.006%, about ten times smaller than the lowest detected volume ratio previously reported in the literature. This volume ratio is detected at a noise level of about 0.6% of the baseline MOSFET drain current, clearly showing the amplification effects from the fluidic circuits and the MOSFETs. We characterize the device sensitivity as a function of MOSFET gate potential and show that its sensitivity is higher when the MOSFET is operating below its threshold gate voltage than when it is operating above the threshold voltage. In addition, we demonstrate that the device sensitivity increases linearly with the applied electrical bias across the fluidic circuit. Finally, we show that polystyrene beads and glass beads of similar sizes can be distinguished from each other based on their different translocation times, and the size distribution of microbeads can be obtained with accuracy comparable to direct

SEM measurements. Part of the work reported in this Chapter has been published in Applied Physics Letters (Xu et al., 2007) and the rest in the Journal of Applied Physics (Sridhar et al., 2008b).

2.2 Device Design & Measurement Setup

The performance of the MOSFET-based resistive-pulse sensor was demonstrated with a microfluidic device fabricated with PDMS microchannels bonded to a glass substrate in conjunction with a commercial MOSFET (2N7000 N-Channel FET, Fairchild Semiconductor Co.), as shown in Fig. 2.1.

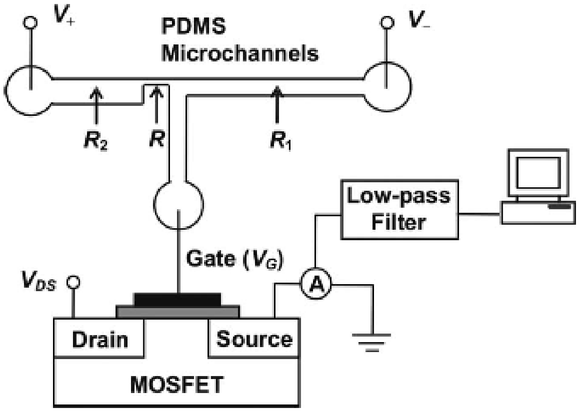

Figure 2.1: The schematic of the experimental setup (not to scale) (Xu et al., 2007). The fluidic and MOSFET circuits are commonly grounded. The resistances of three segments of the horizontal microchannel are denoted as R_2, R, and R_1, respectively.

The microfluidic chip consists of four microchannels, which are all 30 μm deep and fabricated by soft lithography using photolithographically patterned SU-8 as a master. PDMS is poured onto the patterned SU-8 master mold, cured, peeled off after several hours of baking in a convection oven and irreversibly bonded to a clean glass slide using plasma bonding. The left channel (denoted by its resistance R_2) is 7.5 mm long and 800 μm wide, the sensing channel (denoted by its resistance R) is 150 μm long and 16 μm wide, and the right channel (denoted by its resistance R_1) is 15 mm long and 160 μm wide. The vertical microchannel connecting the downstream end of the sensing channel to the gate of the MOSFET is 6 mm long and 300 μm wide. Three reservoirs, each of 3 mm in diameter, were punched through the PDMS to facilitate fluid injection and removal. Platinum wires were used as the source, drain and gate electrodes to connect the fluidic and electronic circuits. An electrokinetic bias ($V_+ - V_-$) was applied using two DC power supplies (Agilent E3612A and Agilent E3617A) to drive microbeads through the microchannels and to facilitate the adjustment of the MOSFET gate voltage.

The performance of the MOSFET was calibrated separately independent of the fluidic circuit before it was used in the experiments. The MOSFET gate voltage was controlled by an accurate voltage source (Keithley 6487). A source-measure unit (Keithley 236) was used to apply a constant drain-source bias, V_{DS}, of either 0.15 V or 0.5 V and to measure the MOSFET drain current. The MOSFET source terminal was commonly grounded with the voltage source and the source-measure unit. Fig. 2.2 shows the measured $I_D^{1/2} - V_G$ curves for the MOSFET when $V_{DS} = 0.15$ V and 0.5 V, respectively. The threshold voltage, V_T, of the MOSFET was determined from the x-intercepts of the $I_D^{1/2} - V_G$ curves in Fig. 2.2 to be $\sim$ 2.1 V when $V_{DS} = 0.15$ V, and $\sim$ 2.2 V when $V_{DS} = 0.5$ V. The slight shift of the threshold voltage observed for different drain-source biases can be attributed to the substrate bias effect (Casey, 1999). The typical commercial MOSFET used has only three terminals for the source, drain and gate electrode and no terminal to control the substrate bias. Therefore, the substrate bias was floating and caused the threshold voltage to shift when the drain-source bias was changed. However, this does not affect our measurements as long as we keep the drain-source bias fixed for each experiment.

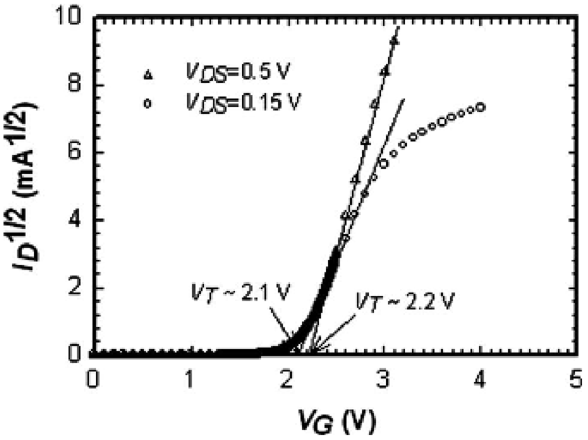

Figure 2.2: $\sqrt{I}_D$ as a function of V_G for a typical MOSFET we used when V_{DS} = 0.15 V and 0.5 V, respectively. The threshold voltage for each case is determined by the value of the x-intercept.

In the experiment, 7.5 mM sodium borate buffered solution (pH value of 9.45) was first filled into the microfluidic circuits and the liquid level in each reservoir was allowed to equilibrate. Then the same borate buffer with dilute suspended polystyrene microbeads was added to the reservoir that would be positively biased. After a short period of time for the liquid level to reach equilibrium again, the electrokinetic bias ($V_+ - V_-$) was applied to induce electroosmotic flow through the horizontal fluidic channel. When a microbead translocates through the sensing microchannel, the conductance of the sensing channel decreases because the sensing channel is partially blocked by the microbead, causing a drop in the ionic current through the channel, which is the most common sensing mechanism of modern resistive-pulse sensors, as explained in detail in Sect. 1.3.1.

However, in the MOSFET-based resistive-pulse sensor, the downstream end of the sensing channel is connected to the gate of a MOSFET and the electrical potential modulation at the end of the sensing channel is monitored by measuring the MOSFET drain current. In our experimental setup, the MOSFET drain current was measured by a current preamplifier (DL Instruments 1211) and the signal passed through a low-pass filter (Stanford Research Systems SR560) before it was fed into the digital data acquisition system. This sensing scheme presents an amplified percentage of modulation to the baseline MOSFET drain current as compared to the percentage of modulation to the baseline ionic current, which is discussed in the next section.

2.3 Theoretical Analysis of the Amplification Effects

In this Section, we present a detailed analysis of the amplification effect. Since the microbeads are in diluted suspension, their effects on the electrical resistance of the large fluidic channels on each side of the sensing channel are negligible. Denoting the increase in resistance of the sensing channel as ΔR when a bead is in the sensing channel, and referring to the resistance of the three segments of the horizontal channels in Fig. 1, the ionic current without (I) and with (I^*) a bead in the sensing channel can be written as

$$
\begin{aligned}
I &= \frac{V_+ - V_-}{R_2 + R + R_1} \\
I^* &= \frac{V_+ - V_-}{R_2 + R + \Delta R + R_1}
\end{aligned}
\tag{2.1}
$$

The gate potentials (V_G) of the MOSFET are then

$$
\begin{aligned}
V_G &= V_- + IR_1 \\
V_G^* &= V_- + I^* R_1
\end{aligned}
\tag{2.2}
$$

The modulation of the gate potential can be derived as

$$\frac{\Delta V_G}{V_G} = \frac{\Delta I R_1}{V_G} = \left(\frac{IR_1}{V_G} . \frac{R}{R_t} \right) . \frac{\Delta R}{R} \tag{2.3}$$

where $\Delta I = I - I^*$ and $R_t = R_1 + R_2 + \Delta R + R$. Eq. 2.3 indicates that the percentage modulation of the gate potential to the baseline gate potential is amplified by a factor of $A_{fluidic} = (IR_1/V_G)(R/R_t)$ compared to the percentage modulation of the channel resistance. This factor is defined as the amplification factor from the fluidic circuit.

A MOSFET can be operated in different regimes, in which the drain current behaves differently as a function of the gate potential. Amplification effects can be achieved when the MOSFET is working in either the saturation region under the conditions of $V_G > V_T$ and $V_{DS} > V_G - V_T$, or in the sub-threshold region under the condition of $V_G < V_T$ because a small change in gate voltage under these conditions leads to a large change in MOSFET drain current as discussed in Sect. 1.4.

When the MOSFET works in the saturation region, the MOSFET drain current modulation as a function of the gate voltage (Casey, 1999; Sze, 1981) can be written as $I_D = k_{sat}(V_G - V_T)^2$, where k_{sat} is a constant. For a small modulation, ΔV_G , the drain current modulation is then

$$\frac{\Delta I_D}{I_D} = \frac{2V_G}{V_G - V_T} \cdot \frac{\Delta V_G}{V_G} \tag{2.4}$$

Combining Eq. 2.3 and Eq. 2.4, we have

$$\frac{\Delta I_D}{I_D} = \left(\frac{2V_G}{V_G - V_T}\right) \cdot \left(\frac{IR_1}{V_G}\right) \cdot \left(\frac{R}{R_t}\right) \cdot \frac{\Delta R}{R} \tag{2.5}$$

So the amplification factor from the MOSFET can be expressed as $A_{FET,sat} = 2V_G/(V_G - V_T)$. To achieve a large total amplification factor, we designed the fluidic circuit as $R_1 = 10R$ and $R_t = 12R$, so as long as the voltage drop across the sensing channel, IR, is larger than $1.2V_G$, $A_{fluidic}$ is larger than 1. For the MOSFET, a large amplification factor can be achieved if $V_G - V_T << V_G$ so the gate voltage selected should be only slightly higher than the threshold voltage.

When $V_G < V_T$, the MOSFET works in the sub-threshold region and the drain current changes exponentially with gate voltage as (Sze et al., 1981)

$$I_D = k_{sub}\left(\frac{q\psi_S}{kT}\right)^{1/2}\left[1 - \exp\left(\frac{-qV_{DS}}{kT}\right)\right]\exp\left(\frac{q\psi_S}{kT}\right) \tag{2.6}$$

where k_{sub} is a constant and q, k and T are the electronic charge, the Boltzmann's constant and temperature, respectively. ψ_S is the surface potential of the MOSFET electronic channel and is given by

$$\psi_S = V_G - V_{FB} - \frac{a^2 kT}{2q}\left\{\left[1 + \frac{4}{a^2}\left(\frac{qV_G}{kT} - \frac{qV_{FB}}{kT} - 1\right)\right]^{1/2} - 1\right\} \tag{2.7}$$

where $a = 2(\epsilon_s/\epsilon_{ox})(d_{ox}/L_D)$. ϵ_s and ϵ_{ox} are the permittivity of the semiconductor and the oxide, respectively. d_{ox} is the thickness of the MOSFET gate oxide, L_D is the extrinsic Debye length, and V_{FB} is the flat-band voltage.

Based on Eqs. 2.3, 2.6, and 2.7, we can derive the theoretical drain current modulation when the MOSFET is working in the sub-threshold region as

$$\frac{\Delta I_D}{I_D} = \left(\frac{qV_G}{kT} - \frac{V_G}{2\psi_S}\right) \cdot \left(\frac{d\psi_S}{dV_G}\right) \cdot \left(\frac{IR_1}{V_G}\right) \cdot \left(\frac{R}{R_t}\right) \cdot \frac{\Delta R}{R} \tag{2.8}$$

This equation is cumbersome to use as we do not have the necessary information such as the dopant concentration, oxide thickness and flat-band voltage to evaluate the variables a and V_{FB}, and hence ψ_S.

In ideal situations, i.e., if we assume there is no fixed oxide charge, interface traps or difference in work function between the semiconductor and the gate metal, and if the diffusion current can be neglected, then ψ_S is approximately equal to V_G. Eq. 2.8 can then be simplified as

$$\frac{\Delta I_D}{I_D} \approx \left(\frac{qV_G}{kT} - \frac{1}{2}\right) \cdot \left(\frac{R}{R_t}\right) \cdot \frac{\Delta R}{R} \tag{2.9}$$

Therefore, an amplification factor for MOSFET working in the sub-threshold regime can be written as $A_{FET,sub} = qV_G/kT - 1/2$. The typical value of q/kT is around 40 at room temperature and for a threshold voltage of 2.1 V, a FET amplification factor of around 80 can be achieved.

2.4 Results and Discussion

2.4.1 Experimental Demonstration of Amplification

The demonstration of the amplification effect was performed with 7.5 mM sodium borate buffer containing polystyrene beads. We first characterized the amplification effect for the MOSFET working in the saturation region by setting $V_{-} = -29$ V, $V_{+} = 11.98$ V, and $V_{DS} = 0.5$ V. The MOSFET gate voltage was inferred from the $I_D^{1/2} - V_G$ curve in Fig. 2 to be ~ 2.31 V so the MOSFET was working in the saturation region. Under these conditions, the calculated amplification factors are $A_{fluidic} = (IR_1/V_G)(R/R_t) = 1.13$, and $A_{FET,sat} = 2V_G/(V_G - V_T) = 42$, yielding a total theoretical amplification factor of 47.46 for the MOSFET drain current modulation compared to the resistance modulation of the sensing channel.

The measured MOSFET drain current as a function of time is shown in Fig. 2.3a when a solution with polystyrene beads of 4.1, 5.9, 7.26, and 9.86 μm-diameter was added. The different-size polystyrene beads can be easily distinguished by the different amplitude of the drain current modulation observed as each microbead was translocated through the sensing channel, which was verified by concurrent observation using an optical microscope (Nikon Eclipse TE-2000U). As pointed by DeBlois & Bean (1970) and Saleh & Sohn (2001), if the diameter of the microbeads is much smaller than the diameter of the sensing channel, the ratio $\Delta R/R$ can be approx-

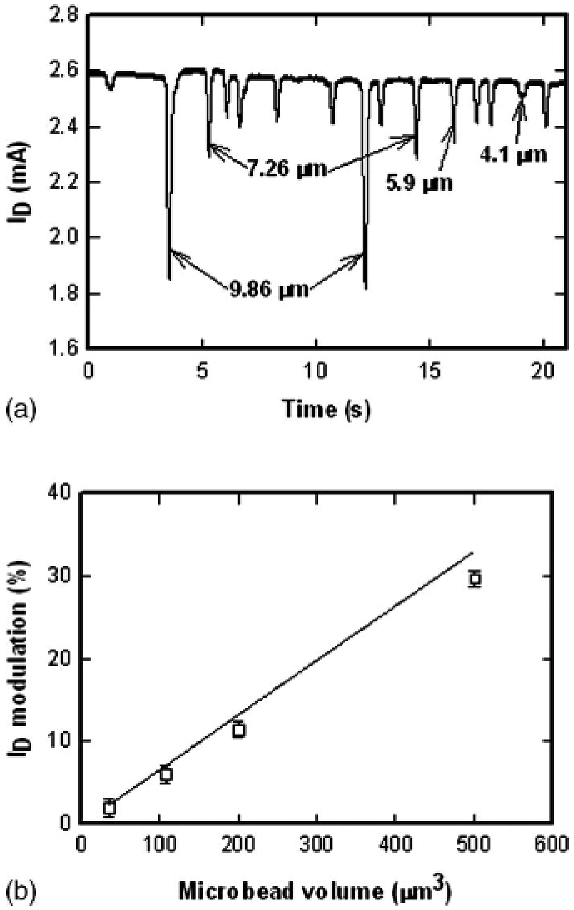

Figure 2.3: (a) The MOSFET drain current modulation as a function of time for a mixture of 4.1, 5.9, 7.26, and 9.86 μm-diameter polystyrene beads when the MOSFET works in the saturation region. (b) The amplitude of the drain current modulation as a function of microbead volume. The points represent experimental values derived from Fig. 2.3a and the solid line represents the theoretical prediction derived from Eq. 2.5.

imated by the ratio of the volume of the microbead to the volume of the sensing channel. Therefore, in Fig. 2.3b we plotted the amplitude of the observed drain current modulation as a function of microbead volume together with the theoretical drain current modulation calculated from Eq. 2.5 using the theoretical amplification factor of 47.46 as derived above. The resistance modulation in the calculation is taken as the volume ratio of the microbead to the sensing channel.

From Fig. 2.3b, it can be seen that the agreement between the theoretical prediction and experimental results is excellent for microbeads of diameter 4.1 and 5.9 μm, and quite good for microbeads of diameter 7.26 μm. However, for the 9.86 μm-diameter beads, there is a difference of about 17.8 % between the theory and the experiment. We believe this is related to the fact the MOSFET is working close to the threshold voltage, and its I-V relation is highly non-linear. Therefore, Eq. 2.4 may not be very accurate for the relatively large modulation from the 9.86 μm-diameter beads. The volume ratio of the 9.86 μm beads to the sensing channel is only 0.7 %, so one might think that the voltage modulation is still small. However, with the 47.46 times amplification, Eq. 2.5 will lead to a hundred percent MOSFET drain current modulation for a 2.1 % resistance modulation (or volume ratio if the resistance modulation is regarded to be equal to the volume modulation).

In addition to characterizing the device for the MOSFET working in the saturation regime, we also characterized the device performance for the MOSFET working in the sub-threshold regime by setting $V_- = -58$ V, $V_+ = 19.56$ V, and $V_{DS} = 0.15$ V. In this case, the gate voltage is derived to be $\sim$1.7 V in the same manner as above, smaller than the threshold voltage for $V_{DS} = 0.15$ V. Thus, the MOSFET was working in the sub-threshold regime. The amplification factors from the fluidic circuit and the MOSFET are $A_{fluidic} = 1.5$ and $A_{FET,sub} = 67.5$ respectively, giving a total theoretical amplification factor of 101.25 with respect to the resistance modulation of the sensing channel. The total amplification factor is more than twice of the total amplification factor for the MOSFET working in the saturation regime (47.46).

To demonstrate the enhanced amplification effect, we added the sodium borate buffer with a mixture of 2 μm and 9.86 μm-diameter polystyrene beads to the fluidic circuits and the measured MOSFET drain current as a function of time is shown in Fig. 2.4. Fig. 2.4 shows that with the higher amplification factor in the sub-threshold regime, we were able to detect particles as small as 2 μm in diameter, which has a volume ratio to the sensing channel of about 0.006 %, or ten times smaller than the

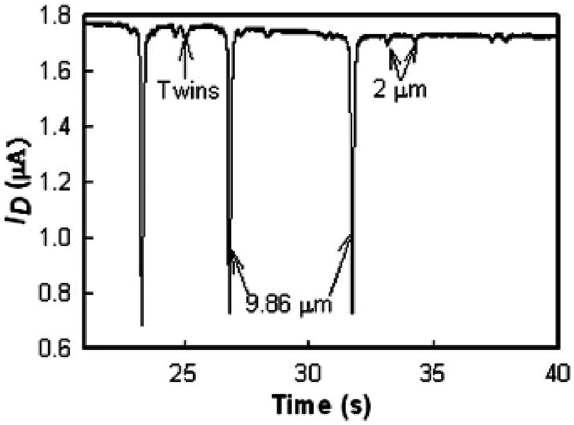

Figure 2.4: The MOSFET drain current modulation as a function of time for a mixture of 2 and 9.86 μm-diameter microbeads when the MOSFET works in the sub-threshold region. “Twins” in the figure indicates a group of two beads that translocate together through the sensing channel.

smallest volume ratio previously reported in the literature, 0.06 %, (DeBlois & Bean, 1970).

The modulations shown in Figs. 2.3a and 2.4 are triangular in shape because the rise time of the current preamplifier was set to 100 ms, which was comparable to the time taken for the beads to translocate through the sensing channel ($\sim$ 300 ms). Hence, due to signal integration, we do not observe an ideal rectangular-shaped signal. However, the long rise time was required only because we tried to do concurrent electrical and optical measurements of particle translocation through the sensing channel and did not have a Faraday cage large enough to contain the whole set up. In real applications where only the electrical signal is desired, the set-up can be shielded with a Faraday cage and a much shorter rise time can be used. This has been verified and Fig. 2.5 shows the MOSFET drain current as a function of time when we added the sodium borate buffer with microbeads of 5.9 μm in diameter to our fluidic circuits shielded in a Faraday cage.

For this experiment, $V_{DS} = 0.15$ V, $V_+ = 9.03$ V, $V_- = -26.3$ V, and the rise time of the current preamplifier is 0.3 ms with a cut-off frequency of the low-pass filter set as 100 Hz. As can be seen from Fig. 2.5, the microbead translocation signals observed have a shape close to the ideal rectangular shape, where the flat region at the bottom corresponds to the microbead traversing the sensing channel. In addition, in Fig. 2.5 we also observed overshooting of the MOSFET drain current signal when the microbead enters the sensing channel, which may be due to sudden resistance and capacitance changes caused by the microbead.

It is worth noting that direct measurement of the ionic current through the fluidic

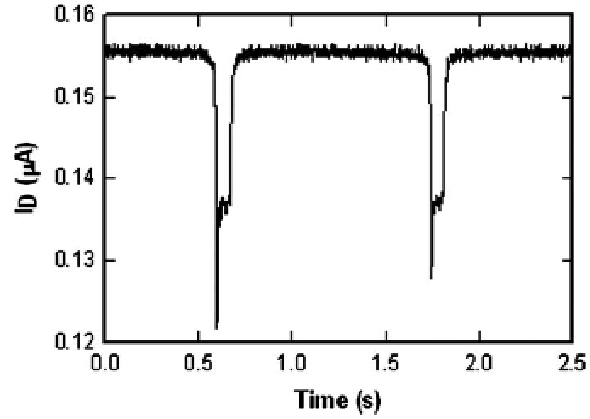

Figure 2.5: The MOSFET drain current modulation as a function of time for 5.9 μm-diameter microbeads when the rise time of the current preamplifier is set to 0.3 ms. The experimental setup was shielded in a Faraday cage, and $V_{DS} = 0.15$ V, $V_+ = 9.03$ V, $V_- = -26.3$ V.

circuit with the same instrument shows no discernible dips when microbeads pass through the channel, as evidenced by concurrent optical observation. Fig. 2.6 shows the measured ionic current through the fluidic circuit when the solution with 9.86 μm-diameter polystyrene beads was driven through the sensing channel. No discernible

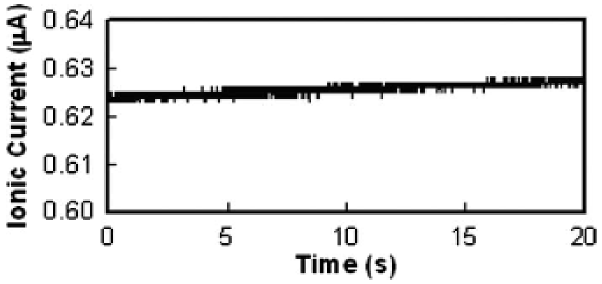

Figure 2.6: Measured ionic current in the fluidic circuit for the microbeads suspension containing 9.86 μm polystyrene beads.

dips can be observed from the ionic current measurement.

2.4.2 Noise Analysis

The sensitivity and limitation of any experimental measurement is ultimately dominated by noise and a more sensitive sensing scheme has to provide a higher signal to noise ratio. The MOSFET-based resistive-pulse sensor provides a higher percentage modulation compared to the percentage modulation to the baseline ionic current for traditional resistive-pulse sensors. However, the concept is useful only if the noise level does not increase to the same extent. If we define the noise level as the ratio of the peak to peak value of the noise to the average baseline value of the signal, then in our measurement, the noise level of the ionic current through the fluidic circuit was about 0.3 %, and the noise level of the MOSFET drain current was between 0.5 - 0.9 %, which varied from one experiment to another. Note that the noise level of the ionic current in the literature ranges from ~ 0.02 % (DeBlois & Bean, 1970) to more than 10 % (Heng et al., 2004) so the noise level we observed is comparable to those reported in the literature.

As discussed in the Sect. 2.4.1, the percentage of modulation can be magnified from 47.46 to 101.25 times depending on the working regime of the MOSFET and applied electrokinetic bias. In comparison, the noise level of the MOSFET drain current is only 2 to 3 times higher than that of the ionic current through the fluidic channel. So compared to the traditional resistive-pulse sensors, the reported MOSFET-based resistive-pulse sensor demonstrates an enhanced sensitivity of up to 50 times. (The sensitivity here is defined as the ratio of the percentage modulation from the particles to the noise level). The true advantage of the MOSFET-based resistive-pulse sensor is that the design amplifies the percentage of the resistance modulation locally.

Recently, there have been several discussions about the noise of nanopore-based resistive-pulse sensors (Ziwy & Fulinsky, 2002; Chen et al., 2004b; Smeets et al., 2006; Tabard-Cossa et al., 2007; Smeets et al., 2008; Uram et al., 2008). All of these reports indicate that the main sources of noise in resistive-pulse sensors are: (a) thermal and shot noise generated by the current preamplifier, (b) thermal noise due to the nanopore device itself, (c) dielectric noise due to the substrate material, and (d) low-frequency flicker (1/f) noise. Recently, the flicker noise has been shown to be inversely proportional to the number of charge carriers inside the nanopore (Smeets et al., 2008). This suggests that the flicker noise could be due to fluctuations in the mobility of the ions in the electrolyte (Tabard-Cossa et al., 2007). However, the origin of the flicker noise has yet to be fully understood. In addition to fluctuations in mobility, surface effects like the inhomogeneity of the surface charge on the pore wall (Chen et al., 2004b), nanobubble formation (Smeets et al., 2006) and the underlying motions of biological membrane channels (Ziwy & Fulinski, 2002) have been proposed as possible sources of the flicker noise. To better understand the noise source in our measurement system, we performed spectral analysis of our data.

Fig. 2.7 shows the power spectra of measured baseline MOSFET drain current for two cases: no Faraday cage with 100 ms rise time setting for the current preamplifier, and with Faraday cage with 0.3 ms rise time setting for the current preamplifier. The power spectra are expressed in units of db with a reference of 1 $A^2\Omega$. The solid line shows the power spectrum density (PSD) of the baseline MOSFET drain current

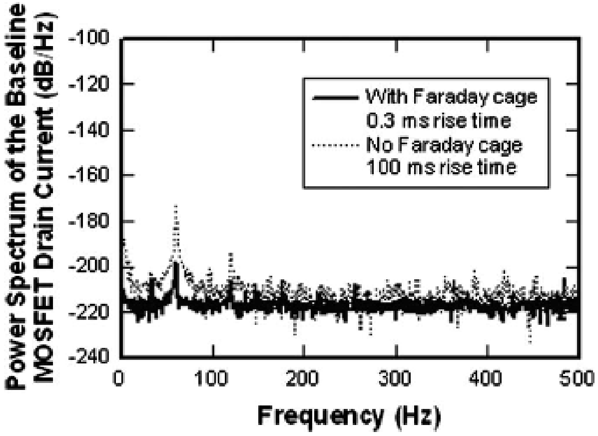

Figure 2.7: Power density spectrum (PSD) of the baseline MOSFET drain current for the cases of with and without Faraday cages.

shown in Fig. 2.5 when the experimental setup was shielded with a Faraday cage, and the dotted line shows the PSD of the baseline MOSFET drain current shown in Fig. 2.4 when a Faraday cage was not used. Fig. 2.7 indicates that in addition to the 1/f flicker noise at very low frequency (<10 Hz), noise at 60 Hz and its harmonic frequencies are present in our measurement. Fig. 2.7 indicates that the 60 Hz noise can be reduced to an acceptable level by using a short rise time for the current preamplifier and shielding the experimental setup with a Faraday cage.

It is worth noting that we did not shield our experimental setup using a Faraday cage because at the experimental characterization stage, we wanted to perform concurrent optical observations to validate the electrical signals. The noise suppression in the above reported results is mainly achieved by a relatively large rise time of the current preamplifier (100 ms) and a low cut-off frequency (30 Hz) of the low-pass filter, which may not be desirable for some applications. However, this is because the measurements were performed in open space without a Faraday cage, which is used in nearly all other resistive-pulse sensors. Further noise characterization showed that if shorter rise time was used, the observed noise was mainly 60 Hz, which can be eliminated by using a Faraday cage, as shown in Fig. 2.5. Using a Faraday cage to shield the measurement set-up can help to achieve a noise level of 0.4 % (ratio of the peak to peak value of the noise to the average baseline value of the signal) with a much shorter rise time of the current preamplifier (0.3 ms), and a much higher cut-off frequency of the low-pass filter (1 kHz).

2.4.3 Device Sensitivity as a function of V_G

As demonstrated above, the amplification of the sensing channel resistance modulation is a function of the MOSFET gate voltage and depends on the MOSFET operating region, as shown in Fig. 2.8. The characterization was performed with 7.5 mM sodium borate buffered solution with 9.86 μm in diameter polystyrene microbeads and the settings of the power supplies were $V_{DS} = 0.15$ V and $V_- = -29$ V. In the experiment, the MOSFET gate voltage was varied by adjusting V_+. It can be clearly seen from Fig. 2.8 that the amplification factor varies continuously as the gate voltage changes and the amplification effect is more significant when the MOSFET works in the sub-threshold region. In the sub-threshold region, the MOSFET drain current modulation only changes marginally with the MOSFET gate voltage, while in the region above threshold, the drain current modulation decreases as the MOSFET gate voltage increases.

The calculated values of the MOSFET drain current modulation as a function of

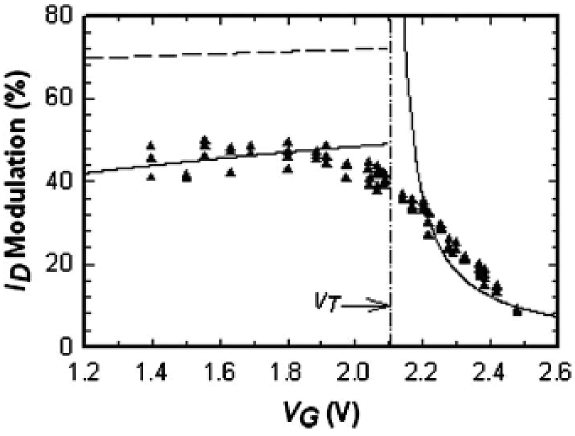

Figure 2.8: Drain current modulation for polystyrene microbeads of diameter 9.86 μm as a function of gate voltage with $V_{-} = -29$ V, $V_{DS} = 0.15$ V. V_{+} was adjusted to obtain different gate voltages on the MOSFET. The points represent experimental data and the solid curves represent theoretical prediction based on Eqs. 2.5 and 2.8. The dashed line represents the approximate theoretical prediction in the sub-threshold region based on Eq. 2.9.

the gate voltage are also shown in Fig. 2.8. In the saturation region, the theoretical prediction based on Eq. 2.5 fits the experimental results very well except in the transition region close to the threshold voltage. However, a significant difference was observed between the experimental results and the theoretical prediction (Eq. 2.9) in the sub-threshold region. This discrepancy indicates that the assumption that $\psi_S \sim V_G$ is not a good approximation in this case. Therefore, we fitted the experimental data in the sub-threshold region to Eq. 2.8, which reflects the more realistic performance of the MOSFET. A set of fit parameters of $a = 6.6$ and $V_{FB} = -0.3$ V yielded an acceptable theoretical curve that fit the experimental data. These values are reasonable as the typical value of a ranges from 0.3 - 30, and V_{FB} depends on the material used for the gate metal and typically ranges from -0.5 to 0.5 V, as stated by Sze (1981).

Note that the vertical spread in the data can be attributed to the intrinsic size dispersion of the 9.86 μm microbeads used and this vertical spread is greater in the sub-threshold region compared to that in the above-threshold region. This is because the device is more sensitive to the resistance change caused by bead size dispersion when the MOSFET is operating in the sub-threshold region since the total amplification factor is larger in this region as shown in the previous section.

2.4.4 Device Sensitivity as a function of Applied Electrokinetic Bias

As mentioned above, the amplification factor is also a function of current through the fluidic circuit, and hence a function of the applied electrokinetic bias. The device sensitivity is expected to vary linearly with V_- because ideally, the IR_1 term in Eqs. 2.3, 2.8 and 2.9 is equal to $V_G - V_-$. When the MOSFET is operating in the sub-threshold region the drain current modulation given by Eq. 2.9 is:

$$\frac{\Delta I_D}{I_D} \approx \left(\frac{q}{kT} - \frac{1}{2V_G}\right) \cdot (V_G - V_-) \cdot \left(\frac{R}{R_t}\right) \cdot \frac{\Delta R}{R} \tag{2.10}$$

The dependence of the drain current modulation on V_- is similar in the saturation region with the same IR_1 substitution made in Eq. 2.5.

The drain current modulation of 9.86 μm-diameter polystyrene microbeads was measured as a function of V_-, while holding the MOSFET gate voltage constant at about 1.81 V. The MOSFET was operating in the sub-threshold region. This was achieved by adjusting V_+ accordingly to keep the measured MOSFET drain current constant. Fig. 2.9 shows the performance of our device as a function of V_{-} and a linear relationship between the drain current modulation and V_{-} is clearly observed as expected.

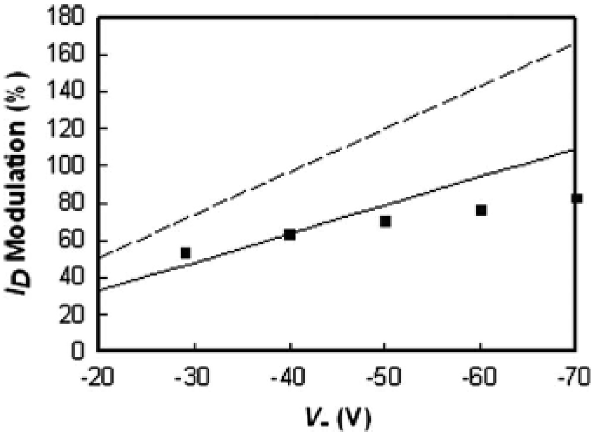

Figure 2.9: Drain current modulation for 9.86 μm polystyrene microbeads as a function of V_{-}, for constant gate voltage of $\sim$ 1.81 V and $V_{DS} = 0.15$ V. The points represent experimental data and the solid line represents the theoretical prediction based on Eq. 2.8 and the dashed line represents the theoretical prediction based on Eq. 2.10.

The theoretical prediction based on Eq. 2.10 is also presented in Fig. 2.9 as the dashed line and again, some discrepancy is observed between the experimental results and the theoretical prediction, which confirms the observation in the previous section that the approximation that $\psi_S \sim V_G$ is not a very good one. However, using Eq. 2.8 with the same fitting parameters ($a = 6.6, V_{FB} = -0.3$ V) as in the previous section (Fig. 2.9, solid line), results in a much better match between the calculation and experiment. We were not able to measure drain current modulations for $|V_{-}| < 29$

V because the electroosmotic flow was very slow and most of the beads stick to the channel walls after a short time of experiment.

2.4.5 Detection of Particles with Similar Sizes but Different Surface Charges

We tested the ability of our device to distinguish two similarly-sized microbeads with different surface charges. Nominally 4.84 μm-diameter polystyrene and 4.8 μm-diameter glass microbeads were used to test this capability of the device. Glass microbeads are known to have relatively large negative surface charge density (Behrens & Grier, 2001) in aqueous electrolyte solutions and will experience an electrophoretic force that opposes the electroosmotic flow of the microbeads (Li, 2004). Therefore, the net speed of the glass beads through the small microchannel will be reduced and the translocation time of the glass beads through the sensing channel should be longer than that of the polystyrene beads of much lower surface charges. Fig. 2.10 shows the MOSFET drain current as a function of time when we added a mixture of the above-mentioned polystyrene and glass beads. The power supply settings are $V_{-} = -29.1$ V, $V_{+} = 11.52$ V, $V_{DS} = 0.15$ V. The MOSFET gate voltage was ~ 1.84 V so the MOSFET was operating in the sub-threshold region.

As expected, the magnitude of drain current modulation observed for both types of microbeads is very similar because of their similar size. The glass microbeads took a longer time to translocate through the sensing channel compared to the polystyrene microbeads as evidenced by the width of the drain current modulations. This has been confirmed by concurrent optical observations with the optical microscope. In fact,

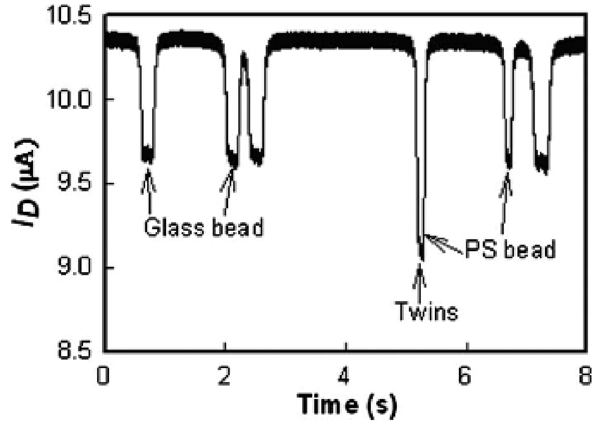

Figure 2.10: MOSFET drain current as a function of time for a mixture of 4.8 μm-diameter glass and 4.84 μm-diameter polystyrene microbeads with $V_{-} = -29.1$ V, $V_{+} = 11.52$ V, and $V_{DS} = 0.15$ V. The gate voltage of the MOSFET is determined to be about 1.84 V so the MOSFET is operating in the sub-threshold region.

the time taken for the glass microbeads to translocate through the sensing channel was $\sim$ 600 ms, in comparison with $\sim$ 400 ms for the polystyrene microbeads. This shows the ability of our device to distinguish particles of similar size but different surface charges.

2.4.6 Characterization of microbead size distribution

A useful function of a standard resistive-pulse sensor is to detect the size of particles. To characterize the devices ability of detecting the size distribution of microbeads, we measured the size distribution of the nominally monodisperse 9.86 μm-diameter polystyrene beads with the MOSFET-based resistive-pulse sensor. We also measured the diameter distribution of the polystyrene beads with a scanning electron microscope (Raith eLiNE SEM). The manufacturer (Bangs Laboratories, Inc) quoted nominal mean sphere diameter of the beads is 9.86 μm with a standard deviation of 0.65 μm, as measured with a Coulter Principle-based particle sizer. The measurement with the MOSFET-based resistive-pulse sensor was performed with the following parameters: $V_{-} = -29$ V, $V_{+} = 11$ V, and $V_{DS} = 0.15$ V, leading to $V_G \sim 1.79$ V. Thus, the MOSFET was working in the sub-threshold region.

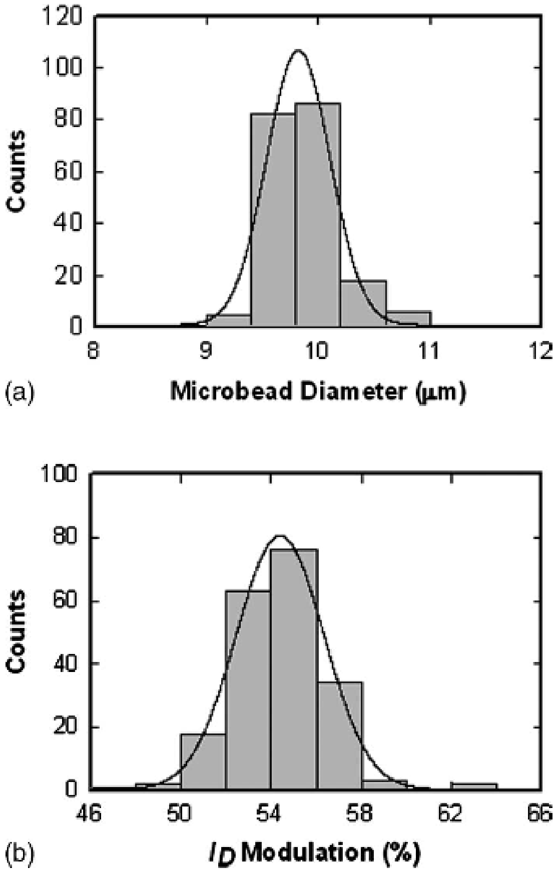

Figure 2.11: (a) Size distribution of 9.86 μm-diameter polystyrene microbeads obtained from SEM measurements, (b) Distribution of drain current modulation observed for 9.86 μm-diameter microbeads. Vertical bars represent a histogram of experimental data and the lines represent a Gaussian fit to the data.

Fig. 2.11a shows the size distribution of the 9.86 μm-diameter microbeads obtained with the SEM, in which the vertical bars represent a histogram of experimental data and the curve represents a Gaussian fit to the data. The diameters of a total of 199 microbeads were directly measured using the SEM, and a mean microbead diameter of 9.82 μm with a standard deviation of $\sigma = 0.29$ μm was obtained from the Gaussian fit to the data. Thus, the direct SEM measurements showed that the size distribution of the 9.86 μm beads was about half of the quoted value from the bead manufacturer. Fig. 2.11b shows the distribution of drain current modulations observed using the MOSFET-based resistive-pulse sensor when 9.86 μm in diameter polystyrene beads were translocated through the sensing channel. The total number of samples was kept the same as that for the SEM measurement, and from the Gaussian fit to the data, a mean drain current modulation of 54.4 %, with a standard deviation of $\sigma = 1.95$ %, was obtained.

To enable a direct comparison between the size distribution obtained between the two measurements, the data were normalized by the mean of the respective Gaussian distributions: 9.82 μm for the SEM data and 54.4 % for the MOSFET-based resistive-pulse sensor. Fig. 2.12a shows the normalized data from the SEM measurement and Fig. 2.12b shows the normalized data from the MOSFET-based resistive-pulse sensor measurement. Because of the normalization, the mean in both Figs. 2.12a and 2.12b was 1.0. The standard deviation for the normalized SEM data shown in Fig. 2.12a was 0.028 and the corresponding value for the normalized MOSFET-based resistive-pulse sensor data shown in Fig. 2.12b was 0.035. Therefore, the size distribution of 9.86 μm in diameter beads measured with the two techniques matches rather well.

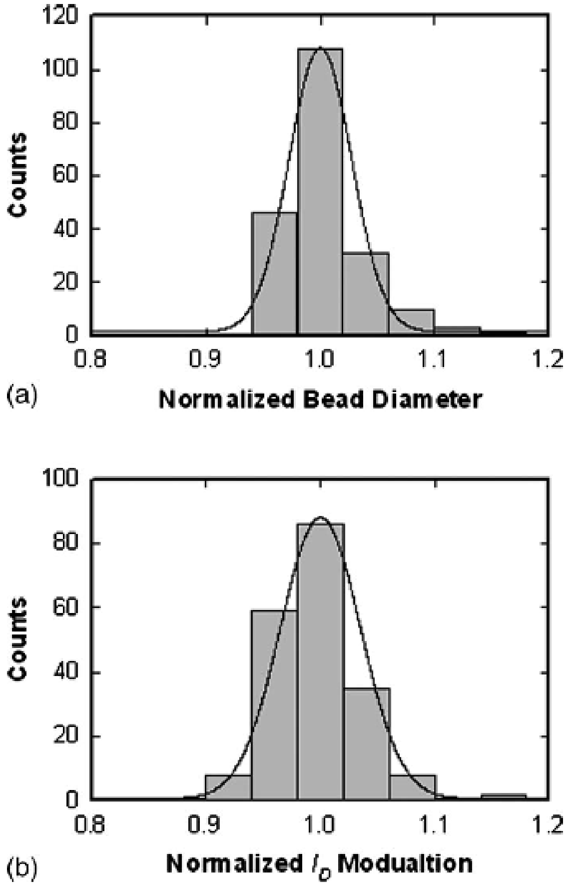

Figure 2.12: (a) Normalized size distribution of 9.86 μm-diameter microbeads obtained by direct SEM measurement. The normalized mean was 1.0 and the standard deviation was 0.028, (b) Normalized size distribution of 9.86 μm-diameter microbeads obtained using the MOSFET-based resistive-pulse sensor. The normalized mean and standard deviation were 1.0 and 0.035 respectively.

It is worth noting that for the normalized distribution of spherical particles, we expected the standard deviation from the MOSFET-based resistive-pulse sensor to be 3 times of the standard deviation from the diameter measurement of the SEM, as the signal from the resistive-pulse sensor is proportional to the volume of the beads. However, the observed standard deviation from the counter is only slightly higher than that from the SEM measurement. A full analysis of this difference will depend on understanding the intrinsic resolution of each probe and the manner in which the resolution function couples to the actual data.

2.5 Summary

In summary, we report the detailed experimental characterization of a design of the microfluidic resistive-pulse sensor and demonstrate that this MOSFET-based resistive-pulse sensor can increase the sensitivity by amplifying the percentage of the modulation caused by the translocation of particles through the sensing channel. The detected minimum volume ratio between the particle and the sensing channel is about 0.006 %, ∼10 times smaller than the lowest volume ratio previously reported in the literature. The sensitivity of the MOSFET-based resistive-pulse sensor has been characterized as a function of MOSFET gate voltage showing that the device is more sensitive when operated in the sub-threshold region as compared to the saturation region. In addition, the sensitivity with respect to the applied electrokinetic bias, V_{-}, has been investigated and it is shown that the drain current modulation varies linearly with V_{-}. The MOSFET-based resistive-pulse sensor can distinguish particles of both different sizes and of similar size but different surface charges, based on the observed amplitude of the MOSFET drain current modulation and the translocation time. It is shown that the size dispersion of 9.86 μm in diameter polystyrene beads measured with the MOSFET-based resistive-pulse sensor is comparable to that from direct SEM observation.

CHAPTER III

MOSFET-BASED NANOFLUIDIC SENSOR

3.1 Introduction

In Chapter II, we discussed a new MOSFET-based sensing scheme which has reduced the minimum volume ratio detectable by resistive-pulse sensing by a factor of 10 from 0.06% to 0.006%. In this Chapter, we present the extension of this sensing scheme to the nanoscale. By reducing the dimensions of the sensing channel to the nanoscale, we extend the detection capabilities to sensing nanoparticles. The fabrication of a nanofluidic sensor in PDMS and glass, and the experimental setup used for our experiments are presented first. Next, we analyze the theoretical performance of our nanofluidic sensor, and then demonstrate the capability of our nanofluidic sensor to detect 210 nm-diameter polystyrene nanobeads. Finally, we discuss the valuable insights that we have learned during our experimental process which will enable us to further improve the performance and capability of the nanofluidic sensor in the future.

3.2 Nanofluidic Sensor Fabrication & Measurement Setup

3.2.1 Nanofluidic Sensor Fabrication

The nanofluidic sensor fabrication process consists of a sequence of electron lithography, silicon micromachining techniques, UV photolithography and soft lithography.

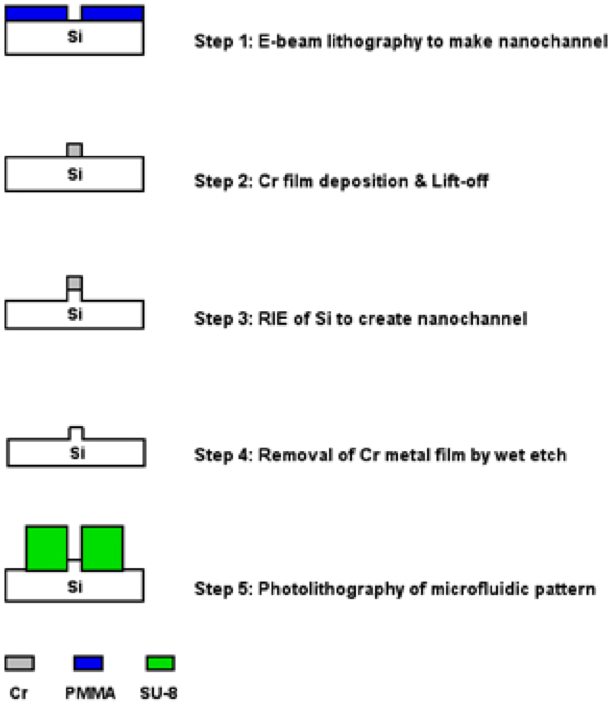

Figure 3.1: Brief outline of the steps involved in the fabrication of the nanofluidic sensor master mold. The substrate was a 4" silicon (100) wafer.

A silicon master mold, which was later used for making PDMS device copies using soft lithography, was first fabricated. A brief outline of this fabrication process is shown in Fig. 3.1. We began with a Si (100) wafer, 4" in diameter, first cleaned using a piranha etch to remove any organic contaminants on the surface of the wafer. The piranha etch consisted of two steps. First, the wafer was immersed in a 1:4 mixture by volume of hydrogen peroxide and sulfuric acid at 120 °C for 10 mins, and then rinsed thoroughly with deionized (D.I.) water. Then, the wafer was immersed in a 1:10 mixture by volume of hydrofluoric acid and D.I. water for 10-20 seconds, and then rinsed thoroughly with D.I. water. 495 PMMA A6 resist (MicroChem Corp.)

was then spun onto the entire surface of the 4" wafer using a two-step spin program with a 5 s slow spin at 500 rpm with acceleration of 1260 rpm/s followed by a fast spin for 50 s at 4000 rpm also with an acceleration of 1260 rpm/s. The wafer was then removed from the spinner and placed on a hotplate set at 180 °C for 60 s. This step is usually referred to as a pre-bake or soft-bake and evaporates the solvents in the resist and helps to densify the resist. Based on ellipsometry measurements, the thickness of the PMMA film after the soft-bake step was estimated to be $\sim$ 325 nm.

Next, the nanochannel portions of the nanofluidic device were patterned using electron beam lithography. We used a Raith eLINE electron beam lithography tool, with an accelerating voltage of 30 kV and an aperture size of 10 μm for our exposures. At this setting, the beam current, measured at the Faraday cup on the sample holder, was typically around 0.04 nA. Area mode exposures with a step size of 10 nm were used to write the patterns, and the optimal exposure dose was determined experimentally to be 350 μC/cm^2. A typical pattern written using the electron beam lithography tool is shown in Fig. 3.2. PMMA is a positive resist, so the regions that are colored in Fig. 3.2 were exposed to the electron beam, and the polymer was broken into fragments in these regions. The average patterning time for a 4" wafer containing 8 such patterns and 2 large alignment crosses (5 $\mu m \times$ 1000 μm) was approximately 45 mins.

After the patterning was done, the wafer was immersed in MIBK:IPA (1:3 by volume) developer solution for 30 s, rinsed thoroughly in IPA for $\sim$ 1 min and blown dry using compressed dry air. The developer dissolved away the portions of the resist that were fragmented due to the electron beam exposure. The wafer was then placed

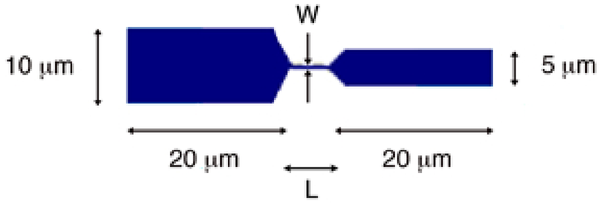

Figure 3.2: Schematic of an individual nanochannel pattern written using electron beam lithography. Eight such patterns, along with two alignment crosses, were written on a single 4" wafer. The length, L, of the nanochannel is varied between 2 and 5 μm, and the width, W, is varied between $\sim$ 300 and 500 nm for the eight patterns.

on a hotplate set at 100 °C for 60 s. This step is called post-exposure bake or hard-bake and serves to stabilize and harden the developed photoresist prior to further processing.

Next, a 60 nm thick Cr film was deposited on top of the wafer using electron beam evaporation. 5 keV electrons were used to evaporate Cr off a pure target onto the substrate. Typically, a deposition rate of $\sim$ 2 Å/s was used to deposit a uniform film of Cr on top of the patterned PMMA film. The wafer was then immersed into a beaker of hot acetone, which was placed on a hotplate set at 110 °C, for about 2 mins to lift off the unpatterned PMMA and the Cr on top of it. The beaker containing the wafer was then removed from the hotplate, and the wafer was transferred into a separate beaker containing fresh acetone at room temperature for $\sim$ 2 mins. Once the Cr film appeared to be cleanly removed from most of the wafer surface, the wafer was rinsed thoroughly in IPA for $\sim$ 2 mins and blown dry using compressed dry air. At this stage, the alignment markers were quite clearly visible to the naked eye, and served as visual confirmation that the processing was successful so far.

The actual thickness of the deposited Cr film was then measured to be ~ 62 ± 5 nm using a surface profilometer (Veeco Dektak 150). The nanochannel pattern was then transferred to the silicon wafer by reactive ion etching using the Cr film as an etch mask. A fluorine-based reactive ion etcher (Trion Phantom II) with a SF_6-based etch recipe was used with the following parameters: Power = 75 W, Pressure = 25 mTorr, SF_6 flow = 30 sccm, O_2 flow = 5 sccm, Process time ~ 100 s. With this etch recipe, the effective etch rate of silicon in the presence of a Cr etch mask was experimentally determined to be ~ 5 nm/s. The remaining Cr film was then removed from the silicon wafer by immersing the wafer in a HCl:D.I. water (3:1 by volume) mixture for ~ 2 mins, followed by a thorough rinsing in deionized water for 2 mins. The wafer was then blown dry using compressed dry air. Surface profilometry measurements were done to measure the final height of the nanochannel structures and the measured heights were typically ~ 520 ± 50 nm as expected.

The wafer was then piranha cleaned, in the same manner as described earlier, to remove any contaminants from the wafer surface before the next photolithography step. SU-8 2005 photoresist (MicroChem Corp.) was then spun onto the wafer in a two-step spin process - 10 s at 500 rpm with acceleration of 100 rpm/s, and 30 s at 2500 rpm with acceleration of 300 rpm/s. The wafer was then soft-baked on a hotplate set at 95 °C for 2 mins. Photolithography was done using a Karl Suss MA-6 mask aligner to pattern microfluidic channels and reservoirs connecting the nanochannel portions fabricated using electron beam lithography. Fig. 3.3 shows a schematic of the photomask used for this process.

The photomask was first aligned to the substrate using the alignment crosses

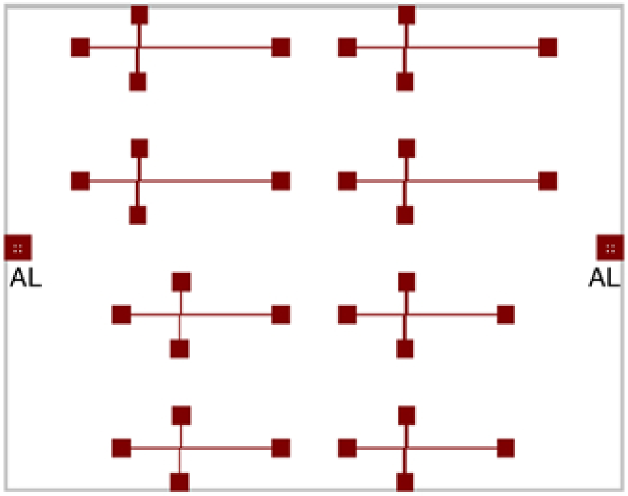

Figure 3.3: Schematic of the bright-field chrome photomask used for photolithography process. The patterns shown in this figure were the only regions transparent to the UV light used for photoexposure. 8 nanofluidic sensors were fabricated on a single 4" silicon wafer, and there were two alignment markers labeled "AL" that enable the alignment of the photomask to the silicon wafer substrate. The photomask was made for us by the Microfabrication Laboratory at University of California at Berkeley.

that were made during the electron beam lithography step. Typically the error in alignment between the substrate and the photomask was less than three microns. The optimum SU-8 exposure dose was experimentally determined to be $\sim 90\ \mathrm{mJ/cm^2}$, and soft contact exposure mode was used. A post-exposure bake was then done before developing the resist by placing the wafer on a hotplate set at 95 °C for 4 mins. This step selectively cross-links the exposed portions of the SU-8 photoresist so that they will be resistant to the developer in the following step. The wafer was then allowed to cool down to room temperature and immersed in SU-8 developer solution (MicroChem Corp.) for 60 s. Only the patterns that were exposed to the UV light and hence selectively cross-linked, remained on the wafer. The rest of the photoresist was dissolved away by the developer. The wafer was then rinsed thoroughly in IPA and blown dry using compressed dry air. Next, the wafer was hard-baked on a hotplate set at 200 °C for ∼ 10 mins to improve the mechanical stability of the SU-8 features by further cross-linking of the material. This step enhances the durability of the master mold, and enables us to re-use the same mold to fabricate several batches of PDMS devices using soft lithography.

Next, the master mold was treated with 1*H*,1*H*,2*H*,2*H*-Perfluorooctyl-trichlorosilane (Sigma Aldrich) in a vacuum desiccator for ∼ 4 hours to make the SU-8 surface hydrophobic. This step reduces adhesion between the SU-8 master mold and the PDMS that is cast onto it during soft lithography, thus enabling us to cleanly and easily peel off PDMS device copies from the master mold after it has cured. The wafer was then rinsed thoroughly with D.I. water to remove any residuals from the wafer surface. The master mold was then used to repeatedly fabricate devices in PDMS using soft lithography.

PDMS (10:1, polymer:curing agent by mass) was then poured onto the master mold and the wafer was degassed for ∼ 4 hours to remove any bubbles present in the PDMS. The mold was then baked in a convection oven set at 65 °C for ∼ 4 hours. Individual devices were then cut and peeled off from the mold. Reservoirs were punched through using a 3 mm-diameter blunt, and the devices were irreversibly bonded to clean glass coverslips using plasma bonding. The silane treatment of the master mold, and PDMS soft lithography steps were performed in the Vanderbilt Institute for Integrative Biosystem Research and Education (VIIBRE) microfabrication laboratories. One such PDMS-based device is shown in Fig. 3.4. Each device was used only for

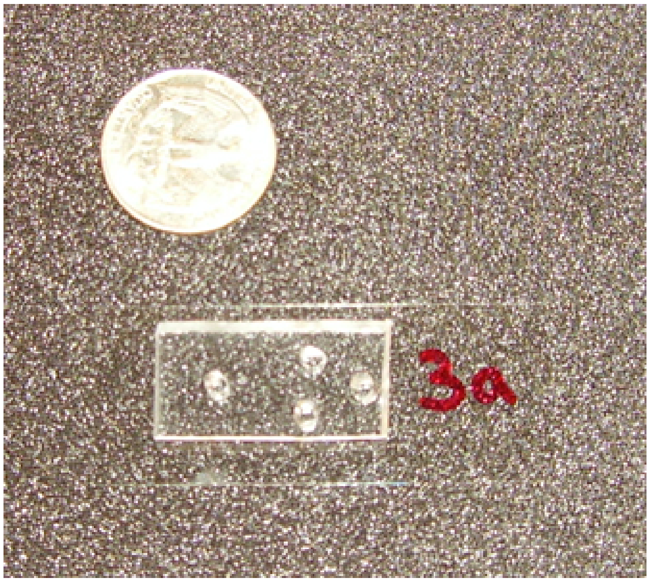

Figure 3.4: Picture of an actual nanofluidic device fabricated in PDMS and bonded to a glass coverslip. A quarter coin is shown above the device for scale.

experiments on a single day, after which it was discarded.

3.2.2 Measurement Setup

Fig. 3.5 shows a schematic of the nanofluidic sensor and the electronic circuit used in all of our experiments. The dimensions of all the channels in the nanofluidic circuit are listed in Table 3.1. Fig. 3.6 shows a SEM micrograph of the nanochannel portion connecting channels A and D, as it appears on the master mold. All channel dimensions were measured on the master mold because it was difficult to make these measurements in the actual PDMS devices themselves. So we assumed that the actual dimensions of the channels in PDMS were approximately the same as the channel dimensions on the master mold.

As is evident from Fig. 3.5, we have used designed the nanofluidic circuit has

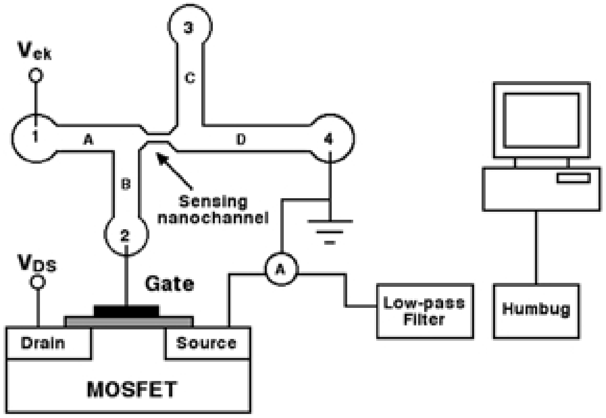

Figure 3.5: Schematic of experimental setup (not to scale). The power supplies and current preamplifier are commonly grounded.

Table 3.1: Dimensions of the channels of the nanofluidic sensor used in our experiments

Channel Label	Length (μm)	Width (μm)	Height (μm)
A	6000	50	5
B	3000	100	5
C	11000	10	5
D	3000	100	5
Nanochannel	5	0.35	0.5

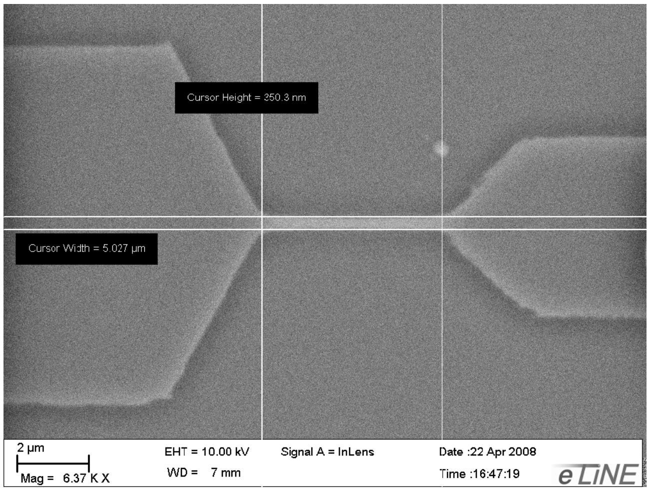

Figure 3.6: SEM micrograph showing the dimension of the sensing nanochannel portion of the nanofluidic device used in our experiments. The nanochannel is ~ 350 nm wide, 5 μm long and 500 nm deep. This image was taken on the master mold.

four microchannels as opposed to three for the microfluidic circuit discussed in Chapter II. We originally added an extra vertical microchannel to our design to aid the electro-osmotic delivery of nanoparticles to the sensing nanochannel. However, during the course of our experiments, we found electro-osmosis to be an ineffective way of delivering nanoparticles to the sensing nanochannel, because the nanoparticles had a high tendency to stick to the bottom of the microchannels. Instead, we chose to use negatively charged nanoparticles and drove them to the sensing nanochannel electrophoretically. The four channel design proved useful in this respect because it helped us adjust the position of the gate electrode and enable convenient tuning of the MOSFET gate voltage.

A buffer solution containing 100 mM KCl, 10 mM Tris-EDTA with 1 mM EDTA (pH value of 8.0) was typically used as the electrolyte in our device. Platinum electrodes were used to apply the electrokinetic bias and to connect the fluidic circuit to the gate of the MOSFET. The reservoir labeled 1 was held at positive voltage, V_{ek}, the reservoir labeled 4 was held at ground, and reservoir 2 was used to connect the fluidic circuit to the gate of the MOSFET (2N7000 N-Channel FET, Fairchild Semiconductor Co.). The MOSFETs used in these experiments were identical to those used in the microfluidic sensor experiments, described in Chapter II, Sect. 2.2. The electrokinetic bias and MOSFET drain-source bias were applied using two separate DC power supplies (Agilent E3612A and Agilent E3617A). The MOSFET drain-source bias, V_{DS} was fixed at 0.15 V for all experiments.

The MOSFET drain current was measured by a current preamplifier (DL Instruments 1211), with rise time set at 1 ms. The current signal was then passed through a low-pass filter (Stanford Research Systems SR560) set at a cutoff frequency of 1 kHz, and then a Hum Bug noise eliminator, which removed most of the 50/60 Hz line cycle noise and associated harmonics, before it is fed into the digital data acquisition system. The power supplies used for applying the electrokinetic bias, drain-source bias, reservoir 4, and the current preamplifier were commonly grounded. Concurrent with the electrical measurements, the nanofluidic device was observed under an inverted fluorescence microscope (Zeiss Axiovert 135) using a 100x oil immersion objective.

3.3 Theoretical Analysis

Typically, in our experiments, a KCl-based buffer solution containing 100 mM KCl, 10 mM Tris-EDTA with 1 mM EDTA was filled into the microchannels and the liquid level in each reservoir was allowed to equilibrate. Then, a suspension containing nanobeads and this same buffer solution was added to reservoir 4. An electrokinetic bias (V_{ek}) was applied across reservoirs 1 and 4 to drive the nanobeads through the circuit electrophoretically through microchannels A and D and the sensing nanochannel. V_{ek} was adjusted such that the MOSFET was always working in the sub-threshold region ($V_G < V_T$) since the total amplification has been shown to be largest when the MOSFET is working in the sub-threshold region as discussed in Chapter II. As described in Chapter II, when a nanobead passes through the sensing nanochannel, the resistance of the sensing nanochannel increases and the corresponding drop in the ionic current results in a modulation of the gate voltage of the MOSFET. This gate voltage modulation results in a modulation of the MOSFET drain current. For our nanofluidic circuit, the ionic current flowing through the circuit when there are no nanobeads in the sensing nanochannel, I, is given by

$$I = \frac{V_{ek}}{R_A + R + R_D} \tag{3.1}$$

where R_A, R and R_D are the resistances of microchannel A, the sensing nanochannel and microchannel D respectively. Hence, the gate voltage that is fed into the MOSFET in this case (i.e. no nanobeads), V_G, is given by

$$V_G = V_{ek} - IR_A \tag{3.2}$$

When a nanobead passes through the sensing nanochannel, the ionic current flowing through the circuit is now given by

$$I^* = \frac{V_{ek}}{R_A + R + \Delta R + R_D} \tag{3.3}$$

where ΔR represents the increase in the resistance of the sensing nanochannel when a nanobead passes through it. Correspondingly, the gate voltage of the MOSFET can be written as

$$V_G^* = V_{ek} - I^* R_A \tag{3.4}$$

Since $I^* < I$, $V_G^* > V_G$. Thus, nanobead translocation across the sensing nanochannel results in an increase in the MOSFET gate voltage. So, we expect to see an upward spike in the MOSFET drain current signal when a nanobead passes through the sensing nanochannel. This is in contrast to the downward spikes seen in Chapter II when microbeads passed through the sensing channel of our microfluidic sensor, because of the arrangement of reservoirs 1, 2 and 4. If reservoir 3 was used instead of reservoir 2 to connect the fluidic circuit to the gate of the MOSFET, then downward spikes, just like those observed in Chapter II, would be observed. However, reservoir 2 was used for convenience of adjusting the gate voltage on the MOSFET.

The relative gate voltage modulation when a nanobead passes through the sensing nanochannel is given by

$$\frac{\Delta V_G}{V_G} = \frac{(I - I^*)R_A}{V_G} = \frac{V_{ek}}{V_G} \cdot \frac{R_A \Delta R}{(R_A + R + R_D)(R_A + R + \Delta R + R_D)} \tag{3.5}$$

Since, $\Delta R << (R_A + R + R_D)$, Eq. 3.5 can be simplified to give

$$\frac{\Delta V_G}{V_G} = \frac{V_{ek}}{V_G} \cdot \frac{R_A R}{(R_A + R + R_D)^2} \cdot \frac{\Delta R}{R} \tag{3.6}$$

In all our experiments, we used the MOSFET working in the sub-threshold region, so we can write the relative drain current modulation expected as

$$\frac{\Delta I_D}{I_D} = A_{FET,sub} \frac{V_{ek}}{V_G} \cdot \frac{R_A R}{(R_A + R + R_D)^2} \cdot \frac{\Delta R}{R} \tag{3.7}$$

where $A_{FET,sub}$ is given by

$$A_{FET,sub} = \left(\frac{qV_G}{kT} - \frac{V_G}{2\psi_S} \right) \left(\frac{d\psi_S}{dV_G} \right) \tag{3.8}$$

from Chapter II, Eq. 2.8. Since we use the same MOSFETs as in Chapter II, we will use fit parameters a=6.6 and V_{FB}=-0.3 reported in Chapter II, Sect. 2.4.3 and 2.4.4. We can now define the nanofluidic amplification factor, $A_{nanofluidic}$ as

$$A_{nanofluidic} = \frac{V_{ek}}{V_G} \cdot \frac{R_A R}{(R_A + R + R_D)^2} \tag{3.9}$$

3.4 Results

3.4.1 Detection of nanoparticles

A suspension of 210 nm-diameter fluorescent polystyrene (PS) nanobeads (Bangs Labs, Inc., FC02F/4779) in 100 mM KCl buffered with 10 mM Tris-EDTA was added to reservoir 4 of the nanofluidic sensor. An electrokinetic bias, $V_{ek} \sim 3.5$ V was applied across reservoirs 1 and 4. The MOSFET drain current observed as a function of time is shown in Fig. 3.7. From the baseline MOSFET drain current, the MOSFET

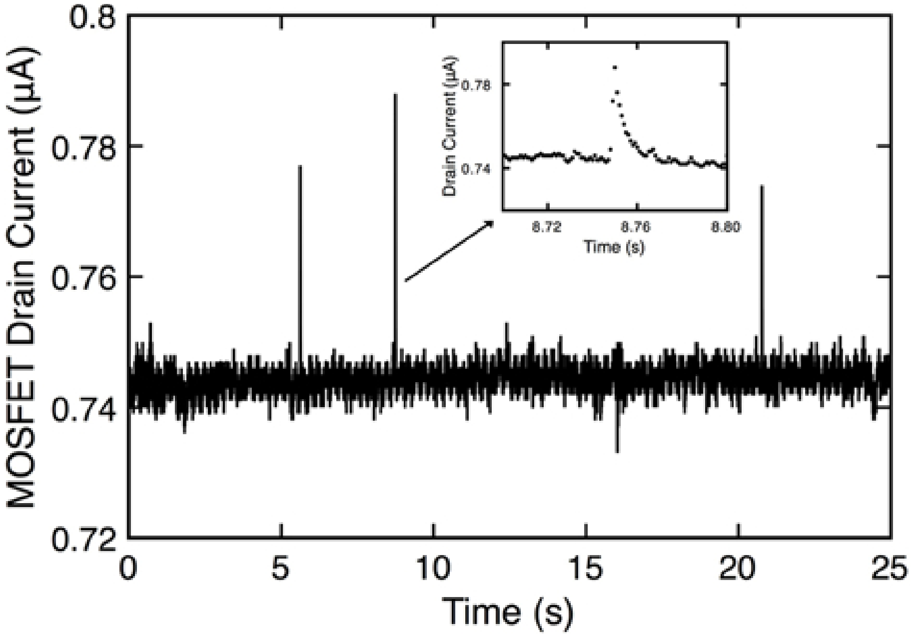

Figure 3.7: MOSFET drain current as a function of time for a suspension of 210 nm-diameter PS nanobeads. The MOSFET gate voltage is ~ 1.64 V so the MOSFET is working in the sub-threshold region. The inset shows a zoomed in view of a single bead translocation event.

gate voltage can be inferred to be ~ 1.64 V. Three 210 nm-diameter fluorescent PS nanobead translocation events are clearly observed in Fig. 3.7, and were verified by concurrent optical observation. It is worth noting here that no discernible dips were observed when the ionic current through the fluidic circuit was directly measured without the use of the MOSFET. Fig. 3.8 shows an image taken with the inverted fluorescence microscope used for concurrent optical observations.

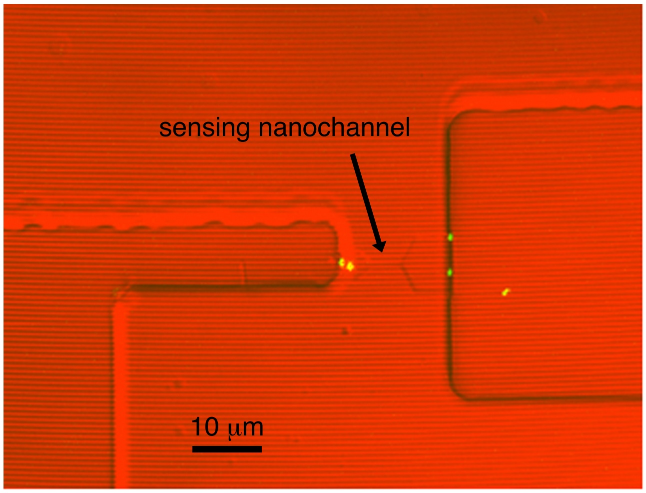

Figure 3.8: Overlay image of transmission image of sensing nanochannel region of nanofluidic sensor and fluorescence image of 210 nm-diameter fluorescent PS nanobeads taken with the inverted fluorescence microscope.

The relative drain current modulations for the three spikes shown in Fig. 3.7 are 4.6 %, 6.1 % and 4.2 % respectively. The variation in the relative drain current modulation observed may be attributed to the size distribution of the nanobeads. The ratio of the volume of the 210 nm-diameter PS nanobeads to the sensing nanochannel (length 5 μm and cross-section 0.35 μm $\times$ 0.5 μm) is $\sim$ 0.55 %. Thus, for the examples shown in Fig. 3.7, the total amplification factor observed by using our nanofluidic sensor is between 7.6 - 11.1. The theoretical total amplification factor based on Eqs. 3.7 and 3.8 is $\sim$ 9.2, in good agreement with our experimental results.

The total amplification factors observed during this preliminary experiments with the nanofluidic sensor (7.6 - 11.1) are much smaller compared to the total amplification factors observed for the microfluidic sensor reported in Chapter II (40 - 80). Ways to improve the total amplification factor for the nanofluidic sensor are outlined in Sect. 3.5.

The noise level in the measured drain current shown in Fig. 3.7 is ∼ 1.4 % of the baseline. Typically, the noise level in our experiments varied between 1 - 2 % of the baseline. This is relatively high because only the MOSFET part of the circuit was kept inside a Faraday cage due to the need for concurrent optical observations of the nanofluidic device. Fig. 3.9 shows an example of the typical noise level observed in the MOSFET drain current when both the MOSFET and nanofluidic device were kept in the Faraday cage without the use of the inverted fluorescence microscope. In this case, the noise level observed was ∼ 0.7 % of the baseline, smaller than typically observed when not using the Faraday cage and with concurrent optical observation (1 - 2 %), and within the range of noise levels observed in Chapter II for the microfluidic sensor

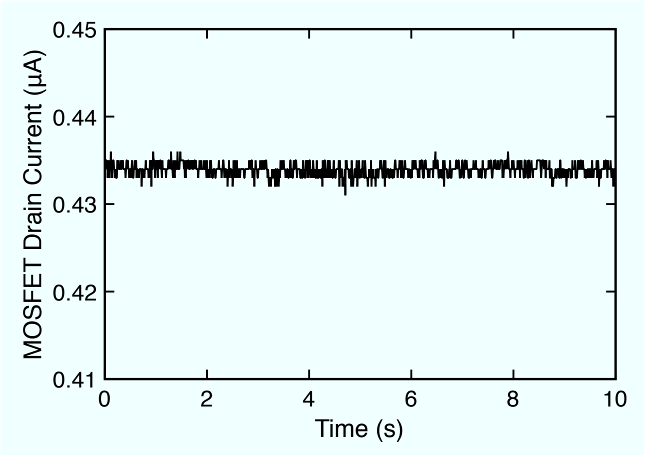

Figure 3.9: Typical noise level observed (∼ 0.7 % with respect to the baseline) when both the nanofluidic device and MOSFET were kept in a Faraday cage without the use of the inverted fluorescence microscope.

($\sim$ 0.5 - 0.9 %). Thus, preliminary investigations indicate that it might be possible to reduce the noise levels measured in the nanofluidic sensor to the same range as reported in Chapter II if both the MOSFET and the nanofluidic device were kept inside a Faraday cage. However, due to the difficulty in delivering the nanoparticles to the sensing nanochannel at the moment, we conducted all our experiments under the inverted fluorescent microscope to enable concurrent optical observations. Once we gain more experimental experience in nanoparticle delivery, we can shield both the MOSFET and nanofluidic device using a Faraday cage to minimize noise so that better device sensitivity can be obtained. We believe that it will be possible to achieve the same sensitivity (i.e. minimum detectable volume ratio of 0.006%) with the nanofluidic sensor in the future.

Assuming that we are able to achieve this level of sensitivity, we will be able to detect $\sim$ 46 nm-diameter nanobeads using a sensing nanochannel similar to that used in our experiments (length 5 μm, width 0.35 μm and height 0.5 μm). Thus, it will be possible to detect very small nanoparticles with relatively large sensing channels, which are easy to fabricate.

3.4.2 Size distribution of 210 nm-diameter fluorescent PS nanobeads

Next, we measured the distribution of the drain current modulations observed for the 210 nm-diameter fluorescent PS nanobeads using our nanofluidic device and compared it to the size distribution of the nanobeads as measured using dynamic light scattering instrument (Malvern Zetasizer Nano ZS), in order to check if the distribution of drain current modulations measured using our nanofluidic sensor can be attributed to the inherent size distribution of the nanobeads. A brief overview of the dynamic light scattering technique is given in Appendix B. To measure the distribution of the drain current modulations, a suspension of 210 nm-diameter fluorescent PS nanobeads in 100 mM KCl with 10 mM Tris, 1 mM EDTA buffer solution was added to reservoir 4 of the nanofluidic device. The electrokinetic bias, V_{ek}, was kept between 3 - 4 V such that the baseline MOSFET drain current remained approximately constant throughout the duration of the measurement.

The distribution of drain current modulations was measured over three different days with four similar nanofluidic devices because of the need for satisfactory statistics. With just a single nanofluidic device, we were not able to measure more than ~ 50 nanobead translocation events because of random blockages of the sensing nanochannel due to large nanobeads or groups of nanobeads. Fig. 3.10a shows the distribution of the MOSFET drain current modulation for 158 nanobeads measured. The filled histogram shows experimental data and the line shows a Gaussian fit to the data. From the Gaussian fit to the data, the mean drain current modulation was 6.1 % and the standard deviation was 1.5%.

Fig. 3.10b shows the size distribution of the 210 nm-diameter fluorescent PS nanobeads in 100 mM KCl with 10 mM Tris-EDTA buffer as measured using dynamic light scattering. The filled histogram shows experimental data and the line shows a Gaussian fit to the data. From the Gaussian fit to the data, the mean bead diameter was determined to be 200 nm and the standard deviation was 39 nm. In Chapter II, we directly measured the size distribution of the microbeads using a SEM. The main advantage of using dynamic light scattering over electron microscopy to directly

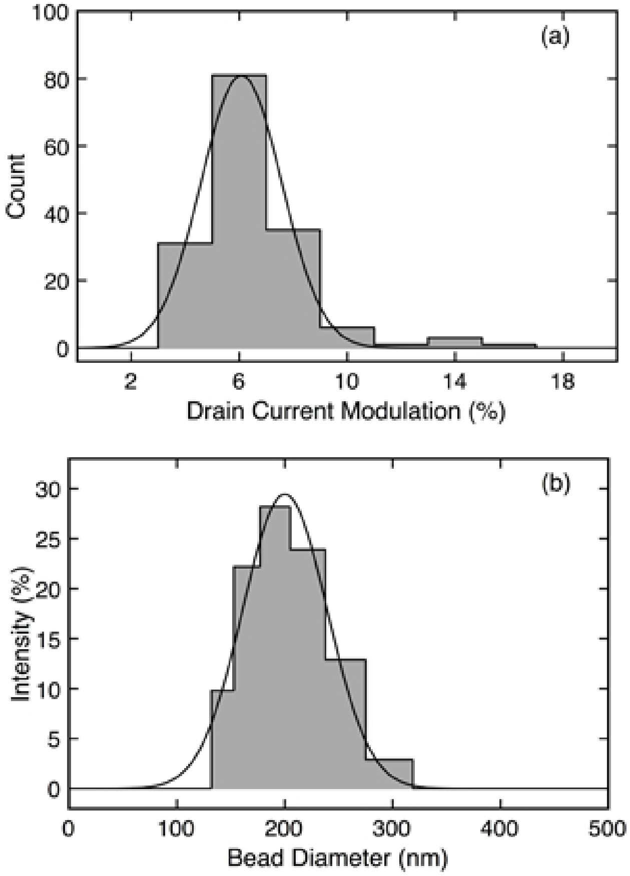

Figure 3.10: (a) Distribution of MOSFET drain current modulation measured for 210 nm-diameter fluorescent PS nanobeads using our nanofluidic devices. A total of 158 nanobead translocation events were measured. (b) Bead size distribution for 210 nm-diameter fluorescent PS nanobeads obtained from dynamic light scattering measurements. The filled histograms show experimental data and the line shows a Gaussian fit to the data.

characterize the size distribution of nanobeads is that light scattering measurements are based on an average of several hundred thousand nanobeads, whereas it is very difficult to image such a large number of nanobeads in a SEM. Thus, the statistical error in the nanobead size distribution obtained from light scattering measurements will be much lower than the corresponding measurements in a SEM. We were unable to use this more accurate instrument to characterize the size distribution of the 9.86 μm-diameter microbeads reported in Chapter II because those microbeads were too large to be detected using our light scattering instrument, which could only detect microbeads up to a maximum of ~ 6 μm in diameter. Thus, we have chosen to directly measure the nanobead size distribution using dynamic light scattering instead of SEM imaging.

To compare the two different distributions shown in Fig. 3.10 directly, the data were normalized by the mean of the respective Gaussian distributions: 200 nm for the Zetasizer data and 6.1 % for the data obtained from the nanofluidic sensor. Fig. 3.11a shows the normalized data from the nanofluidic device and Fig. 3.11b shows the normalized data from the Zetasizer measurements. By definition, the normalized mean of both distributions was 1.0. From Fig. 3.11a, the standard deviation of the normalized drain current modulation obtained from the nanofluidic device data was 0.25. In comparison, from Fig. 3.11b, the standard deviation of the normalized bead diameter obtained from the Zetasizer measurements was 0.20.

Since the drain current modulations from the nanofluidic sensor are proportional to nanobead volume in contrast to light scattering which is proportional to nanobead diameter, we expect the standard deviation from the nanofluidic sensor measurements

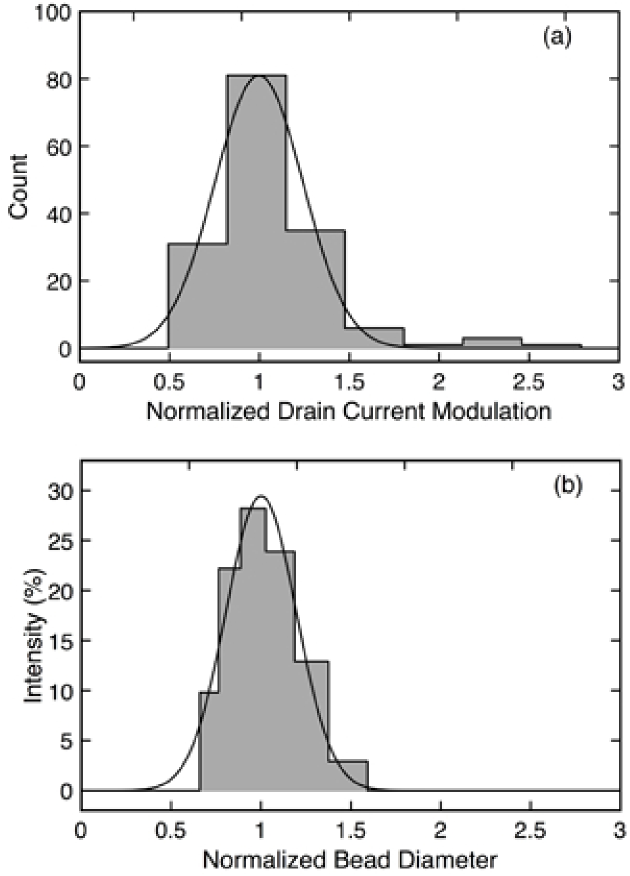

Figure 3.11: (a) Normalized distribution of drain current modulation for 210 nm-diameter fluorescent PS nanobeads obtained from nanofluidic sensor measurements. The normalized mean was 1.0 and the standard deviation was 0.25. (b) Normalized size distribution for 210 nm-diameter fluorescent PS nanobeads obtained from light scattering measurements. The normalized mean was 1.0 and the standard deviation was 0.20.

to be three times the standard deviation from the light scattering measurements. However, the observed standard deviation from the sensor is only slightly higher than that from the light scattering measurement. One possible reason could be that since we have used four different devices to measure the size distribution of the nanobeads as mentioned above, the volume of the sensing nanochannel could vary slightly from one device to another. This would affect the drain current modulations observed and skew the resultant size distribution observed. A full analysis of this difference would depend on understanding the intrinsic resolution of both techniques and how it affects the actual size distribution data.

3.5 Discussion

During the course of our experiments, we experienced difficulty in delivering the nanobeads reliably to the sensing nanochannel. In general, when we used plain fluorescent polystyrene nanobeads without any surface groups, we found that the nanobeads often got stuck to the microchannel walls of our device. Consequently, the probability of delivering the nanobeads successfully to the sensing nanochannel was very low. As a result of all our attempts, successful or otherwise, we have learned that there are two considerations that must be taken into account when designing a nanofluidic sensor. We have to be able to (a) reliably deliver the nanoparticles to the sensing nanochannel, and (b) sense the nanoparticle translocation with maximum total amplification. These two issues will be addressed in this order, based upon the insights we have gleaned from our experimental efforts.

The two main factors that determine whether or not we are able to deliver nanoparticles successfully are the surface charge of the nanoparticles and the concentration of electrolyte in which the nanoparticles are suspended. In general, when nanoparticles are suspended in an electrolyte and driven by an applied electric field, there are two forces acting on the nanoparticle - the electro-osmotic force that drives the nanobeads along with the bulk fluid from the positive to negative terminal, and the electrophoretic force due to the surface charge of the nanobeads themselves, which is normally negative, that drives them from the negative to the positive terminal. The electro-osmotic force is inversely proportional to the concentration of the electrolyte, and the electrophoretic force is directly proportional to the surface charge of the nanoparticle. Under certain conditions, the two opposing forces may cancel each other resulting in negligible flow of the nanoparticles inside the device. Thus, based on the surface charge of the nanoparticle that needs to be sensed, the concentration of electrolyte used must be optimized to enable successful and reliable delivery of the nanoparticles to the sensing nanochannel. For nanoparticles with low negative surface charge, the electrolyte concentration must to be low such that the electro-osmotic force dominates over the electrophoretic force, and for nanoparticles with high negative surface charge, the electrolyte concentration must be high such that the electrophoretic force dominates over the electro-osmotic force. In our experiments reported in Sects. 3.4.1 and 3.4.2, we have chosen a rather high concentration of electrolyte (100 mM KCl buffered with 10 mM Tris and 1 mM EDTA) because the nanobeads we used have high negative surface charge due to the presence of carboxylic acid groups (-COOH) on the surface of the nanobeads. It must be noted that due to their high negative surface charge, carboxyl-terminated nanobeads (Saleh &

Sohn, 2001; 2003; Sun & Crooks, 2000; Ito et al., 2003) have been successfully used by other researchers working with traditional resistive-pulse sensors. Alternatively, some research groups chose to focus on DNA molecules (Saleh & Sohn 2003; Chang et al. 2004; Heng et al, 2004; Chen et al., 2004a; 2004b; Fan et al., 2005; Fologea et al., 2005; Storm et al., 2005; Tabard-Cossa et al., 2007) which also have high negative surface charge. However, although the usage of highly charged nanoparticles in nanoscale sensors is common, a comprehensive investigation of the effect of electrolyte concentration and nanoparticle surface charge on the transport of nanoparticles has not yet been done.

To maximize the amplification factor for sensing nanoparticles, we have to maximize the right-hand side of Eq. 3.7. The MOSFET amplification factor is maximum when the MOSFET is working in the sub-threshold region, and we have already implemented this in our experiments reported earlier. The nanofluidic amplification factor, $A_{nanofluidic}$, can be maximized by better designing our nanofluidic device. From Eq. 3.9, there are two independenet parameters that we can adjust to improve the nanolfuidic amplification factor - the ratio of V_{ek}/V_G and the resistance ratio $R_A R/(R_A + R + R_D)^2$. The ratio V_{ek}/V_G can be improved by increasing the electrokinetic bias, V_{ek} used to drive the nanoparticles through the device. However, increasing V_{ek} will result in the nanoparticles flowing faster, and care must be taken to ensure that the nanoparticles do not move so quickly through the sensing nanochannel that the data acquisition rate becomes insufficient. Assuming that the resistance of the sensing nanochannel is determined by the size of the nanoparticle being sensed and hence constant for the purpose of this analysis, the resistance ratio

$R_A R/(R_A + R + R_D)^2$ can be maximized by designing the nanofluidic device such that

$$R_A = R + R_D \tag{3.10}$$

Thus, through our nanofluidic experimental efforts, we have gained some valuable insight into how we can better design a nanofluidic sensor. First, based on our choice of nanoparticles, the concentration of the electrolyte must be optimized such that the nanoparticles are successfully delivered to the sensing nanochannel. Next, the nanofluidic amplification factor, $A_{nanofluidic}$ must be maximized. The electrokinetic bias applied to drive the nanoparticles through the device must be maximized, while ensuring that the speed at which the nanoparticles pass through the sensing nanochannel is less than the data acquisition rate. In addition, the microchannels A and D in the nanofluidic device can be designed such that their resistances obey Eq. 3.10 to maximize the nanofluidic amplification factor. Finally, as mentioned in Sect. 3.4.1, the nanofluidic device was not shielded in a Faraday cage due to the need for concurrent optical observations. We believe that better device sensitivity and performance can be achieved if we shield both the nanofluidic device and the MOSFET in a Faraday cage. This will lower our noise levels with respect to the baseline and enable us to sense smaller relative drain current modulations.

3.6 Summary

We have developed a prototype nanofluidic sensor based on the new MOSFET-based sensing scheme. We have shown that we can successfully detect 210 nm-diameter nanobeads using a sensing nanochannel that was 350 nm wide, 500 nm deep and 5 μm long. With further experimental optimization, we believe that we can sense nanobeads as small as 46 nm in diameter using such a sensing nanochannel. Hence, our new sensing scheme will reduce the stress on fabrication technology to make sensing nanochannels of the same size as the nanoparticles being detected, as currently required for traditional resistive-pulse sensors. As a result of our experiments, we have gained new insights into how a better nanofluidic sensor based on our new sensing scheme can be designed. As such, we have outlined four major guidelines that will enable us to further improve the performance of the nanofluidic sensor in future works.

CHAPTER IV

MOLECULAR DYNAMICS SIMULATIONS OF THERMAL BUBBLE FORMATION IN NANOCHANNELS

4.1 Motivation

In a recent report on nanopore-based resistive pulse sensors, Smeets et al. (2006) have used a simple model to show that the conductance expected with a nanobubble present inside a nanopore is similar to the conductance measured experimentally. They suggest that nanobubbles could cause a strong increase in low-frequency current noise observed in ionic current measurements through nanofluidic devices due to nucleation, movement along the nanopore surface and/or dissolution. However, we ask the question whether bubbles can form inside nanoscale channels, and hence be a plausible source of electrical noise in nanofluidic experiments? Nanoscale bubbles of interest are difficult to observe experimentally. Our MOSFET-based nanofluidic sensor might eventually prove to be a technique sensitive enough to detect the presence of bubbles inside nanochannels. Until that time, we can investigate bubble nucleation in nanochannels using molecular dynamics (MD) simulations. The rapid growth of computer power has allowed and stimulated a significant amount of research using molecular dynamics to study the bubble nucleation process, with model systems composed of simple Lennard-Jones liquids like argon. Thus, we adapted these approaches and pursued the theoretical investigation of bubble nucleation in nanochannels using the MD method.

In this Chapter, we will first present a brief introduction to the MD method. Then, we will review the MD simulations of bubble nucleation in nanochannels that have already been reported by several other groups. We will then present our MD simulation model and verify that our MD models are working properly by reproducing previously published results. Next we will present our MD simulation results for two different fluids - argon and water. Finally, we discuss our simulation results and offer a possible explanation for the results observed. Most of the work presented in this Chapter has been submitted for publication in Microfluidics Nanofluidics (Sridhar et al., 2008a).

4.2 Introduction to Molecular Dynamics

Molecular dynamics simulation is a technique for computing the equilibrium and transport properties of a classical many-body system (Frenkel & Smit, 2002). We typically select a model system of N atoms or molecules, solve Newton's equations of motion for this system until the system reaches satisfactory equilibrium (i.e. critical properties of system do not change significantly with time), and finally extract out the necessary measurements usually with the aid of the methods of statistical mechanics. A simple molecular dynamics program typically involves four steps (Allen & Tildesley, 1987):

1) Initialize the positions and velocities of all N atoms involved in the simulation.

2) Calculate the force on each atom in the system based on the intermolecular

potentials chosen.

3) Update the position and velocity of each atom in the system after a short time interval δt.

4) Calculate measured variables in the system, and repeat from 2) until system reaches satisfactory equilibrium.

The three most important computational steps are steps 1-3 shown listed above. We will now consider these three steps individually.

4.2.1 Intermolecular potentials

In order to accurately calculate the force on each atom in the system, it is crucial to have an accurate description of the interaction potential between every atom in the system. For a simple system containing N atoms, we can approximate the potential energy of the system, U, as

$$U(r_1, r_2, ...r_N) \approx \sum_i u_1(r_i) + \sum_i \sum_{j>i} u_2(r_i, r_j) \tag{4.1}$$

where the index i runs from 1 to N (i.e. the summation is over all N atoms in the system), $u_1(r_i)$ is the potential due to an external force field, and $u_2(r_i, r_j)$ represents the pairwise interaction of the N atoms in the system, which is normally the most important interaction and is often referred to as the pair potential. In this approximation, we have neglected higher order terms that correspond to interactions between three or more atoms. This is a common approximation in molecular dynamics simulations because it becomes very complicated and computationally expensive to calculate many-body interactions. As such, many-body interactions are often accounted for by the use of an ‘effective’ pair potential.

In general, we can categorize pairwise interactions into two kinds - short-range interactions and long-range interactions.

Short-range Interactions

Short-range interactions refer to interactions where the interaction potential decays rapidly with interatomic distance. The most commonly used short-range interaction potential is called the 6-12 Lennard-Jones (L-J) potential. The general form of the L-J potential can be written as

$$u_{LJ}(r_i, r_j) = 4\epsilon_{ij}\left[\left(\frac{\sigma_{ij}}{r_{ij}}\right)^{12} - \left(\frac{\sigma_{ij}}{r_{ij}}\right)^{6}\right] \tag{4.2}$$

where ϵ_{ij} represents the depth of the potential well between atoms i and j, σ_{ij} is a length parameter that represents the finite distance at which $u_{LJ} = 0$, and r_{ij} is the distance between atoms i and j. Fig. 4.1 shows a plot of the pair potential, u_{LJ}, as a function of interatomic distance, r_{ij}, for the case of liquid argon. The parameters ϵ and σ are taken to be 1.67×10^{-21} J and 3.405 Å respectively (Verlet, 1967).

As can be seen from Fig. 4.1, the L-J potential is highly repulsive at short distances, approximately less than 3.5 Å, weakly attractive at longer distances, and decays close to zero when the interatomic distance is greater than ~ 6 Å. The repulsive component is due to the r^{-12} term in the L-J potential, which represents the

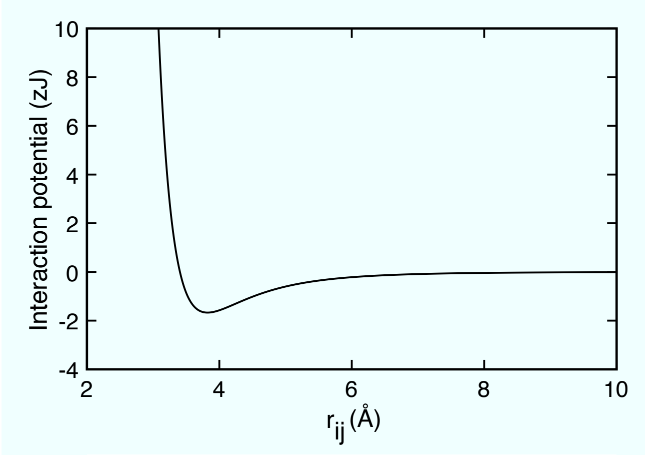

Figure 4.1: Plot of the interaction potential, u_{LJ}, as a function of interatomic distance, r_{ij} for the case of liquid argon. The depth of the potential well, ϵ, is 1.67 zJ and σ is 3.405 Å.

steric hindrance of an atom, and the attractive part is due to the r^{-6} term, which represents the effect of induced dipole interactions due to fluctuations in the charge distribution of the atoms. The values for the parameters ϵ and σ are often available for interactions of like elements, and combining rules such as the Lorentz-Berthelot mixing rule (Allen & Tildesley, 1987) shown in Eq. 4.3 can be used to generate appropriate parameters for interactions involving unlike elements or molecules. The subscripts 1 and 2 in Eq. 4.3 represent atoms of two different elements.

$$\begin{aligned} \sigma_{12} &= \tfrac{1}{2}(\sigma_{11} + \sigma_{22}) \\ \epsilon_{12} &= \sqrt{(\epsilon_{11}\epsilon_{22})} \end{aligned} \tag{4.3}$$

For a system of N particles, the time needed to calculate the total potential energy or force for pairwise-additive interactions such as the L-J interaction will be proportional to N^2. Thus, the computations become very time-consuming and computationally expensive when simulating systems with a large number of particles. When the interatomic distance, $r_{ij} = 2.5\sigma$, the L-J potential drops to just 1.6% of the well depth. Hence, it is common to restrict the evaluation of the potential to atoms within a sphere of radius r_c, where $r_c \sim 2.5\sigma$, since interactions between atoms that are further than this limit do not significantly affect the total potential energy of the system. This approach significantly reduces the computation time, because the number of interactions computed explicitly is now reduced.

However, this approach still requires us to compute the interatomic separations of every distinct pair of atoms in the system at each time step so that we can evaluate whether the atoms are within the cutoff sphere or not. Verlet (1967) introduced a technique known as the Verlet list or neighbor list, in which a second cutoff radius, r_v, is introduced where $r_v > r_c$. Before calculating the interactions, a list of all particles within a radius, r_v, of a particular particle i is made. Then, only those particles in this neighbor list are tested at each timestep to see if the interatomic separation $r_{ij} < r_c$. Using this technique, the time taken to compute the total potential energy of a N-body system will vary as N^{α}, where $1 \leq \alpha \leq 2$, depending on how frequently the neighbor list is updated and the choice of r_v. The neighbor list must also be reconstructed frequently (of order 10 timesteps) to ensure that atoms not present in the neightbor list for a particular particle do not come into the interaction region during the course of the simulation.

Long-range Interactions

Long-range interactions refer to interactions where the interaction potential decreases gradually with interatomic distance. A common long-range interaction potential is the Coulomb potential which varies as $1/r_{ij}$. For a system containing ions or polar molecules such as water, the Coulomb potential can be written as

$$u_{coul} = \frac{1}{2} \sum_{i} \sum_{j, j \neq i} \frac{q_i q_j}{|\mathbf{r}_{ij}|} \tag{4.4}$$

where q_i and q_j are the charges on atoms i and j respectively. There are two main difficulties with calculating long-range interaction potentials:

(a) The calculation must be done over all possible atom pairs in the simulation system since the potential does not decay rapidly like the L-J potential.

(b) Since we often use periodic boundary conditions, i.e. the simulation box is replicated throughout space to form an infinite lattice, interactions between particles in the main simulation box and all periodic images of the atoms must be evaluated.

Formally, the Coulomb potential for a N-body system can be evaluated using a lattice sum as shown in Eq. 4.5.

$$u_{coul} = \frac{1}{2} \sum_{i,j=1}^{N} \sum_{\mathbf{n}}{}' \frac{q_i q_j}{|\mathbf{r}_{ij} - \mathbf{n}L|} \tag{4.5}$$

where $\mathbf{n}$ is a lattice vector and $\sum\nolimits'_{\mathbf{n}}$ means that for $\mathbf{n} = 0$, $i \neq j$. This lattice is sum is only conditionally convergent, and Ewald (1921) invented a method called the Ewald summation method which overcomes this limitation. It is worth noting that there are other techniques to evaluate long-range interactions such as fast multipole methods and particle-mesh techniques (Frenkel & Smit, 2002), but the Ewald summation method is the most widely used method and is the method used in this work.

The basic idea of the Ewald sum involves introducing a Gaussian screening charge density of opposite charge for each point charge in the system such that the electrostatic potential due to each point charge decays to zero within a short distance. This part of the potential then becomes short-ranged and is evaluated easily in real space. The effect of this artificially introduced Gaussian screening charge density is then handled by a sum in reciprocal space. The detailed derivation of the Ewald sum can be found elsewhere (de Leeuw et al. 1980a; 1980b) and the final form can be written as

$$
\begin{aligned}
u_{coul} = \frac{1}{2}\Bigg[\sum_{\mathbf{n}}{}' \sum_{i,j=1}^{N} \frac{q_i q_j erfc(\alpha|\mathbf{r}_{ij} - \mathbf{n}L|)}{|\mathbf{r}_{ij} - \mathbf{n}L|} - \frac{2\alpha}{\sqrt{\pi}} \sum_{i=1}^{N} q_i^2 \\
+ \frac{4\pi}{L^3} \sum_{\mathbf{k}\neq 0} \sum_{i,j=1}^{N} \frac{q_i q_j}{|\mathbf{k}|^2} e^{-k^2/4\alpha^2} e^{i\mathbf{k}\cdot\mathbf{r}_{ij}} \Bigg]
\end{aligned}
\tag{4.6}
$$

where $\mathbf{k} = 2\pi\mathbf{n}/L$.

The first summation term is the real space evaluation of the potential of a set of point charges which are screened by a Gaussian distribution of opposite charge, centered at r_i with width α, such that the real space potential decays rapidly to zero at a short distance. The potential due to this artificially introduced screening charge is then accounted for by a sum in reciprocal space, as shown in the third term in Eq. 4.6. The second term represents the correction for including the self-interaction of the Gaussian screening charge cloud and a point charge q_i located at the center of the Gaussian cloud. Typically, a cutoff sphere of radius R_c is used to simplify the evaluation of the real space sum of the Ewald sum, and a cut-off wave-vector, $\mathbf{k}_{max}$, is used to truncate the reciprocal space sum. Thus, typically the three parameters, α, R_c and $\mathbf{k}_{max}$ are chosen such that the truncation error in each term is minimized and the speed of the computation is maximized.

4.2.2 Integration algorithm

Once the initial configurations of the atoms in the MD system are specified and the potentials are evaluated to calculate the force on each atom, the equations of motion, shown in Eq. 4.7 and 4.8, can be integrated using finite-difference methods.

$$\mathbf{f}_i = -\frac{\partial U}{\partial \mathbf{r}_i} \tag{4.7}$$

$$m_i \ddot{\mathbf{r}}_i = \mathbf{f}_i \tag{4.8}$$

where U is the potential energy function, $\mathbf{f}_i$ is the force on atom i due to all other atoms in the system, and m_i and r_i are the mass and co-ordinates of atom i.

The algorithm used to integrate the equations of motion is usually referred to as the integrator. The accuracy of the integrator increases as the time interval between successful calculations is reduced, i.e. $\delta t \to 0$. However, this increases the number of computations of potential, position etc. required and hence reduces computational speed. Hence, there is an intrinsic trade-off between accuracy and speed and the integration time step is chosen carefully to balance these two considerations.

The most commonly used integration algorithm is the Verlet algorithm (Verlet, 1967) and in this work we use a variation of this algorithm known as the leap-frog scheme (Allen & Tildesley, 1987). The algorithm can be written as

$$\mathbf{r}(t+\delta t) = \mathbf{r}(t) + \delta t\ \mathbf{v}(t+\delta t/2) \tag{4.9}$$

$$\mathbf{v}(r+\delta t/2) = \mathbf{v}(t-\delta t/2) + \delta t\ \mathbf{a}(t) \tag{4.10}$$

where $\mathbf{r}$, $\mathbf{v}$ and $\mathbf{a}$ are vectors of position, velocity and acceleration respectively and δt is the time step of the integration algorithm. In the leap-frog scheme, the current positions $\mathbf{r}(t)$, accelerations $\mathbf{a}(t)$ and mid-step velocities $\mathbf{v}(t-\delta t/2)$ are stored. The velocity equation, Eq. 4.10, is solved first to give $\mathbf{v}(t+\delta t/2)$, and then the new positions can be calculated using this updated velocity. The current velocity can be calculated by

$$\mathbf{v}(t) = \frac{1}{2}\left[\mathbf{v}(t+\delta t/2) + \mathbf{v}(t-\delta t/2)\right] \tag{4.11}$$

4.2.3 Statistical Ensemble

The most common ensembles used in MD simulations are the microcanonical (NVE) ensemble, where the number of atoms in the system, the volume of the system and the total energy of the system are held constant, and the canonical (NVT) ensemble, where the number of atoms in the system, volume of the system and temperature of the system are held constant. However, it is possible to also simulate other ensembles such as the isobaric-isothermal (NPT) ensemble by controlling the appropriate thermodynamic quantities in MD simulations. There are four different types of control mechanisms used in the literature to control the relevant thermodynamic quantities: (a) differential control, (b) proportional control, (c) integral control and (d) stochastic control. In this work, we use the NVT ensemble and the NPT ensemble, and a proportional control algorithm is used to control the system temperature. The proportional thermostat was proposed by Berendsen et al. (1984), and weakly couples the system to an external heat bath. At each time step, the deviation of the system temperature, T, from the prescribed temperature, T_0, is corrected by multiplying the velocities of the atoms by a factor, λ_T, which is given by

$$\lambda_T = \left[1 + \frac{\delta t}{\tau}\left(\frac{T_0}{T} - 1\right)\right]^{1/2} \tag{4.12}$$

where τ is the coupling time constant and represents the time scale in which the system reaches the desired temperature, T_0, and δt represents the time step of the MD simulation. It is worth noting that the Berendsen thermostat allows the system temperature, T, to fluctuate around the desired temperature, T_0, and corrects it to a value closer to T_0 at every time step.

4.3 A Brief History of MD Simulations of Bubble Nucleation

Thermal bubble nucleation in nano-confined spaces has attracted considerable attention recently (Kinjo et al., 1999; 2000; Maruyama & Kimura, 2000; Park et al., 2000; Wu & Pan, 2003; Nagayama et al., 2006), partly due to fundamental interest in novel phase change phenomena in nano-confined systems and partly due to the potential applications of bubbles as valves and pumps in micro- and nanofluidic devices. Lugli and Zerbetto (2007) discussed a number of other interesting applications of bubbles, such as using collapsing bubbles as micro-reactors to enhance chemical reactions and as vectors to direct drug delivery. In addition, as mentioned in Sect. 4.1, bubbles in nanopores have been suggested as a major source for the noise in the measured ionic current through nanopores in nanoscale resistive-pulse sensors (Smeets et al., 2006). Such nanoscale bubbles of interest are difficult to observe experimentally.

Due to the rapid growth of computer power, there has been a significant amount of research done using molecular dynamics to study the bubble nucleation process, with model systems composed of simple Lennard-Jones liquids like argon. In most simulations, either an NVE system (a system with constant number of molecules, constant volume, and constant energy) or an NVT system (a system with constant number of molecules, constant volume, and constant temperature) is implemented. Due to the constant volume assumption, generation of a bubble will squeeze the rest of the liquid, leading to an ultrahigh pressure in the liquid because of the low compressibility of liquid. Therefore, no stable bubble can be generated in the simulation system of constant volume with saturation liquid density by simply setting the temperature to be higher than the saturation temperature under a certain pressure. To overcome this difficulty, various techniques have been used to create a model system with a density lower than the density of saturated liquid under certain temperature, and stable bubbles were observed in the simulations. However, such simulations can be regarded more appropriately as bubble cavitation rather than thermal bubble nucleation.

A brief summary of recent work follows. Kinjo et al. (1998; 1999) used a microcanonical (NVE) ensemble to study bubble formation in Lennard-Jones liquids and showed that bubbles formed instantaneously when the average density of the liquid was less than 83% of the saturated liquid density at atmospheric pressure. They predicted rapid growth of bubbles up to a diameter of ~ 2 nm when the density was lower than this limit.

Park et al. (2000) and Wu and Pan (2003) studied bubble formation using NVT ensembles in Lennard-Jones liquids. Park et al. (2000) reported that stable bubbles were formed at $T = 99$ K when the average density of the liquid was less than 80% of the saturated liquid density at atmospheric pressure in a cubic box 5.1 nm long in each dimension. They also showed that this critical average density scaled proportionally with the size of the simulation box. Larger simulation boxes had a higher critical average density because the liquid was in a bigger domain and more liable to break up and induce a bubble than when the liquid was in a smaller box. They also reported that the minimum stable bubble diameter observed was 2 nm. They claimed that no bubble was observed in a cubic simulation box of an edge length less than 3.7 nm. Wu and Pan (2003) calculated the critical average liquid density for various negative pressures in a cubic box with an edge length of 5.75 nm and found that the value was consistently less than 78% of the bulk saturated liquid density. They also calculated the homogeneous nucleation rate of argon to be on the order of 10^{29} cm^{-3}s^{-1} for various negative pressures, and showed that the generated bubbles did not grow more than 3 - 3.5 nm in diameter. This asymptotic value for bubble diameter was attributed to the fact that these bubbles occupy 50 - 70% of the simulation box volume, which was close to the maximum packing of bubbles (74%) without coalescence, considering bubbles as rigid particles. In all simulations, periodic boundary conditions in all three dimensions were adopted with negative pressures of -10 to -20 MPa, and critical average liquid densities of about 80% of the bulk saturated liquid density were reported.

Maruyama & Kimura (2000), and Nagayama et al. (2006) studied bubble formation in Lennard-Jones liquids in the presence of solid platinum walls. Maruyama & Kimura (2000) expanded the volume of their simulation system adiabatically and instantaneously to generate negative pressures on the order of -20 MPa to induce bubble generation in an NVE simulation domain and reported the formation of stable bubbles of 4 - 6 nm in diameter. They also reported that the equilibrium shape of the bubble was characterized by the wettability of the solid surface, where low wettability resulted in bubbles of flattened shape and high wettability resulted in bubbles of more spherical shape. Nagayama et al. (2006) used a combination of NVT ensemble and non-equilibrium molecular dynamics method where an external force is applied to each molecule at the inlet of the nanochannel. They investigated the bubble formation process in terms of the hydrophobicity/hydrophilicity of the solid walls. Their results indicated that bubbles were formed in the bulk of the liquid when the walls were hydrophilic and close to the surface of the walls when the walls were hydrophobic. They observed stable bubbles of 2 - 4 nm in diameter and suggested that the Young-Laplace equation may be inadequate for nano-bubbles because there were not enough vapor molecules in the bubbles to generate a sufficiently high vapor pressure to maintain force balance with the surrounding liquid.

The generation of bubbles due to rupturing of fluid caused by a decrease in pressure is referred to as cavitation (Brennen, 1995). It can be seen that all the aforementioned reports on modeling bubble generation represent simulations more of a cavitation process rather than thermal bubble formation because of the use of negative external pressures which are likely to exert enough tensile stress to rupture the fluid. In reality, thermal bubble generation usually happens under constant temperature and pressure while the system volume can vary. NPT simulations of bubble nucleation are rarely reported in the literature. In fact, to our knowledge the only NPT study of bubble nucleation was recently reported by Novak et al. (2007). They primarily investigated the effect of the strength of solid-liquid interactions on bubble nucleation rate. They simulated several cases corresponding to strong, neutral and weak solid-liquid interactions and found that the nucleation rate was highest when the solid-liquid interaction was weak.

In this work, we report on simulations of thermal bubble nucleation in NPT systems of both argon and water using a parallel molecular dynamics code, with a different mathematical formalism as compared to Novak et al. (we will discuss the different computational approaches used by Novak et al. and this work, which give rise to our different results, in the following section). Our results indicated that for the NPT system, no bubble generation was observed at an external pressure of 0.1 MPa even though the system temperature was well above the boiling temperature of the respective liquids. In fact, no bubble generation could be observed even when the external pressure was reduced to as low as 0.01 MPa. To explain our observations, we hypothesize that bubble nucleation in nano-confined liquids is suppressed by a pressure wave generated inside the nanochannel during bubble nucleation. This pressure wave travels toward the channel walls, reflects off the solid walls back toward the bubble nucleation site and suppresses bubble nucleation.

4.4 MD Simulation Methods

We simulated both NVT and NPT systems for two kinds of liquids: argon and water with molecular dynamics.

4.4.1 NVT Systems

The interaction between argon atoms was modeled using the L-J potential as described by Eq. 4.13:

$$u_{LJ}(r_{ij}) = 4\epsilon\left[\left(\frac{\sigma}{r_{ij}}\right)^{12} - \left(\frac{\sigma}{r_{ij}}\right)^{6}\right] \tag{4.13}$$

where the length parameter, σ_{Ar-Ar}, the energy parameter, ϵ_{Ar-Ar}, are listed in Table 4.1.

The water molecules were modeled by the SPC/E model (Berendsen et al., 1987) with a SETTLE algorithm (Miyamoto & Kollman, 1992) to maintain the rigid geometry of each molecule. The intermolecular interactions are described by the Lennard-Jones potential with parameters for different atom pairs given in Table 4.1 (Qiao & Aluru, 2003). In addition, the electrostatic interactions between the O and H atoms

Table 4.1: Lennard-Jones parameters used for interactions involving argon, silicon and water molecules (Qiao & Aluru, 2003).

Atom pair	ϵ (10^{-21} J)	σ (Å)
Ar-Ar	1.67	3.41
Ar-Si	5.2	3.36
O-O	4.3	3.17
O-Si	8.4	3.27

in water molecules were calculated using an Ewald summation algorithm (Frenkel & Smit, 2002). Periodic boundary conditions were adopted in all three dimensions for both the water and argon systems. A Berendsen thermostat (Berendsen et al., 1984) with a time constant of 0.1 ps was used to control the system temperature at a given value. The equations of motion were integrated using a leap-frog algorithm with a time step of 2.0 fs. In all simulations, a cutoff radius of 11 Å was used to calculate the L-J potential and the real space part of electrostatic interaction potential.

4.4.2 NPT Systems

For NPT systems, the argon or water molecules, modeled using the same intermolecular potentials as in the NVT systems, are sandwiched between two parallel silicon plates. For the argon NPT systems, the Ar-Si interaction was also modeled using the L-J potential with the parameters calculated using the Lorentz-Berthelot combination rule shown in Eq. 4.3. The L-J parameters used for the Ar-Si are shown in Table 4.1. It is worth noting that the primary difference between our simulation scheme and that of Novak et al. (2007) is the way we have handled the solid-liquid interactions. Novak et al. used a L-J potential, similar in form to what we have used, to model the solid-liquid interaction at the bottom channel wall. However, they used a 9-3 mean field potential to model the interactions of the fluid atoms with the top channel wall. The 9-3 potential results from a series of approximations in which the original L-J potential is averaged over space, to form a continuum description. The L-J potential that forms the basis of the 9-3 potential, is precisely of the same form as that used in this paper in a non-averaged approach. In particular, we have used the same L-J potential to model fluid interactions with both the top and bottom channel walls, as opposed to the approach used by Novak et al.

For the water NPT systems, the interaction between water molecules and silicon walls was described by the L-J interaction between oxygen and silicon atoms with interaction parameters also listed in Table 4.1. The electrostatic interactions between the O and H atoms in the water molecules were calculated using an Ewald summation algorithm with slab correction (Yeh & Berkowitz, 1999). Periodic boundary conditions were applied in the two dimensions that were not bound by the silicon walls. The top silicon wall was allowed to move in the z-direction, up to a maximum of 10 - 15 nm from the bottom wall, to maintain constant pressure enforced upon the simulation systems. A Berendsen thermostat, as described for the NVT systems, was used to control system temperature, and the leap-frog algorithm was used to integrate the equations of motion with a time step of 2.0 fs. The same cutoff radius as used in NVT systems was used to calculate the L-J potential and real space part of the electrostatic interaction potential.

4.5 Verification of Code and Results of NVT Systems

To verify that our code produces results similar to those reported in the literature, we first modeled argon NVT systems, which have been reported in several publications. We also modeled water NVT systems, which have not been reported in the literature to our knowledge. The NVT simulations of both argon and water systems allow the comparison with their respective NPT systems.

4.5.1 Verification of MD Code using Argon NVT Case

The canonical (NVT) ensemble of argon included 2606 argon atoms in a simulation box as shown in Fig. 4.2. The system temperature was kept at 100 K and the

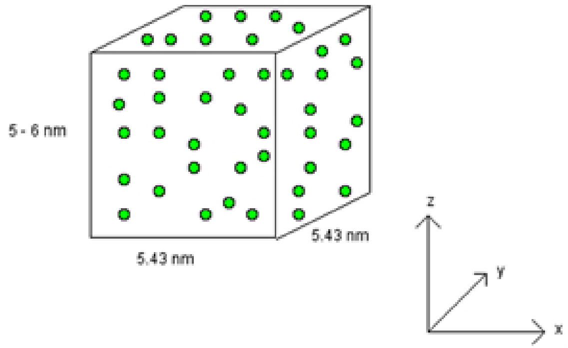

Figure 4.2: Schematic of the simulation box (not to scale) used for bulk argon case. Periodic boundary conditions were applied in all three directions. The green spheres represent argon atoms.

average density of the system was varied from 70% to 100% of the saturated liquid argon density at atmospheric pressure (0.1 MPa) by adjusting the height of the box between 4.2 and 6 nm. The coordinates of every atom in the system was recorded every 20 ps. We identify a stable bubble visually as a region with density less than 20% of the density of the surrounding fluid with a size larger than 1 nm that can be observed over 400 ps.

Fig. 4.3a shows a typical argon atom configuration when the density of the liquid was $0.84\rho_{0,argon}$, where $\rho_{0,argon}$ is the density of saturated liquid argon under atmospheric pressure (1397 kg/m^3). No bubble was observed in this case over the whole simulation period of 3 ns. Fig. 4.3b shows a typical argon atom configuration when the density of argon was $0.70\rho_{0,argon}$ and a stable bubble was observed in this case. In general, we found that large, stable bubbles were formed at $T = 100$ K when $\rho < 0.8\rho_{0,argon}$, which is in agreement with the molecular dynamics results published by several others (Kinjo & Matsumoto 1998; Park et al. 2000; Wu & Pan 2003).

The bubble shown in Fig. 4.3b has a cylindrical shape with a diameter of approximately 2.5 nm and a length of 5 nm, which took approximately 1 ns to form. Once formed, the bubble is observed to be stable for the rest of the simulation period of approximately 2 ns. The nucleation rate was estimated as the inverse of the product of the bubble volume and the time taken for the bubble to form. At $T = 100$ K, the nucleation rate calculated for argon in the NVT system was 4×10^{28} cm^{-3}s^{-1}, which is close to the values reported in the literature (Kinjo & Matsumoto 1998; Kinjo et al. 1999). In conclusion, we believe that our molecular dynamics code and model parameters reproduce previously published results.

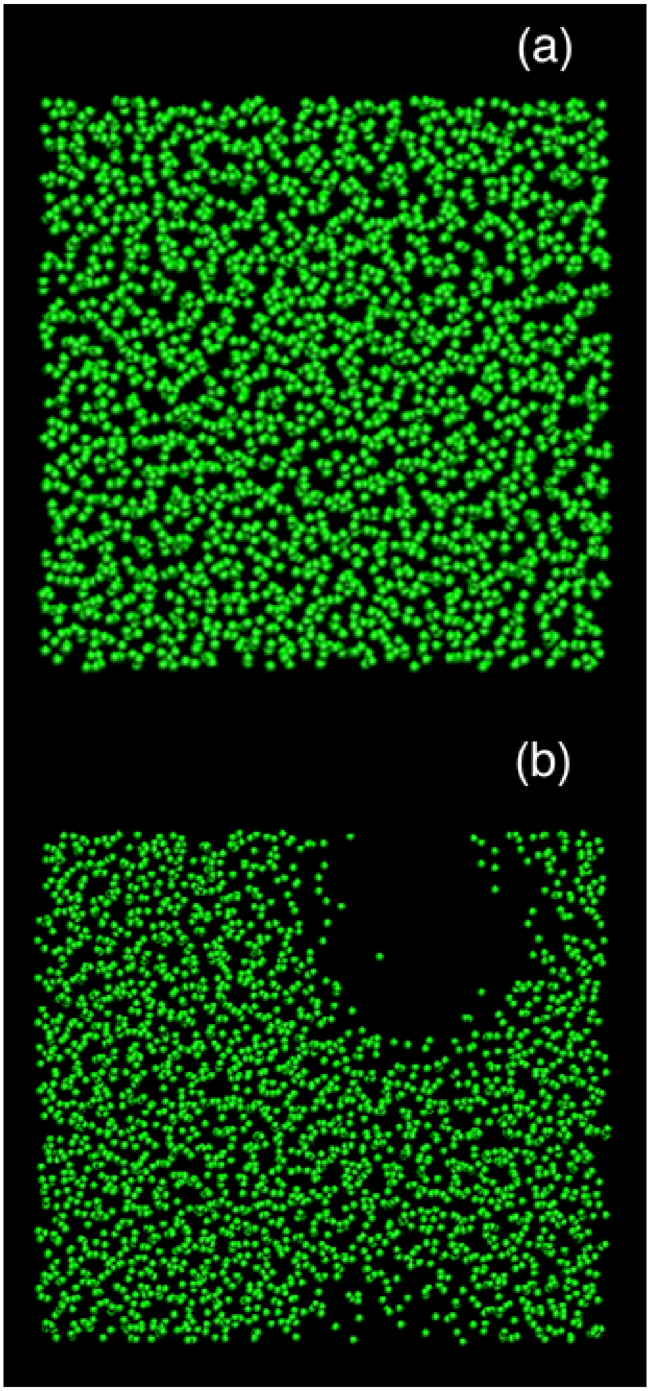

Figure 4.3: (a) No bubbles observed for the argon NVT case at $T = 100$ K, $\rho = 0.84\rho_{0,argon}$, as expected. b) Stable bubble formed for the argon NVT system with $T = 100$ K and $\rho = 0.70\rho_{0,argon}$. The green spheres represent argon atoms. For scale, the diameter of the bubble shown in (b) is ~ 2.5 nm.

4.5.2 Water NVT Case

The canonical (NVT) ensemble of water contains 2008 water molecules in a simulation box similar to Fig. 4.2 with dimensions of $x = y = 4.34$ nm and $z \sim 3 - 5$ nm. The height of the simulation box was varied to adjust the average density of water in the system to be 60% to 100% of the saturated liquid water density at 0.1 MPa and 450 K ($\rho_{0,water} = 958$ kg/m^3). The total simulation time was 2 ns.

For the water NVT systems, we observed stable bubbles when $\rho < 0.74\rho_{0,water}$. The critical relative average density ($0.74\rho_{0,water}$) for observing bubble formation is smaller than that for the argon case ($0.8\rho_{0,argon}$ from Sect. 4.5.1), possibly associated with the different intermolecular potentials of argon and water. Fig. 4.4a shows a typical water molecule configuration when the average density is higher than the critical average density, and Fig. 4.4b shows one when the average density is lower than the critical average density.

The bubble in Fig. 4.4b has a cylindrical shape with a diameter of approximately 2 nm and a length of 4 nm. The bubble formation time in this case is approximately 200 ps, which is shorter than the formation time reported earlier for the Ar bubble. The calculated nucleation rate in this case was 4×10^{29} cm^{-3}s^{-1}, which is in consistent with the fact that the homogeneous nucleation rate of water is generally higher than that of argon (Carey, 1992).

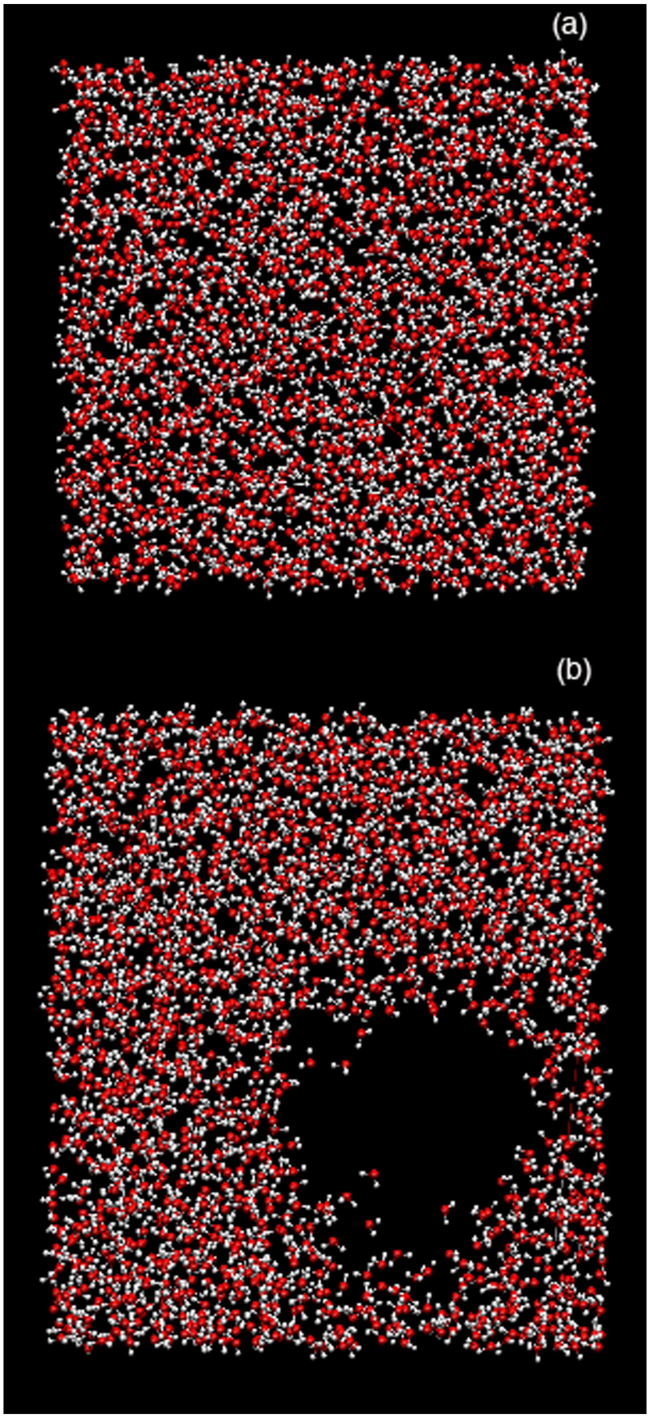

Figure 4.4: (a) No bubbles observed for the water NVT case at T = 450 K, $\rho = 0.95\rho_{0,water}$. b) Stable bubble formed in the water NVT system at T = 450 K, $\rho = 0.66\rho_{0,water}$. The red spheres represent oxygen atoms and the white spheres represent hydrogen atoms. For scale, the diameter of the bubble shown in (b) is ~ 2 nm.

4.6 Thermal Bubble Formation in NPT Systems

Having confirmed that our code can generate results similar to those reported in the literature, and using results of NVT systems as a comparison base, we then performed simulation of thermal bubble nucleation in the more realistic isothermal-isobaric (NPT) ensemble for both argon and water.

4.6.1 Argon NPT Case

A typical snapshot of the argon NPT system is shown in Fig. 4.5, where the argon atoms were sandwiched by two silicon plates in the z-direction. There were four layers of Si atoms in each wall, consisting of 800 neutral Si atoms rigidly arranged in a diamond lattice with its (100) surface in contact with argon.

First, the NPT system was modeled under a constant pressure of 0.1 MPa. In all simulations, we equilibrated our system until the top silicon wall oscillated within a distance of less than 1Å. This ensured that the overall pressure in our system was indeed kept constant. Under a constant pressure of 0.1 MPa, we did not observe any stable bubbles generated at $T = 100$ K for a simulation period of 3 ns. Furthermore, no stable bubble was observed even when the system temperature was raised up to $T = 120$ K, the superheat limit for argon. The snapshots of argon atoms in the confined silicon nanoslits at $T = 100$ K and $T = 120$ K are shown in Figs. 4.6a and 4.6b, respectively.

To study whether thermal bubble formation would occur under lower pressure, we modeled argon NPT systems at $T = 100$ K and 120 K with external pressures

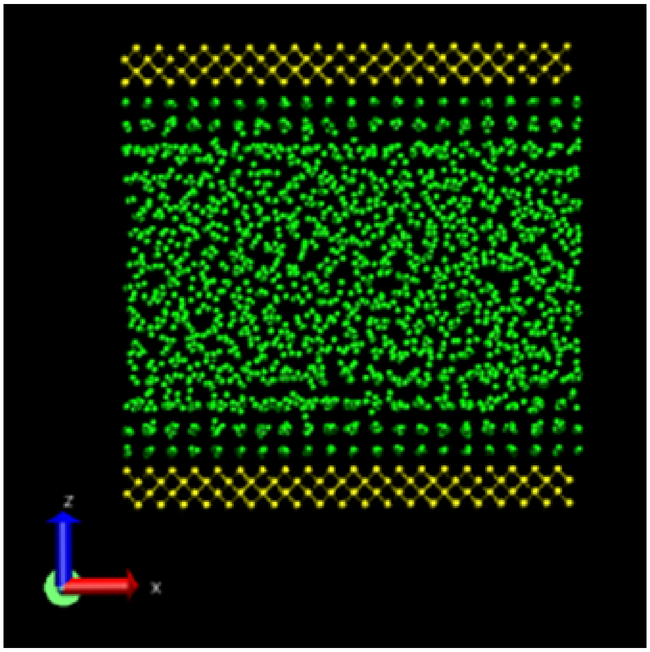

Figure 4.5: Schematic of the simulation box used for argon NPT case. The x and y dimensions of the simulation box are 5.43 nm and the z dimension of the box was controlled by the net pressure of the system. The yellow spheres represent silicon atoms and the green spheres represent argon atoms.

varying from 0.01 MPa to 0.1 MPa. No bubble formation was observed in any of these cases. Fig. 4.7 shows the variation of the relative average density of the nano-confined argon ($\rho/\rho_{0,argon}$) as a function of the external pressure of the system. The relative average density of nano-confined argon was calculated by dividing the total number of argon atoms in the system by the volume of the nanochannel box at equilibrium and normalizing by the average density of saturated liquid argon at atmospheric pressure ($\rho_{0,argon}$). We found that the average density of nano-confined argon changed negligibly as the external pressure of the system was reduced. This indicates that nano-confined argon behaves like a liquid with low compressibility even when the system temperature was close to the superheat limit of argon.

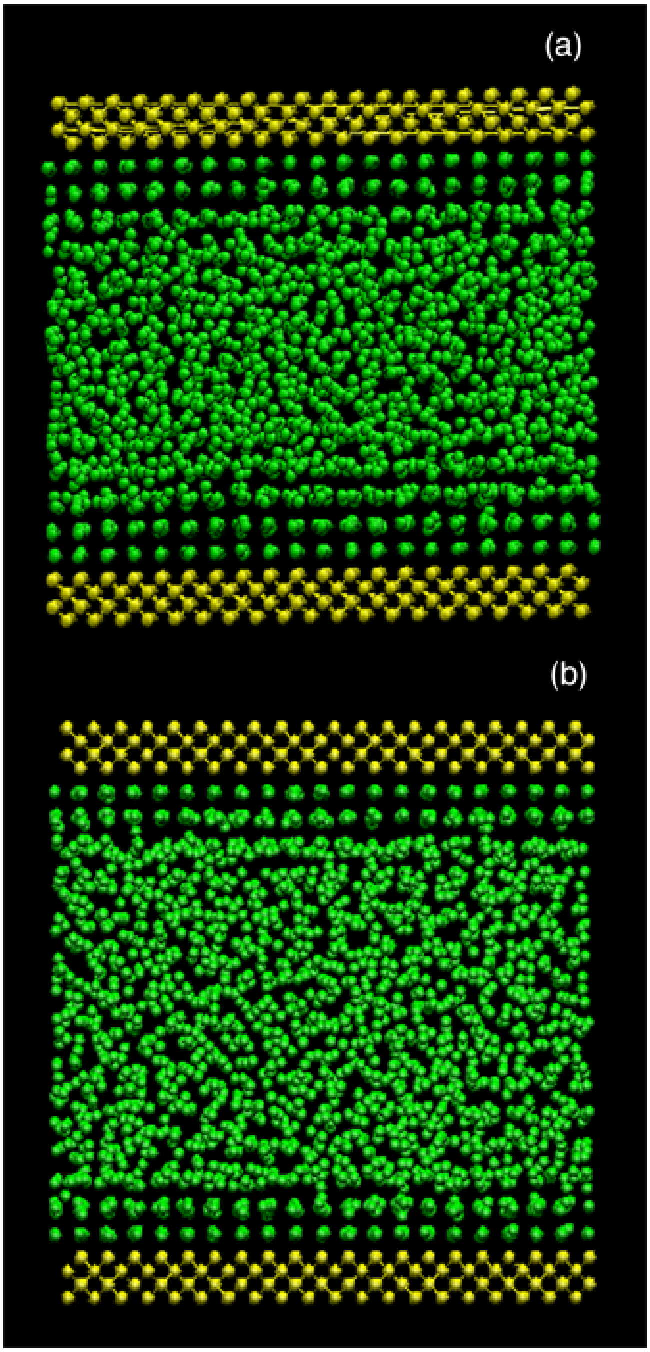

Figure 4.6: (a) No bubbles observed for argon NPT case at T = 100 K, and (b) T = 120 K. The average density of the argon in the nanochannel was $0.96\rho_{0,argon}$ at T = 100 K and $0.86\rho_{0,argon}$ at T = 120 K. The pressure of the system was kept constant at 0.1 MPa. The yellow spheres represent channel wall atoms and green spheres represent argon atoms.

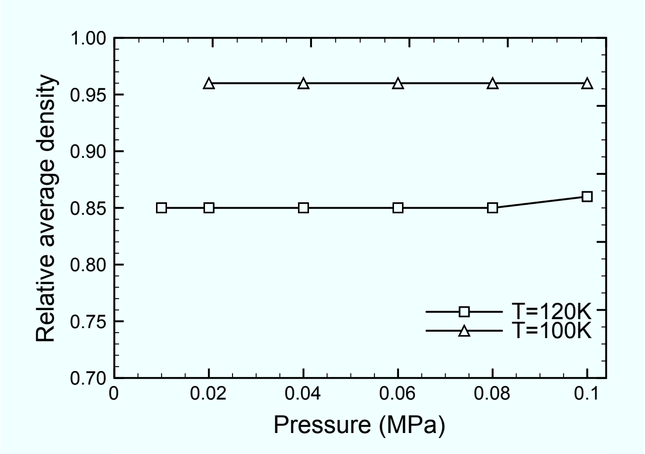

Figure 4.7: Average relative density ($\rho/\rho_{0,argon}$) of argon in the nanochannel as a function of external pressure for argon NPT systems at two different temperatures, $T = 100$ K and $T = 120$ K.

4.6.2 Water NPT Case

Similar to the argon NPT case, the bubble nucleation process was modeled for water using a NPT system with dimensions $x = y = 4.34$ nm. The distance between the silicon plates in the z-direction was controlled by the net pressure of the system similar to that for the NPT argon system.

The water NPT system was first modeled under a constant pressure of 0.1 MPa for different temperature from 450 K to 540 K. No stable bubble was observed for any cases for a simulation time of 2 ns, which is true even when the system temperature was raised to approximately $T = 540$ K, the superheat limit of water. Figs. 4.8a and 4.8b show the snapshots of water molecules at $T = 450$ K and $T = 523$ K, respectively. The average density of water molecules shown in Figs. 4.8a and 4.8b was $0.81\rho_{0,water}$ at $T = 450$ K and $0.70\rho_{0,water}$ at $T = 523$ K respectively.

The water NPT system was also simulated under a reduced external pressure of

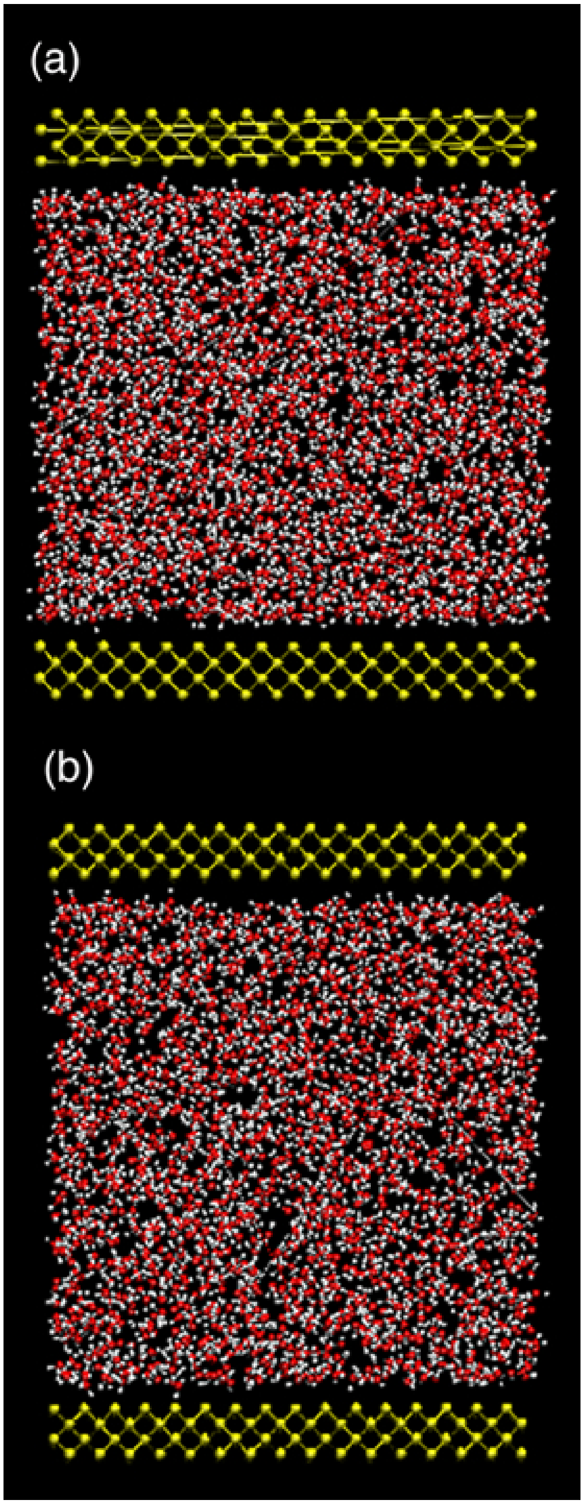

Figure 4.8: No bubbles observed for the water NPT case at (a) $T = 450$ K, and (b) $T = 523$ K. The average density of the water in the nanochannel was $0.81\rho_{0,water}$ for $T = 450$ K and $0.70\rho_{0,water}$ for $T = 523$ K. The pressure of the system was kept constant at 0.1 MPa. The yellow spheres represent Si channel wall atoms, red spheres represent oxygen atoms and white spheres represent hydrogen atoms.

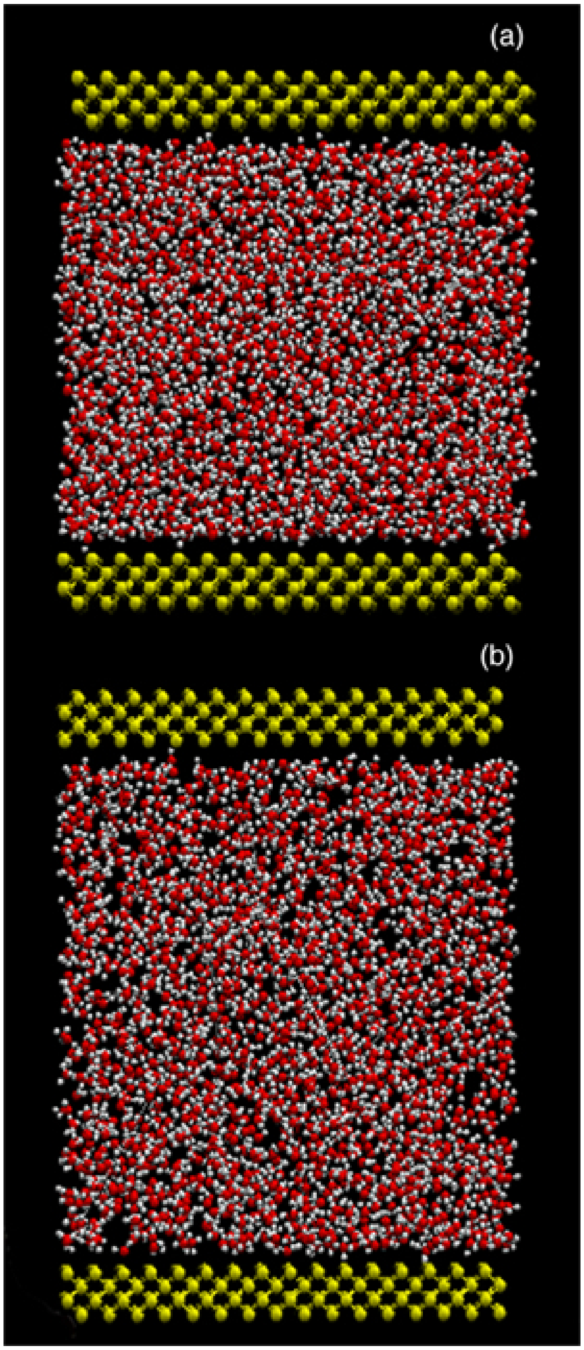

Figure 4.9: No bubble formation in water was observed up to a simulation time of 2 ns when external pressure was reduced to 0.01 MPa at (a) $T = 450$ K, and (b) $T = 540$ K. The average density of the water in the nanochannel was $0.80\rho_{0,water}$ for $T = 450$ K and $0.65\rho_{0,water}$ for $T = 540$ K. The pressure of the system was kept constant at 0.01 MPa.

0.01 MPa at $T = 450$ K and $T = 540$ K to observe whether bubble formation would occur when the system pressure was reduced. Figs. 4.9a and 4.9b show snapshots of the water molecules at $T = 450$ K and $T = 540$ K under a pressure of 0.01 MPa, respectively. The average density of water molecules was $0.80\rho_{0,water}$ at $T = 450$ K, and $0.65\rho_{0,water}$ at $T = 540$ K. Figs. 4.9a and 4.9b indicate that no bubble forms even under reduced pressure and elevated temperature. The average water density in the nanochannel when the external pressure is 0.01 MPa ($\rho = 0.80\rho_{0,water}$ at $T = 450$ K) is very close to the average density when the external pressure was 0.1 MPa ($\rho = 0.81\rho_{0,water}$ at $T = 450$ K), which indicates that nano-confined water, just like nano-confined argon, behaves like a liquid with low compressibility even when the system temperature is close to the superheat limit of water.

4.7 Discussion

4.7.1 Effect of Pressure Waves in Bubble Nucleation in NPT Systems

Our results indicate that thermal bubble nucleation is suppressed in nano-confined NPT systems, compared to the bulk, NVT systems. To understand our simulation results, we consider the physical process for thermal bubble nucleation. During thermal bubble nucleation, the bubble compresses the liquid around it and generates a pressure disturbance to adjust the arrangement of the liquid. The pressure disturbance propagates in the liquid as a pressure wave. We believe that in nano-confined spaces, the pressure disturbance will travel to the channel wall, where it will be reflected back to the bubble nucleation site and suppress bubble formation. The effects of pressure waves on bubble nucleation were first discussed by Zhang et al. (2000) in a theoretical effort to understand why very high superheat temperatures were required to observe bubbles in microchannels. Using iterative, numerical computations, they estimated the nucleation rate and maximum superheat temperature required for successful bubble nucleation in methanol in microchannels by assuming that the nucleation time is equal to the time taken for the pressure wave to reflect off the channel wall back to the nucleation region. They obtained qualitative agreement between their theoretical prediction for the superheat limit for bubble nucleation in methanol as a function of microchannel diameter and the experimental results.

Here, we extend this pressure wave concept to explain why bubble nucleation is not observed in nano-confined NPT simulations. The pressure wave explanation requires that the time for the pressure wave to travel to the channel wall and back must be much less that the time for bubble nucleation. Only then can we attribute the suppression of bubble nucleation to the effect of the pressure wave. Therefore, we define and compare two characteristic times: t_{nuc}, which is the time taken for a bubble to form, grow and stabilize in size, and t_{press}, which is the time required for the pressure wave to travel to and from the nanochannel walls back to the bubble nucleation site. t_{nuc} was estimated from the corresponding NVT systems at the same temperature and reduced density by visually estimating how many timesteps were required for a stable bubble to form from a atomic configuration where no bubbles were observed.

A time-sequence of frames illustrating the growth and stabilization of a bubble formed in the argon NVT system is shown in Fig. 4.10. In practice, we start from a

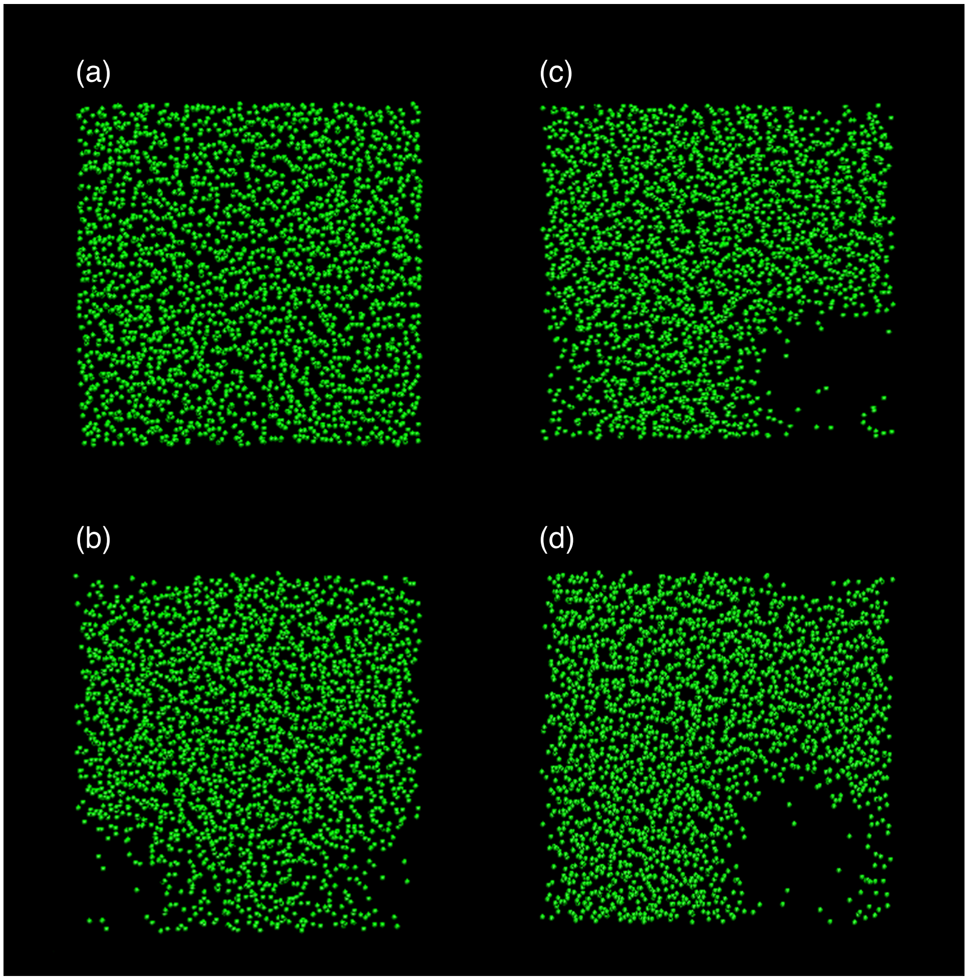

Figure 4.10: Sequence of frames showing argon atom configuration in the NVT system with $T = 100$ K and $\rho = 0.70\rho_{0,argon}$. (a) Argon atom configuration just before bubble nucleation process begins. We will define this as $t = 0$ ps. (b) Small density fluctuation begins to form near the side of the simulation box, $t = 140$ ps. (c) Clear, stable bubble observed at $t = 840$ ps, just as the bubble stabilizes, and again at (d) $t = 2$ ns.

timestep where a clear, stable bubble is observed, as shown in Fig. 4.10d and track the argon atom configuration backwards in time until we find the earliest timestep where we still recognize the stable bubble. This corresponds to Fig. 4.10c, and this frame marks the completion of the bubble formation process. Now, we continue tracking the argon atom configuration backwards in time until we observe a relatively uniform distribution of argon atoms with no sign of bubble formation, as illustrated by Fig. 4.10a. Fig. 4.10b shows a snapshot of the intermediate argon atom configuration as the bubble is forming in the simulation system. Thus, we estimate t_{nuc} to be the difference in time between the atomic configurations shown in Figs. 4.10c and 4.10a. In the example shown, $t_{nuc} \sim 840$ ps. Eq. 4.14 was used to estimate t_{press}.

$$t_{press} = \frac{L}{v_{sound}} \tag{4.14}$$

where L is the distance traveled by the pressure wave, which is taken as twice the height of the nanochannel system, and v_{sound} is the speed of pressure waves in the liquid. In the calculation of t_{press}, we have assumed the v_{sound} to be ~ 820 ms^{-1} for argon and ~ 1500 ms^{-1} for water (Lide, 2002).

The values of t_{nuc} and t_{press} for argon and water NPT systems are tabulated in Table 4.2. Table 4.2 clearly indicates that for both argon and water, the characteristic times for the pressure waves are about one order of magnitude less than bubble nucleation times.

To further test the above argument, we constructed a model of virtual argon with modified intermolecular interaction strength. The purpose was to investigate

Table 4.2: Calculated values of t_{nuc} and t_{press} for three different simulations cases. The virtual argon case refers to the NPT case where the strength of the liquid-liquid interaction was reduced by 20%, i.e. $\beta = 0.8$.

Parameter\Fluid type	Real argon ($\beta = 1$)	Virtual argon ($\beta = 0.8$)	Water
T (K)	100	100	450
t_{nuc} (ps)	840	10	180
t_{press} (ps)	12	12	6
Bubbles?	No	Yes	No

whether thermal bubbles could be generated in a liquid with different intermolecular interactions, and how the characteristic times for the pressure waves and bubble nucleation compared with each other. For the virtual argon fluid, we applied a scale factor β to vary the strength of the liquid-liquid energy parameter with β varying from 0.1 to 2.0. $\beta < 1$ corresponds to cases where the liquid-liquid interaction is weaker than the typical Ar-Ar interaction, and $\beta > 1$ corresponds to cases where the liquid-liquid interaction is stronger than the typical Ar-Ar interaction. We call these liquids virtual argon as their intermolecular potentials are scaled from real argon. Simulations were performed at $T = 100$ K with an external pressure of 0.1 MPa. All other simulation conditions were kept the same as the argon NPT case reported in section 4.6.1.

Fig. 4.11 shows the relative average density of the liquid confined in the nanochan-

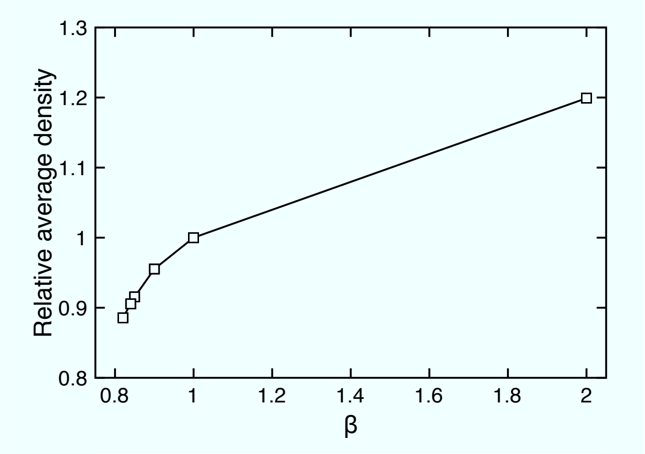

Figure 4.11: Plot of relative average density of fluid in the nanochannel as a function of the strength of liquid-liquid interaction at $T = 100$ K. $\beta = \epsilon_{liq-liq}/1.67 \times 10^{-21}$ J. The relative average density of the fluid in the nanochannel was calculated by normalizing the average density of the fluid in the nanochannel for each simulation case by the average density of argon in the nanochannel ($\beta = 1$).

nel as a function of β. The relative average density of the liquid was calculated by dividing the calculated average liquid density in the simulation domain by the average density of argon in the nanochannel (i.e. $\beta = 1$ case). We observed a reduced average density of the liquid as the strength of the liquid-liquid interaction is weakened. At 100 K, the saturation pressure for argon is approximately 0.3 MPa, which is higher than 0.1 MPa. This means that the intermolecular potential holds the molecules together and a reduced strength of the intermolecular potential would allow greater separation of the molecules.

For the virtual argon, we found that no bubble would form for a simulation time of 3 ns when $\beta \geq 0.82$ corresponding to $\epsilon_{liq-liq} \geq 1.37 \times 10^{-21}$ J. For $\beta < 0.82$, an unstable bubble would form and expand rapidly such that its size would exceed the size of our simulation domain. Fig. 4.12a shows a snapshot of the configuration of the liquid atoms when $T = 100$ K, $\beta = 0.9$. No bubble can be observed in the system. Fig. 4.12b shows a snapshot of an unstable bubble forms when $T = 100$ K, $\beta = 0.8$ after 80 ps. The bubble shown in Fig. 4.12b has a diameter of ~ 4 nm and length 5 nm and expands so rapidly that the top Si channel wall exceeds our simulation box size after 134 ps.

To extract the bubble nucleation time, t_{nuc}, we also performed a simulation of an NVT system with reduced intermolecular interaction of 1.34×10^{-21} J ($\beta = 0.8$) at $T = 100$ K in a manner similar to that reported in Sect. 4.5.1 for consistency. The NVT simulation box height was varied from 6 - 9 nm and we observed a stable bubble for the $\beta = 0.8$ case when the average density of the fluid was less than or equal to $0.53\rho_0$. From the NVT simulations, t_{nuc} was estimated to be 10 ps in the same manner as for the argon and water cases. To calculate t_{press} for the virtual argon, we took L as twice the height of the nanochannel box just before the bubble was observed. The speed of the pressure waves was taken as that for real argon (820 ms^{-1}), which should be larger than the acoustic speed in the virtual argon of lower density. Therefore, the calculated t_{press} should be a conservative value smaller than the actual value. For the virtual argon case, the calculated t_{press} (12 ps) was larger than t_{nuc} (10 ps). Correspondingly, a thermal bubble was observed in the simulation. This further supports the hypothesis that thermal bubble formation in an NPT system depends on the competition between the rate of bubble nucleation and suppression by the reflected pressure waves.

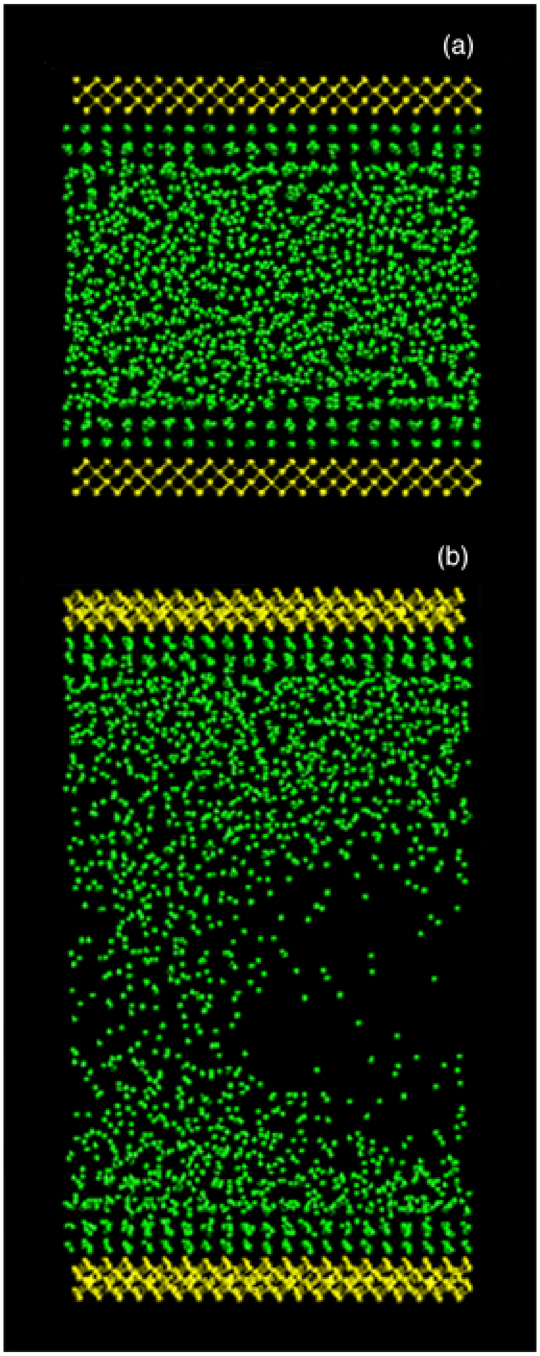

Figure 4.12: (a) Configuration of fluid molecules at $T = 100$ K, $\beta = 0.9$. No bubbles observed up to a simulation time of 3 ns. (b) Snapshot of unstable bubble shown at $T = 100$ K, $\beta = 0.8$ at $t = 80$ ps. Bubble shown has diameter ~ 4 nm and length 5 nm.

4.7.2 Effect of Solid-Liquid Interactions

Due to the presence of solid channel walls in close proximity to the fluid atoms, the strength of the solid-liquid interactions is expected to be an important parameter influencing bubble nucleation in nanochannels. As discussed in Sect. 4.4.2, Novak et al. (2007) recently reported a molecular dynamics study of bubble nucleation rate in a Lennard-Jones liquid when confined between two plates of arbitrary material using an isobaric-isothermal (NPT) system. In their simulations, they allowed the fluid atoms to interact with the top channel wall through a mean field 9-3 potential, and with the bottom channel wall through a 6-12 L-J potential. They investigated three distinct cases (strong, neutral & weak) where the strength of solid-liquid interaction with the bottom wall only was varied. They observed bubble nucleation in all three cases and found that the nucleation rate was fastest when the solid-liquid interaction was weak. Their strong, neutral and weak solid-liquid interaction cases corresponded to values of 1.67×10^{-21} J, 8.35×10^{-22} J and 2.64×10^{-21} J for the 6-12 L-J (i.e. bottom wall interaction) solid-liquid energy parameter, $\epsilon_{sol-liq}$.

Instead of using the 9-3 potential, which essentially can be derived from the 6-12 L-J potential through a series of integrations in space, we allow the fluid atoms to interact with both the top and bottom wall using a 6-12 L-J potential, starting with $\epsilon_{sol-liq} = \epsilon_{Ar-Si} = 5.2 \times 10^{-21}$ J, as reported in Table 4.1. We vary the solid-liquid interaction strength by introducing a multiplicative scale factor, α, for the solid-liquid energy parameter such that $0.01 \leq \alpha \leq 2$. Thus, our range of solid-liquid interaction strengths correspond to 5.2×10^{-23} J $\leq \epsilon_{sol-liq} \leq 1.0 \times 10^{-20}$ J, which covers and extends the range of solid-liquid interaction strengths studied by Novak et al. $\alpha < 1$ represents cases where the solid-liquid interactions are weaker than the original Ar-Si interaction (i.e., more hydrophobic), whereas $\alpha > 1$ represents cases where the solid-liquid interactions are stronger than the Ar-Si interaction (i.e., more hydrophilic). Simulations were carried out at two different temperatures (T = 100 K and T = 120 K) with the external pressure fixed at 0.1 MPa. All other simulation conditions were kept the same as the argon NPT case reported in Sec. 4.6.1.

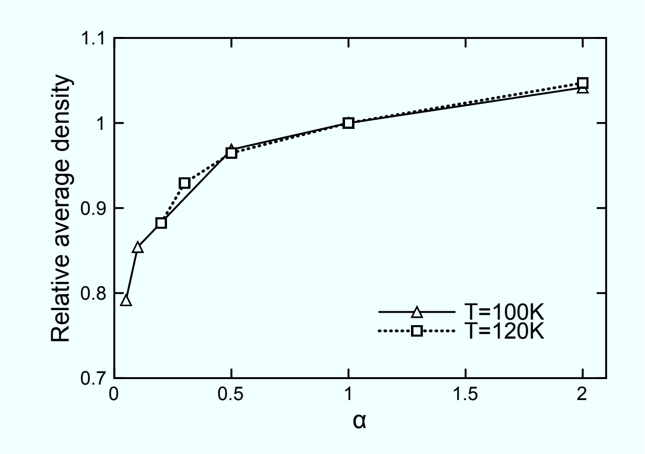

Figure 4.13: Plot of relative average density of fluid in the nanochannel as a function of the strength of solid-liquid interaction at $T = 100$ K and 120 K. $\alpha = \epsilon_{sol-liq}/5.22 \times 10^{-21}$ J. The relative average density of the fluid in the nanochannel was calculated by normalizing the average density of the fluid in the nanochannel for each simulation case by the average density of argon in the nanochannel ($\alpha = 1$) at the corresponding temperature.

Fig. 4.13 shows a plot of the relative average densities of the liquid in the nanochannel as a function of α at $T = 100$ K and 120 K. The relative average density of the liquid in the nanochannel for each simulation case was obtained by dividing the calculated average density by the average density of argon in the nanochannel ($\alpha = 1$) at the corresponding temperature. Similar to the case of the liquid-liquid intermolecular interaction, the average density of the liquid in the nanochannel increased with a stronger solid-liquid interaction and vice-versa.

No bubbles were found in simulations at $T = 100$ K when $\alpha \geq 0.05$ ($\epsilon_{sol-liq} \geq 2.6 \times 10^{-22}$ J). When $\alpha < 0.05$, a bubble formed and grew rapidly such that the size of the bubble quickly exceeded our simulation box size, causing the simulations to terminate. Fig.4.14a shows a snapshot of an unstable bubble seen at $T = 100$ K, $\alpha = 0.04$ ($\epsilon_{sol-liq} = 2.1 \times 10^{-22}$ J) after 140 ps, just before the top Si channel wall of our system expanded beyond our simulation box because of rapid bubble growth. At $T = 120$ K, we found no bubbles when $\alpha \geq 0.2$ ($\epsilon_{sol-liq} > 1.0 \times 10^{-21}$ J). Below this threshold value, similar to the $T = 100$ K cases, we found that a bubble formed and grew to exceed the simulation box. Fig. 4.14b shows a snapshot of an unstable bubble seen at $T = 120$ K, $\alpha = 0.1$ after 100 ps. The bubble shown in Fig. 4.14b expanded so rapidly that the top channel wall expanded beyond our simulation box within 190 ps.

In summary, we could only observe bubble nucleation when the strength of the solid-liquid interaction is below a certain threshold value at both $T = 100$ K and $T = 120$ K. This observation can be understood qualitatively. When the solid-liquid interaction is strong, the liquid atoms are strongly bound to the solid walls. As such, they are rendered almost immobile and are not available to participate in the bubble formation process. Thus, bubble formation is not observed for strong solid-liquid interactions. When the solid-liquid interaction is sufficiently weak, the liquid

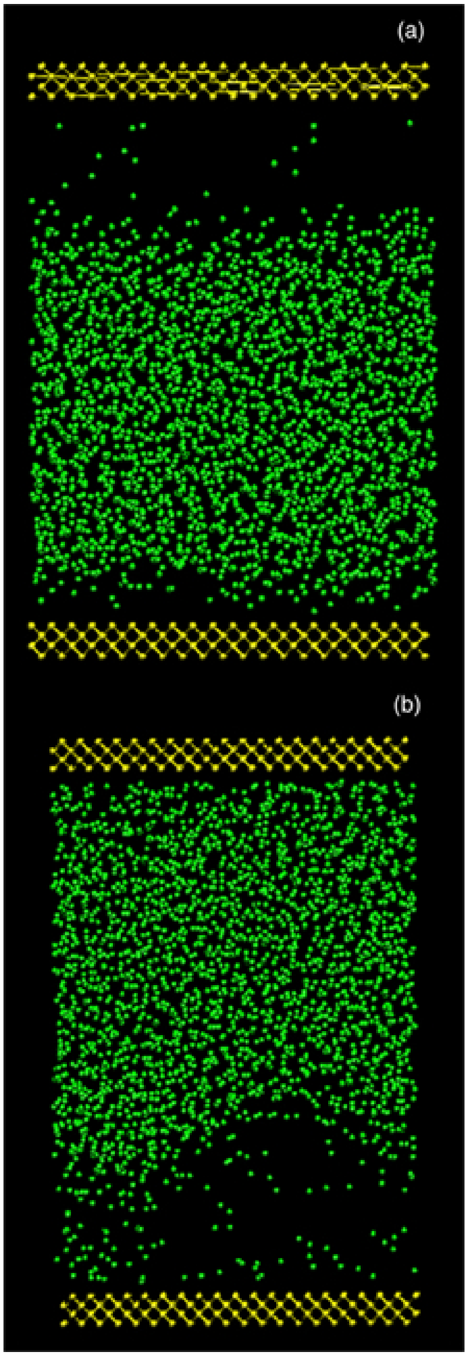

Figure 4.14: (a) Bubble observed to be forming at the top Si plate for argon NPT case at $T = 100$ K with $\alpha = 0.04$ ($\epsilon_{sol-liq} = 2.1 \times 10^{-22}$ J). This snapshot was taken at $t = 140$ ps, just before the simulation terminated because of rapid bubble growth. The bubble shown has a cuboid shape with length ~ 5 nm and height ~ 3 nm. (b) Bubble observed to be forming at bottom Si plate for argon NPT case at $T = 120$ K with $\alpha = 0.1$ ($\epsilon_{sol-liq} = 5.2 \times 10^{-22}$ J). This snapshot was taken at $t = 100$ ps, and the bubble is cylindrical in shape with length ~ 5 nm and diameter 4 nm.

atoms are weakly bound to the solid walls and so, more likely to participate in the bubble formation process. It must be noted that direct comparison of our results with Novak's work (Novak et al., 2007) is not possible because they use different simulation conditions (temperature and pressure) and different mathematical formalism (i.e. the use of the 9-3 potential to model interaction with top wall) to model bubble nucleation in nanochannels.

4.8 Summary

Molecular dynamics studies of bubble nucleation process were carried out using both NVT and NPT systems for both argon and water. Results using NVT systems show that we are able to reproduce previously published results, which indicate that our molecular dynamics code works properly. The modeling of bubble nucleation process using (NPT) systems indicates that no bubble formation for either argon or water under an external pressure of 0.01 - 0.1 MPa even when the temperature approaches the limit of superheat. This observation is consistent with the hypothesis that bubble nucleation in nano-confined liquids can be suppressed by a pressure wave generated inside the nanochannel during bubble nucleation. The generated pressure wave travels toward the channel walls, reflects off the solid walls back toward the bubble nucleation site and suppresses bubble nucleation. Comparison of the calculated characteristic times for the pressure wave and bubble nucleation indicates that bubble nucleation in the NPT system is suppressed when the characteristic time for the pressure wave is much shorter than the bubble nucleation time. To further examine this hypothesis, the liquid-liquid interactions are varied to alter the two characteristic times, and results show that when the characteristic time for the pressure wave is larger than the bubble nucleation time, bubble nucleation does occur in NPT systems. We also investigate the effect of the strength and representation of solid-liquid interactions on bubble nucleation in nano-confined argon NPT systems. Results indicates that bubbles will not form until the energy parameter of the solid-liquid interaction potential was less than 5% of its original value at $T = 100$ K and less than 20% of its original value at $T = 120$ K. Below these threshold values, bubbles will form almost spontaneously and grow rapidly. This result can be understood qualitiatively because when the solid-liquid interaction is strong, the liquid atoms are strongly bound to the solid walls and are almost immobile. Hence, these atoms are unavailable to participate in the bubble formation process. Bubble formation is thus less likely because few atoms are available to participate in the bubble formation process. However, when the solid-liquid interaction is sufficiently weak, the liquid atoms are no longer bound strongly to the solid walls, and are available to participate in the bubble formation process, making the process more likely.

CHAPTER V

CONCLUSIONS

Part One: Experimental Work

Experimentally, we have developed a new sensing scheme integrating a MOSFET with a fluidic device. Particles are detected by monitoring the MOSFET drain current instead of the ionic current through the fluidic circuit as in traditional resistive pulse sensors. The sensing scheme was first tested and characterized in detail using a microfluidic device fabricated in PDMS (Chapter II). We demonstrated that this MOSFET-based resistive pulse sensor can increase sensitivity by amplifying the percentage of the modulation caused by the translocation of particles through the sensing channel. Several different micron-scale polystyrene microbeads were detected using the MOSFET-based microfluidic resistive pulse sensor, and the detected minimum volume ratio between the particle and the sensing channel was found to be 0.006 %, $\sim$10 times smaller than the lowest volume ratio previously reported in the literature. The sensitivity of the MOSFET-based resistive pulse sensor was characterized as a function of MOSFET gate voltage. It was shown that the device was more sensitive when operated in the sub-threshold region as compared to the saturation region. In addition, the sensitivity with respect to the applied electrokinetic bias, V_{-}, was also investigated and it was shown that the relative drain current modulation varied linearly with V_{-}. We also showed that the MOSFET-based microfluidic resistive pulse sensor can distinguish particles of both different sizes and of similar size but different surface charges, based on the observed amplitude of the MOSFET drain current modulation and the translocation time. It was shown that the size dispersion of 9.86 μm in diameter polystyrene beads measured with the MOSFET-based resisitve pulse sensor was comparable to that from direct SEM observation.

Next, we extended this sensing scheme to the nanoscale by fabricating a nanofluidic device, also in PDMS (Chapter III). Using a sensing nanochannel that was $\sim$ 350 nm wide, 500 nm deep and 5 μm long, we successfully detected 210 nm-diameter nanobeads, corresponding to a volume ratio of 0.48 %. Based on the experimental insights we have gained from these preliminary investigations and further experimental optimization, we believe that we can achieve the same sensitivity with the nanofluidic sensor as with the microfluidic sensor reported in Chapter II. In principle, this will allow us to sense nanoparticles as small as 46 nm in diameter with the same sensing nanochannel reported above. Thus, our new sensing scheme will reduce the stress on fabrication technology to make sensing nanochannels of the same size as the nanoparticles being detected, as currently required for traditional resistive pulse sensors.

Part Two: Computational Work

In recent experimental studies of nanopore-based resistive pulse sensors, nanobubbles have been cited as a possible source of noise in the ionic current measurements. Due to the rapid growth and availability of computing power and the challenges of studying nanobubble formation experimentally, we carried out molecular dynamics simulations of thermal bubble nucleation in nanochannels (Chapter IV) to investigate whether nanobubbles can indeed form in nanochannels and thus, be a valid source of noise in nanofluidic experiments.

Molecular dynamics studies of bubble nucleation process were carried out using both NVT and NPT systems for both argon and water. Using NVT systems, we showed that we are able to reproduce previously published results, which indicate that our molecular dynamics code works properly. The modeling of bubble nucleation process using (NPT) systems indicated no bubble formation for either argon or water under an external pressure of 0.01 - 0.1 MPa even when the temperature is approaching the limit of superheat. This observation is consistent with the hypothesis that bubble nucleation in nano-confined liquids can be suppressed by a pressure wave generated inside the nanochannel during bubble nucleation. The generated pressure wave travels toward the channel walls, reflects off the solid walls back toward the bubble nucleation site and suppresses bubble nucleation. Comparison of the calculated characteristic times for the pressure wave and bubble nucleation indicates that bubble nucleation in the NPT system is suppressed when the characteristic time for the pressure wave is much shorter than the bubble nucleation time. To further examine this hypothesis, the liquid-liquid interactions are varied to alter the two characteristic times, and results show that when the characteristic time for the pressure wave is larger than the bubble nucleation time, bubble nucleation does occur in NPT systems. To compare with a published molecular dynamics simulation of Lennard-Jones liquid, we also investigate the effect of the strength of solid-liquid interactions. Results indicates that bubbles will not form until the energy parameter of the solid-liquid interaction potential was less than 5% of its original value at T = 100 K and less than 20% of its original value at T = 120 K. Below these threshold values, bubbles will form almost spontaneously and grow rapidly. This result can be understood qualitiatively because when the solid-liquid interaction is strong, the liquid atoms are strongly bound to the solid walls and are almost immobile. Hence, these atoms are unavailable to participate in the bubble formation process. Bubble formation is thus less likely because few atoms are available to participate in the bubble formation process. However, when the solid-liquid interaction is sufficiently weak, the liquid atoms are no longer bound strongly to the solid walls, and are available to participate in the bubble formation process, making the process more likely.

In conclusion, our initial investigations have revealed that it might be difficult to form thermal bubbles in nano-confined systems. This casts doubt on whether nanobubbles can be cited as a source of noise in nanofluidic experiments. We hope our initial findings spur further interest in this field, since much more computational and experimental work is required to fully understand bubble nucleation in nano-confined systems.

APPENDIX A

DERIVATION OF ELECTRO-OSMOTIC & ELECTROPHORETIC FLOW VELOCITIES

When a tangential external electric field is applied to a fluid, the general Navier-Stokes equation for a Newtonian fluid (White, 2006) can be written as

$$\rho_f \frac{\partial \mathbf{u}}{\partial t} = -\nabla p + \eta \nabla^2 \mathbf{u} + \rho_{\mathbf{f}} \mathbf{g} + \rho_{\mathbf{f}} \mathbf{E} \tag{A-1}$$

where ρ_f is the density of the fluid, $\mathbf{u}$ is the velocity of the fluid, p is the fluid pressure, η is the viscosity of the fluid, $\mathbf{g}$ is the gravitational acceleration, and $\mathbf{E}$ is the tangential applied electric field. The left-hand side represents the rate of change of momentum of the fluid at a given location within the flow field. The first term on the right-hand side is the contribution of pressure, the second term is due to viscous forces in the liquid, the third term represents the body force on the liquid due to gravity, and the last term is the body force on the liquid due to an applied electric field. In our derivation, we will assume that:

- the fluid flow is a steady-state flow, i.e. flow velocity is constant with respect to time,
- there is negligible pressure difference within the system,
- the body force due to gravity can be neglected, since the force is perpendicular to the flow direction.

Under these simplifying assumptions, we can rewrite Eq. A-1 in 1-dimension as

$$\eta \frac{d^2u}{dz^2} + \rho_f E = 0 \tag{A-2}$$

Using the 1-D version of Poisson's equation, i.e. $d^2\psi/dz^2 = -\rho_f/\epsilon$, we can rewrite the second term in Eq. A-2 such that

$$\eta \frac{d^2u}{dz^2} - \epsilon E \frac{d^2\psi}{dz^2} = 0 \tag{A-3}$$

It must be noted that for EOF, ψ represents the potential at a particular distance away from a charged solid surface, whereas in EPF, ψ represents the potential at a particular distance away from a charged particle. We will use the subscripts w and p to distinguish between variables due to the charged channel wall (EOF) and variables due to the charged particle (EPF).

First, consider EOF in a nanochannel system as shown in Fig. A-1. The 1-D Poisson's equation that needs to be solved from Eq. 1.3 in this case is

$$\frac{d^2\psi_w}{dz^2} = \frac{2z_i q n_0}{\epsilon} \sinh(\frac{z_i q \psi_w}{kT}) \tag{A-4}$$

The exact solution to the differential equation shown in Eq. A-4 was calculated by Burgreen & Nakache (1964). However, this solution is cumbersome, and we will consider the simplified analysis of Eq. A-4 based on the Debye-Hückel approximation, $z_i q\psi_w/kT << 1$ (Li, 2004). Under this assumption, we can linearize Eq. A-4 such

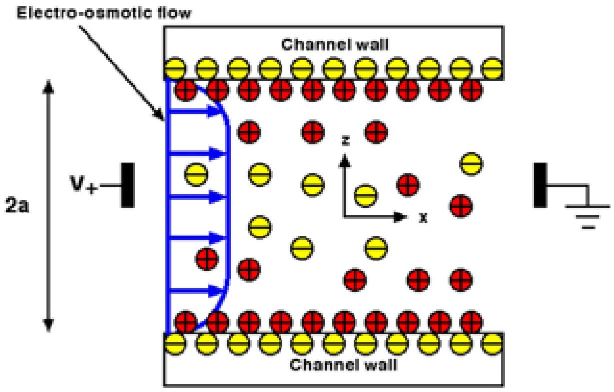

Figure A-1: Schematic of EOF in a slit nanochannel of width $2a$. A positive bias is applied on the left electrode while the right electrode is grounded. The resultant EOF drives fluid from left to right as shown by the arrows.

that

$$\frac{d^2\psi_w}{dz^2} = \frac{\psi_w}{\lambda^2} \tag{A-5}$$

where λ is the characteristic EDL thickness. Applying boundary conditions where the potential at the top and bottom channel surfaces is equal to the zeta potential ($\psi_w(z=a) = \psi_w(z=-a) = \zeta_w$), we get

$$\psi_w(z) = \zeta_w \cdot \frac{|\sinh(z_i/\lambda)|}{\sinh(a/\lambda)} \tag{A-6}$$

Substituting the solution for ψ_w shown in Eq. A-6 back into Eq. A-3, and applying the boundary conditions $u_{EOF}(z=a)$ and $u_{EOF}(z=-a)=0$, we obtain

$$u_{EOF}(z) = -\frac{\epsilon\zeta_w E}{\eta}(1 - \frac{|\sinh(z_i/\lambda)|}{\sinh(a/\lambda)}) \tag{A-7}$$

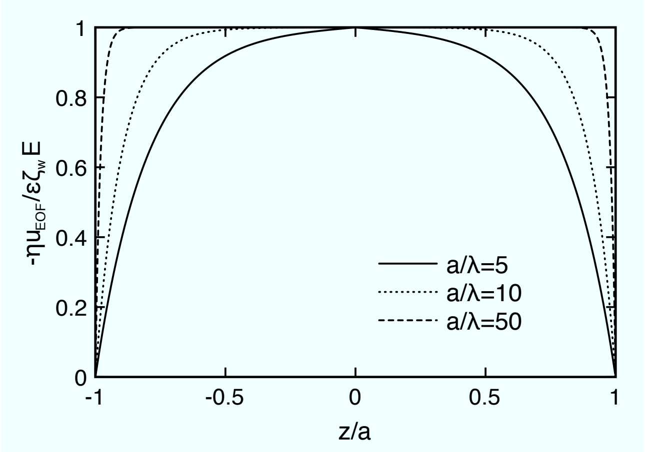

Figure A-2: Plot of normalized EOF velocity, u_{EOF} as a function of normalized distance from the channel wall. Three cases are plotted for varying ratios of channel width:EDL thickness.

The variation of the normalized EOF velocity, $\eta u_{EOF}/\epsilon\zeta_w E$, as a function of normalized distance from the channel walls, z/a, for three different values of the ratio a/λ is shown in Fig. A-2. As can be seen from Fig. A-2, for large values of a/λ, i.e. when the EDL thickness is small compared to the channel width, the EOF velocity is almost constant ($u_{EOF} = -\epsilon\zeta_w E/\eta$) throughout the width of the channel. Significant spatial variation of the EOF velocity only begins to occur when the EDL thickness is comparable to the channel width.

Now, for the case of EPF, consider a spherical charged particle with diameter, d, in a nanochannel system similar to that shown in Fig. A-1. EPF is analogous to EOF except that the charged surface of the spherical particle is considered instead of the charged surface of the channel wall. Hence, using a form similar to Eq. A-7, we can write the EPF velocity, under the assumptions that the zeta potential is small (i.e. $z_i q\zeta_p/kT << 1$), and that the EDL thickness is small compared to the particle diameter, d, as

$$u_{EPF} = \frac{\epsilon \zeta_p E}{\eta} \tag{A-8}$$

where ζ_p is zeta potential of the charged particle. This equation is commonly referred to as the Helmholtz-Smoluchowski equation. A more general formulation for u_{EPF}, valid for arbitrary EDL thickness but still for small zeta potentials, was derived by Henry (1931) and can be written as

$$u_{EPF} = \frac{2\epsilon \zeta_p E}{3\eta} \cdot f(\frac{d}{\lambda}) \tag{A-9}$$

where $f(\frac{d}{\lambda})$ is known as Henry's function and can be given analytically by

$$\begin{aligned} f(\frac{d}{\lambda}) = 1 &+ \frac{1}{16}(\frac{d}{\lambda})^2 - \frac{5}{48}(\frac{d}{\lambda})^3 - \frac{1}{96}(\frac{d}{\lambda})^4 + \frac{1}{96}(\frac{d}{\lambda})^5 \\ &+ \frac{1}{8}(\frac{d}{\lambda})^4 e^{d/\lambda}\left(1 - \frac{(d/\lambda)^2}{12}\right)\int_{d/\lambda}^{\infty}(\frac{e^{-t}}{t})dt \end{aligned} \tag{A-10}$$

Fig. A-3 shows the variation of Henry's function, $f(\frac{d}{\lambda})$, as a function of d/λ. As can be seen from Fig. A-3, Henry's function tends to 1.5 when $d/\lambda >> 1$. Hence, Eq. A-9 simplifies to Eq. A-8 when , i.e. EDL thickness small compared to particle diameter. When $d/\lambda << 1$, i.e. EDL thickness much larger than particle diameter, Henry's function tends to 1, and so the EPF velocity becomes $u_{EPF} = 2\epsilon\zeta_p E/3\eta$ in this case. The EPF velocity when $d/\lambda << 1$ is a factor of 2/3 less than the Helmholtz-Smoluchowski equation (Eq. A-8). This is attributed to the electrophoretic drag exerted by counterions in the EDL of the charged particle which move in the opposite direction to the particle itself (Li, 2004).

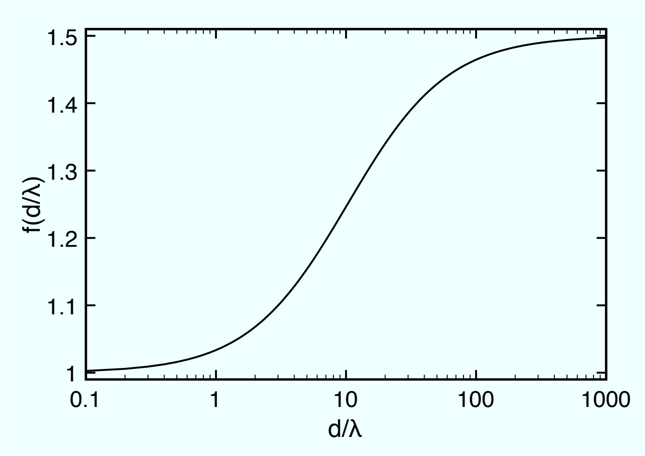

Figure A-3: Plot of Henry's function, $f(d/\lambda)$, as a function of d/λ. $f(d/\lambda)$ tends to 1 when d/λ is small and to 1.5 when d/λ is large.

APPENDIX B

OBTAINING NANOPARTICLE SIZE DISTRIBUTION USING DYNAMIC LIGHT SCATTERING

Dynamic light scattering (DLS), sometimes also known as Photon Correlation Spectroscopy or Quasi-Elastic Light Scattering, is a technique for measuring the size of particles typically in the sub-micron region (Pecora, 1985). DLS essentially measures the translational diffusion coefficient, D, of particles suspended in a liquid medium and relates this measured quantity to the diameter of the particles, d by using the Stokes-Einstein equation shown in Eq. B-1, where k is Boltzmann's constant, T is the temperature, and η is the viscosity of the liquid medium.

$$d = \frac{kT}{3\pi\eta D} \tag{B-1}$$

Fig. B-1 shows a schematic of the optical configuration used by a typical DLS instrument such as the Malvern Zetasizer Nano ZS, which we have used for our experiments in Chapter III, Section 3.4.2. A sample cell, containing the nanoparticles being analyzed in a suitable liquid medium, is illuminated with attenuated laser light (typically of wavelength ~ 600 nm). The incident light is scattered by the nanoparticles present in the sample cell. The scattering intensity is a function of particle diameter, and can be accurately described by Mie theory (van de Hulst, 1957). Consequently, the Brownian motion of the nanoparticles is also affected by the scattering. Small particles will move more rapidly after a scattering event compared

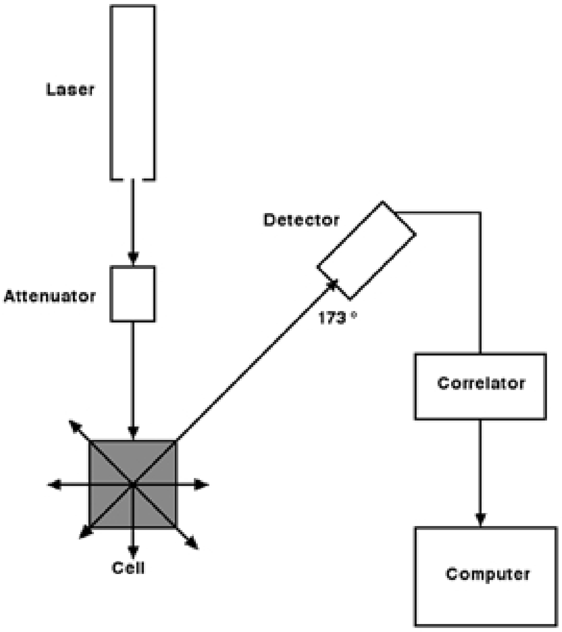

Figure B-1: Schematic of optical configuration in Malvern Zetasizer Nano ZS instrument used for DLS-based nanoparticle size distribution measurements.

to larger particles. The scattered light is then collected by a detector placed at 173° for the case of the Malvern Zetasizer Nano ZS. This detection arrangement is called backscatter detection and has two main advantages over detection at 0° or 90°. First, the laser does not have to travel through the entire sample so the effect of multiple scattering, where light from one particle is scattered by other particles. Second, contaminants such as dust particles within the liquid medium, which are typically large compared to the nanoparticles being analyzed, mainly scatter in the forward direction. So, the effect of dust particles is reduced by using backscatter detection.

Typically, large particles cause large fluctuations in scattering intensity that persist for a longer time, while small particles cause small fluctuations in scattering intensity that decay faster. The scattering intensity signal recorded by the detector is then fed into a digital processing unit called a correlator which compares the scattering intensity at successive time intervals to determine the rate at which the light intensity is varying. The correlator constructs a correlation function, $G(\tau)$, of the scattered intensity which can be written as

$$G(\tau) =< I(t) \cdot I(t + \tau) > \tag{B-2}$$

where τ is the time interval at which the intensity is compared by the correlator. It must be noted here that the correlation function may be defined differently depending upon the algorithm used by the software to derive the size distribution of the particles. Eq. B-2 shows the correlation function used by the Malvern Zetasizer Nano ZS instrument we used for our experiments in Chapter III, Section 3.4.2. The positions of the nanoparticles in the liquid medium will be approximately the same at time t and $t + \tau$, when τ is small (typically up to a few μs). Thus, the correlation between the scattering intensities at time t and $t + \tau$ will be large and the correlation function will be ~ 1. At longer time intervals, the positions of the nanoparticles will change significantly due to Brownian motion and so the correlation between the scattering intensities will decay, and the correlation function will gradually reduce to zero. Fig. B-2a shows a typical correlogram for a sample containing small nanoparticles where the correlation function decays faster while Fig. B-2b shows a typical correlogram for a sample containing larger nanoparticles where the correlation function takes a long time to decay. The time at which the correlation function starts to decay is indicative of the mean diameter of the nanoparticle sample as illustrated in Fig. B-2, and the gradient of the decay is indicative of the polydispersity of the sample.

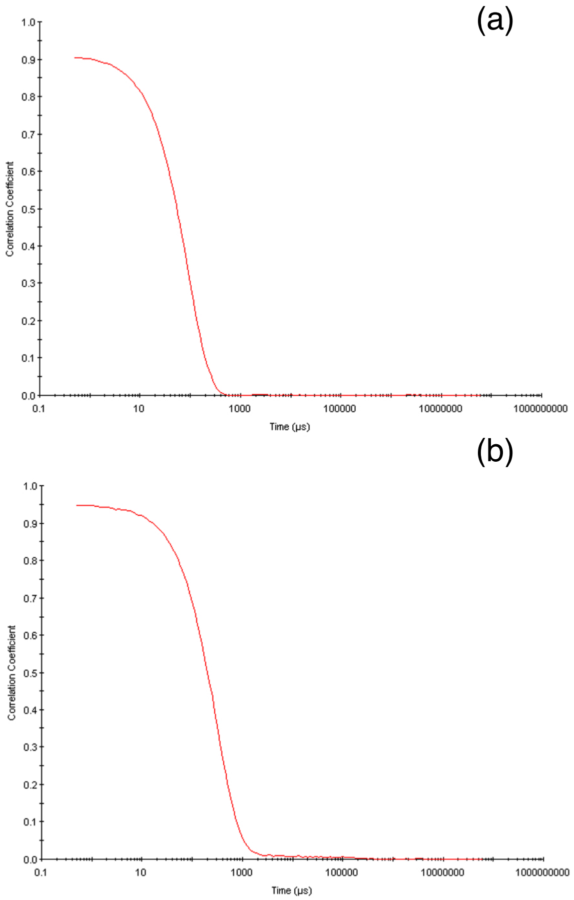

Figure B-2: Typical correlation function decays expected for a sample of (a) small nanoparticles, and (b) large nanoparticles. Smaller particles have higher Brownian velocities so the correlation starts to decay at an earlier time compared to larger particles that have lower Brownian velocities.

This information is then sent to a computer where the software typically fits the correlation function with a multiple exponential function, using methods such as nonnegative least squares (NNLS) or CONTIN (Provencher, 1982; Stock & Ray, 1985) to obtain a distribution of diffusion coefficients and hence a particle size distribution. For a simple, monodisperse sample of nanoparticles, the correlation function, $G(\tau)$, can be fitted by a single exponential function as shown in Eq. B-3,

$$G(\tau) = A\left[1 + B\exp(-2Dq^2\tau)\right] \tag{B-3}$$

where A = baseline of the correlation function, B = intercept of the correlation function, $q = (4\pi n/\lambda_0)\sin(\theta/2)$, n = refractive index of the liquid medium, λ_0 = wavelength of laser, and θ = scattering angle = 173°. The diffusion coefficient(s) obtained are then transformed into particle diameters using the Stokes-Einstein relation shown in Eq. B-1.

REFERENCES

Allen, M. P., Tildesley, D. J., 1987. *Computer Simulations of Liquids.* Oxford University Press, New York.

Auroux, P. A., Iossifidis, D., Reyes, D. R., Manz, A., 2002. Micro Total Analysis Systems. 2. Analytical Standard Operations and Applications. *Anal. Chem.* **74**, 2637–2652.

Bayley, H., Cremer, P. S., 2001. Stochastic sensors inspired by biology. *Nature* **413**, 226–230.

Bayley, H., Martin, C. R., 2000. Resistive-Pulse Sensing - From Microbes to Molecules. *Chem. Rev.* **100**, 2575–2594.

Behrens, S. V., Grier, D. G., 2001. The charge of glass and silica surfaces. *J. Chem. Phys.* **115**, 6716–6721.

Berendsen, H., Grigera, J., Straatsma, T., 1987. The missing term in effective pair potentials. *J. Phys. Chem.* **91**, 6269–6271.

Berendsen, H., Postma, J., van Gunsteren, W., DiNola, A., Haak, J., 1984. Molecular dynamics with coupling to an external bath. *J. Chem. Phys.* **81**, 3684–3690.

Berge, L. I., Feder, J., Jøssang, T., 1989. A novel method to study single-particle dynamics by the resistive pulse technique. *Rev. Sci. Instrum.* **60**, 2756–2763.

Bezrukov, S. M., Vodyanoy, I., Parsegian, V. A., 1994. Counting polymers moving through a single ion channel. *Nature* **370**, 279–281.

Brennen, C. E., 1995. *Cavitation and Bubble Dynamics.* Oxford University Press, New York.

Carbonaro, A., Sohn, L. L., 2005. A resistive-pulse sensor chip for multianalyte immunoassays. *Lab Chip* **5**, 1155–1160.

Carey, V., 1992. *Liquid-Vapor Phase-Change Phenomena - An Introduction to the Thermophysics of Vaporization and Condensation Processes in Heat Transfer Equipment.* Series in Chemical and Mechanical Engineering. Taylor & Francis, Bristol, PA.

Casey, H. C., 1999. *Devices for Integrated Circuits: Silicon and III-V Compound Semiconductors.* Wiley, New York.

Chang, H., Kosari, F., Andreadakis, G., Alam, M. A., Vasmatzis, G., Bashir, R., 2004. DNA-Mediated Fluctuations in Ionic Current through Silicon Oxide Nanopore Channels. *Nano Lett.* **4**, 1551–1556.

Chen, P., Gu, J., Brandin, E., Kim, Y. R., Wang, Q., Branton, D., 2004a. Probing Single DNA Molecule Transport Using Fabricated Nanopores. *Nano Lett.* **4**, 2293–2298.

Chen, P., Mitsui, T., Farmer, D. B., Golovchenko, J. A., Gordon, R. G., Branton, D., 2004b. Atomic Layer Deposition to Fine-Tune the Surface Properties and Diameters of Fabricated Nanopores. *Nano Lett.* **4**, 1333–1337.

Coulter, W. H., 1953. Means for counting particles suspended in a fluid. U.S. Patent No. 2,656,508, issued 20 Oct. 1953.

Coulter, W. H., 1956. High Speed Automatic Blood Cell Counter and Cell Size Analyzer. *Proc. Natl. Electron. Conf.* **12**, 1034–1042.

Daiguji, H., Yang, P., Majumdar, A., 2004. Ion transport in nanofluidic channels. *Nano Lett.* **4**, 137–142.

de Leeuw, S. W., Perram, J. M., Smith, E. R., 1980a. Simulation of electrostatic systems in periodic boundary conditions. I. Lattice sums and dielectric constants. *Proc. Roy. Soc. Lond. A* **373**, 27–56.

de Leeuw, S. W., Perram, J. M., Smith, E. R., 1980b. Simulation of electrostatic systems in periodic boundary conditions. II. Equivalence of boundary conditions. *Proc. Roy. Soc. Lond. A* **373**, 57–66.

DeBlois, R. W., Bean, C. P., 1970. Counting and sizing of submicron particles by the resistive pulse technique. *Rev. Sci. Instrum.* **41**, 909–915.

DeBlois, R. W., Wesley, R. K. A., 1977. Sizes and Concentrations of Several Type C Oncornaviruses and Bacteriophage T2 by the Resistive-Pulse Technique. *J. Virol.* **23**, 227–233.

Erickson, D., Li, D., 2004. Integrated microfluidic devices. *Anal. Chim. Acta* **507**, 11–26.

Ewald, P. P., 1921. Die berechnung optischer und elektrostatischer gitterpotentiale. *Ann. Phys.* **64**, 253–287.

Fan, R., Karnik, R., Yue, M., Li, D., Majumdar, A., Yang, P., 2005. DNA Translocation in Inorganic Nanotubes. *Nano Lett.* **5**, 1633–1637.

Fologea, D., Uplinger, J., Thomas, B., McNabb, D. S., Li, J., 2005. Slowing DNA Translocation in a Solid-State Nanopore. *Nano Lett.* **5**, 1734–1737.

Frenkel, D., Smit, B., 2002. *Understanding Molecular Simulations - From Algorithms to Applications*, 2nd Edition. Academic Press, San Diego.

Heng, J. B., Ho, C., Kim, T., Timp, R., Aksimentiev, A., Grinkova, Y. V., Sligar, S., Schulten, K., Timp, G., 2004. Sizing DNA Using a Nanometer-Diameter Pore. *Biophys. J.* **87**, 2905–2911.

Henriquez, R. R., Ito, T., Sun, L., Crooks, R. M., 2004. The resurgence of Coulter counting for analyzing nanoscale objects. *The Analyst* **129**, 478–482.

Henry, D. C., 1931. The cataphoresis of suspended particles, Part 1. The equation of cataphoresis. *Proc. Roy. Soc. Lond. A* **133**, 106–129.

Hunter, R. J., 1981. *Zeta Potential in Colloid Science.* Academic Press, London.

Ito, T., Sun, L., Crooks, R. M., 2003. Simultaneous Determination of the Size and Surface Charge of Individual Nanoparticles Using a Carbon Nanotube-Based Coulter Counter. *Anal. Chem.* **75**, 2399–2406.

Ito, T., Sun, L., Henriquez, R. R., Crooks, R. M., 2004. A Carbon Nanotube-Based Coulter Nanoparticle Counter. *Acc. Chem. Res.* **37**, 937–945.

Jagtiani, A., Sawant, R., Zhe, J., 2006a. A label-free high throughput resistive-pulse sensor for simultaneous differentiation and measurement of multiple particle-laden analytes. *J. Micromech. Microeng.* **16**, 1530–1539.

Jagtiani, A., Zhe, J., Hu, J., Carletta, J., 2006b. Detection and counting of micro-scale particles and pollen using a multi-aperture Coulter counter. *Meas. Sci. Technol.* **17**, 1706–1714.

Kang, S. M., Leblebici, Y., 1999. *CMOS Digital Integrated Circuits: Analysis and Design*, 2nd Edition. McGraw-Hill, Boston, MA.

Karnik, R., Castelino, K., Majumdar, A., 2006. Field-effect control of protein transport in a nanofluidic transistor circuit. *Appl. Phys. Lett.* **88**, 123114.

Karnik, R., Fan, R., Yue, M., Li, D., Yang, P., Majumdar, A., 2005. Electrostatic control of ions and molecules in nanofluidic transistors. *Nano Lett.* **5**, 943–948.

Kasianowicz, J. J., Brandin, E., Branton, D., Deamer, D. W., 1996. Characterization of individual polynucleotide molecules using a membrane channel. *Proc. Natl Acad. Sci.* **93**, 13770–13773.

Kinjo, T., Gao, G. T., Zeng, X. C., 2000. Bubble nucleation in confined liquids: Molecular dynamics study. *Prog. Theor. Phys. Suppl.* **138**, 732–733.

Kinjo, T., Matsumoto, M., 1998. Cavitation processes and negative pressure. *Fluid Phase Equil.* **144**, 343–350.

Kinjo, T., Ohguchi, K., Yasuoka, K., Matsumoto, M., 1999. Computer simulation of fluid phase change: vapor nucleation and bubble formation dynamics. *Comp. Mat. Sci.* **14**, 138–141.

Knight, J., 2002. Honey, I shrunk the lab. *Nature* **418**, 474–475.

Kobayashi, Y., Martin, C. R., 1997. Toward a molecular Coulter counter type device. *J. Electroanal. Chem.* **431**, 29–33.

Koch, M., Evans, A. G. R., Brunnschweiler, A., 1999. Design and fabrication of a micromachined Coulter counter. *J. Micromech. Microeng.* **9**, 159–161.

Larsen, U. D., Blankenstein, G., Branebjerg, J., 1997. Microchip coulter particle counter. In: *Proc. Transducers '97.* Vol. 2. Chicago, IL, pp. 1319–1322.

Li, D., 2004. *Electrokinetics in Microfluidics.* Vol. 2 of Interface Science and Technology. Elsevier Academic Press, Amsterdam.

Li, J., Gershow, M., Stein, D., Brandin, E., Golovchenko, J. A., 2003. DNA molecules and configurations in a solid-state nanopore microscope. *Nature Mat.* **2**, 611–615.

Li, J., Stein, D., McMullan, C., Branton, D., Aziz, M. J., Golovchenko, J. A., 2001. Ion-beam sculpting at nanometre length scales. *Nature* **412**, 166–169.

Lide, D. R., 2002. *Handbook of Chemistry and Physics.* CRC Press, Cleveland.

Lugli, F., Zerbetto, F., 2007. An introduction to bubble dynamics. *Phys. Chem. Chem. Phys.* **9**, 2447–2456.

Lyklema, J., 1995. *Fundamentals of Colloid and Interface Science.* Vol. II. Academic Press, London.

Maruyama, S., Kimura, T., 2000. A Molecular Dynamics Simulation of Bubble Nucleation on Solid Surface. *Int. J. Heat Technol.* **8**, 69–74.

Masliyah, J. H., Bhattacharjee, S., 2006. Electrokinetic and Colloid Transport Phenomena. Wiley, Hoboken, NJ.

Meller, A., Branton, D., 2002. Single molecule measurements of DNA transport through a nanopore. *Electrophoresis* **23**, 2583–2591.

Miyamoto, S., Kollman, P., 1992. SETTLE: An analytical version of the SHAKE and RATTLE algorithm for rigid water models. *J. Comp. Chem.* **13**, 952–962.

Nagayama, G., Tsuruta, T., Cheng, P., 2006. Molecular dynamics simulation on bubble formation in a nanochannel. *Int. J.Heat Mass Tran.* **49**, 4437–4443.

Nakane, J. J., Akeson, M., Marziali, A., 2003. Nanopore sensors for nucleic acid analysis. *J. Phys.: Condens. Matter* **15**, R1365–R1393.

Novak, B. R., Maginn, E. J., McCready, M. J., 2007. Comparison of heterogeneous and homogeneous bubble nucleation using molecular simulations. *Phys. Rev. B* **75**, 085413.

Park, S., Weng, J. G., Tien, C. L., 2000. Cavitation and Bubble Nucleation using Molecular Dynamics Simulation. *Microscale Thermophys. Eng.* **4**, 161–175.

Pecora, R., 1985. *Dynamic Light Scattering: Applications of Photon Correlation Spectroscopy.* Plenum Press, New York.

Peterman, M. C., Ziebarth, J. M., Braha, O., Bayley, H., Fishman, H. A., Bloom, D. M., 2002. Ion channels and lipid bilayer membranes under high potentials using microfabricated apertures. *Biomed. Microdevices* **4**, 231–236.

Provencher, S. W., 1982. A constrained regularization method for inverting data represented by linear algebraic or integral equations. *Comput. Phys. Commun.* **27**, 213–227.

Qiao, R., Aluru, N. R., 2003. Ion concentrations and velocity profiles in nanochannel electroosmotic flows. *J. Chem. Phys.* **118**, 4692–4701.

Reyes, D. R., Iossifidis, D., Auroux, P. A., Manz, A., 2002. Micro Total Analysis Systems. 1. Introduction, Theory, and Technology. *Anal. Chem.* **74**, 2623–2636.

Rodriguez-Trujillo, R., Mills, C. A., Samitier, J., Gomila, G., 2007. Low cost micro-Coulter counter with hydrodynamic focusing. *Microfluid. Nanofluid.* **3**, 171–176.

Saleh, O. A., Sohn, L. L., 2001. Quantitative sensing of nanoscale colloids using microchip Coulter counter. *Rev. Sci. Instrum.* **72**, 4449–4451.

Saleh, O. A., Sohn, L. L., 2003. An Artificial Nanopore for Molecular Sensing. *Nano Lett.* **3**, 37–38.

Sikdar, S. K., Webster, S. H., 1980. Coulter particle counting at high counting rates. *J. Phys. E: Sci. Instrum.* **13**, 1075–1077.

Siwy, Z., Fulinsky, A., 2002. Origin of 1/f(alpha) noise in membrane channel currents. *Phys. Rev. Lett.* **89**, 158101.

Smeets, R. M. M., Keyser, U. F., Dekker, N. H., Dekker, C., 2008. Noise in solid-state nanopores. *Proc. Natl Acad. Sci.* **105**, 417–421.

Smeets, R. M. M., Keyser, U. F., Krapf, D., Wu, M.-Y., Dekker, N. H., Dekker, C., 2006a. Salt Dependence of Ion Transport and DNA Translocation through Solid-State Nanopores. *Nano Lett.* **6**, 89–95.

Smeets, R. M. M., Keyser, U. F., Wu, M. Y., Dekker, N. H., Dekker, C., 2006b. Nanobubbles in Solid-State Nanopores. *Phys. Rev. Lett.* **97**, 088101.

Sridhar, M., Xu, D., Hmelo, A. B., Feldman, L. C., Li, D., 2008a. Molecular Dynamics Simulations of Thermal Bubble Nucleation in Nanochannels, *Microfluid. Nanofluid.*, (submitted).

Sridhar, M., Xu, D., Kang, Y., Hmelo, A. B., Feldman, L. C., Li, D., Li, D., 2008b. Experimental characterization of a metal-oxide-semiconductor field-effect transistor-based Coulter counter. *J. Appl. Phys.* **103**, 104701.

Stock, R. S., Ray, W. H., 1985. Interpretation of photon correlation spectroscopy data: A comparison of analysis methods. *J. Polym. Phys.: Polym. Phys. Ed.* **23**, 1393–1447.

Storm, A., Storm, C., Chen, J., Zandbergen, H., Joanny, J. F., Dekker, C., 2005. Fast DNA Translocation through a Solid-State Nanopore. *Nano Letters* **5**, 1193–1197.

Sun, L., Crooks, R. M., 2000. Single Carbon Nanotube Membranes: A Well-Defined Model for Studying Mass Transport through Nanoporous Materials. *J. Am. Chem. Soc.* **122**, 12340–12345.

Sze, S. M., 1981. *Physics of Semiconductor Devices.* Wiley, New York.

Tabard-Cossa, V., Trivedi, D., Wiggin, M., Jetha, N. N., Marziali, A., 2007. Noise analysis and reduction in solid-state nanopores. *Nanotechnology* **18**, 305505.

Uram, J. D., Ke, K., Mayer, M., 2008. Noise and Bandwidth of Current Recordings from Submicrometer Pores and Nanopores. *ACS Nano* **2**, 857–872.

van de Hulst, H. C., 1957. *Light Scattering by Small Particles.* Wiley, New York.

van den Berg, A., Lammerink, T. S. J., 1998. Micro Total Analysis Systems: Microfluidic Aspects, Integration Concept and Applications. *Top. Curr. Chem.* **194**, 21–49.

Verlet, L., 1967. Computer "Experiments" on Classical Fluids. I. Thermodynamical Properties of Lennard-Jones Molecules. *Phys. Rev.* **159**, 98–103.

Vlassiouk, I., Siwy, Z., 2007. Nanofluidic Diode. *Nano Lett.* **7**, 552–556.

White, F. M., 2006. *Viscous Fluid Flow*, 3rd Edition. McGraw-Hill, Singapore.

Wu, Y., Pan, C., 2003. A Molecular dynamics simulation of bubble nucleation in homogeneous liquid under heating with constant mean negative pressure. *Microscale Thermophys. Eng.* **7**, 137–151.

Xu, D., 2008. *Development of ultra-sensitive fluidic sensors and molecular dynamics studies of ion and water distribution in nanochannels.* Ph.D. thesis, Vanderbilt University.

Xu, D., Kang, Y., Sridhar, M., Hmelo, A. B., Feldman, L. C., Li, D., Li, D., 2007. Wide-Spectrum, Ultrasensitive Fluidic Sensors with Amplification from both Fluidic Circuits and MOSFETs. *Appl. Phys. Lett.* **91**, 013901.

Yeh, I., Berkowitz, M., 1999. Ewald summation for systems with slab geometry. *J. Chem. Phys.* **111**, 3155–3162.

Zhang, J., Peng, X., Peterson, G., 2000. Analysis of phase-change mechanisms in microchannels using cluster nucleation theory. *Microscale Thermophys. Eng.* **4**, 177–187.

Zhang, Z., Zhe, J., Chandra, S., Hu, J., 2005. An electronic pollen detection using Coulter counting principle. *Atmos. Environ.* **39**, 5446–5453.

Zhe, J., Jagtiani, A., Dutta, P., Hu, J., Carletta, J., 2007. A micromachined high throughput Coulter counter for bioparticle detection and counting. *J. Micromech. Microeng.* **17**, 304–313.